The Thesis Committee for Sean Dewaputra Brame

Certifies that this is the approved version of the following Thesis:

The Effect of Rock Morphology on Steam Foam Rheology

APPROVED BY

SUPERVISING COMMITTEE:

Quoc P. Nguyen, Supervisor

Zoya Heidari

The Effect of Rock Morphology on Steam Foam Rheology

by

Sean Dewaputra Brame

Thesis

Presented to the Faculty of the Graduate School of

The University of Texas at Austin

in Partial Fulfillment

of the Requirements

for the Degree of

Master of Science in Engineering

The University of Texas at Austin

May 2019

Acknowledgements

I am incredibly grateful for this experience of studying and working as a graduate student at UT Austin these past two years. The knowledge and experience I have gained are impossible to describe with words. I would like to thank and express gratitude to Dr. Nguyen for this opportunity and his continuous guidance. I am also extremely grateful for the guidance that Dr. Zoya Heidari provided during the writing of this thesis. I would also like to thank The Dow Chemical Company and their team for sponsoring this project. I greatly appreciate the guidance I received from people I have worked with on this project. Special thanks go to Litan Li and Bi Nguyen for their mentorship. Thanks also go to Vence Sie, Rafael Perez, and Oualid M'barki for their advice and help throughout my work. I also appreciate the companionship from my fellow graduate students here at CPE. Thank you, David Fukuyama, Sercan Gul, Daniel Hatchell, Hanyu Li, Jeff Luo, and Javid Shiriyev for sharing this experience with me. A huge shout out to my friends outside of UT, who have helped to round-out and complete my experience of living, studying, and working in Austin. Thank you, Ali Darwiche, Kane Dinh, Thao Huynh, Anna Hsu, Zeeky Le, Alex Lee, Bagel Nguyen, Lillian Trinh, Sean Vo, and George Yang for all the fun times and for keeping me sane. There are many more I would like to thank, but the list is endless. Finally, thank you to my family for their continued support and motivation.

Abstract

The Effect of Rock Morphology on Steam Foam Rheology

Sean Dewaputra Brame, M.S.E

The University of Texas at Austin, 2019

Supervisor: Quoc P. Nguyen

The injection of steam as an enhanced oil recovery method to produce heavy oil is a mature technology. However, due to its high mobility, steam injection suffers from gravity override, viscous fingering, and loss to thief zones. Steam foam has been used to improve the sweep efficiency of steam injection processes. Steam foaming processes have been used successfully in the 1970s and 1980s, but more work has to be done to better understand and optimize the process for successful field implementation. Recent work has developed better surfactants for high-temperature foams above 200°C, but the physics of steam foam in varying reservoir conditions have been neglected. The purpose of this work was to study the change in the rheological behavior of steam foam in rocks with differing morphological properties, namely permeability and microheterogeneity. Based on the results of sand pack floods, it was concluded that permeability and foam quality govern the trend of apparent viscosity growth and decay for a given sand permeability. It was also determined that at high velocities, the shear thinning effect on steam foam is offset by new foam generation in heterogeneous sands. While the permeability of the sand more significantly influences foam viscosity, it was concluded that the microheterogeneity of a sand pack does affect foam dynamics. Experimentation with rock cores have proved to be more complex, and important limitations have been identified.

Table of Contents

List of Tables

List of Figures

Chapter 1 Introduction

This chapter discusses the motivations and objectives of this work. The chapter begins with a discussion on the background, use, and challenges of steam foam as an enhanced oil recovery method. The motivation for why a better understanding of the relationship between rock morphology and steam foam behavior is provided. Next, the research objectives of the study are given. The chapter closes with a brief outline of the remaining chapters of this work.

1.1 Motivation

As proven conventional reserves are exploited, more attention has turned to unconventional resources. These include shale resources, coal bed methanes, oil sands (bitumen), and heavy oils. Unconventionals require the utilization of more advanced technology to recover the resources. The production of heavy oil, including oil sands/bitumen, is led by Canada and Venezuela. The US, in particular, is highly dependent on these resources, as 40% of US crude imports in 2016 were from heavy oil resources in Canada and Venezuela (U.S. Energy Information Administration, 2016). However, heavy oil reserves are also found in many other countries and hold the potential for widespread exploitation as they make up about 30% of total global oil resources (Schlumberger, 2016). Heavy oil, as opposed to conventional resources, is a highly viscous hydrocarbon resource. It is defined as having a viscosity of greater than 200 cP at reservoir conditions, or below 20° API. Bitumen, typically found in oil sands, generally has the criteria of less than 12° API and greater than 10,000 cP (Dusseault, 2001). Heavy oil is produced through in-situ thermal methods or surface mining in the case of shallow oil sands. In-situ thermal methods require the injection of steam, which is the most commonly used and the most effective thermal enhanced recovery (EOR) process to recover heavy oil (Delamaide et al., 2016). Thermal EOR methods are widely used and account for 53% of EOR processes used for onshore production (Kang et al., 2016). Steam injection techniques include steam drives or floods, cyclic steam stimulation (CSS), steam-assisted gravity drainage, and in-situ combustion (ISC). As heavy oils are, by definition, highly viscous and practically

immobile, heat is used to reduce its viscosity. Steam is typically used due to its price, availability, and high heat of condensation. The injected steam propagates in the formation, and at the edge of the steam from, it condenses, liberating its heat and causing a reduction in oil viscosity. This allows the oil to flow towards producing wells.

Steam injection is a mature technology with strong success in field applications, where recoveries in steam flood processes can exceed 50% of OOIP. However, there are a number of drawbacks to steam injection processes that arise due to the inherent low viscosity and high mobility of the steam. Steam injection can suffer greatly from reservoir heterogeneity, and cause gravity override, channeling, viscous fingering, and loss to thief zones. Steam flows through high permeability channels within a formation, which leads to poor vertical sweep and early breakthrough in steam drives. In cyclic and SAGD processes, steam chambers are only partially developed due to variances in reservoir permeability (Chen et al., 2010). This leaves bypassed oil in low permeability intervals or zones.

Foam has been utilized to mitigate the loss of steam to channeling and to improve the efficiency of the process. The use of foam in steam injection processes, by injected steam foam, was first proposed in 1968 to plug high permeability strata to divert steam into lower permeability strata in order to improve the injection profile (Hirasaki, 1989). The creation of foam increases the apparent viscosity of the steam, which results in a decrease in mobility. Lowering the mobility of steam mitigates its loss to thief zones and channeling, resulting in a better distribution of steam to lower permeability intervals.

Since first being proposed as a solution to steam loss issues, steam foam has been utilized in pilots from the 1970s through to the early 1990s. By the mid-1990s, the research and development of the steam foam process had slowed, but interest has reemerged in the last decade as heavy oil reservoirs continue to become an attractive source for petroleum resources. Recent advances in steam foam have focused on new, high-temperature surfactant formulations, novel foaming agents, and the optimization of the steam foam process.

These advances have added significantly to the understanding of steam foam, but research in the last few years have neglected the effect of the rock environment. Some work has developed a better understanding of foam generation at the pore-scale. However, these were done in relatively homogeneous systems. Real reservoirs are much more complex at the pore-level, with a variance in grain and pore sizes in a given rock. Thus, there is a lack of in-depth understanding of the effect of rock morphology on foam behavior. A better understanding of the rheology of steam foam in environments with high micro- and macro-heterogeneity is key to optimizing the process when coupled with advances in surfactant formulation.

1.2 Research Objectives

The purpose of this work was to study the effect of rock morphology on steam foam rheological behavior. Rock morphology includes properties and parameters such as permeability, microheterogeneity, and pore structure. This was achieved by conducting several core flood experiments using both sand packs and consolidated rock cores to study the effect of permeability and heterogeneity. To evaluate the steam foam's rheological behavior, the apparent viscosities of the foam were calculated from the pressure drop within a specific rock environment while varying foam quality and interstitial velocity (flow rate). The objectives are summarized as:

1. Study the effect of varying permeability and grain size distribution in sand pack systems on steam foam strength. Foam strength was assessed through its rheological behavior.
2. Up-scale the study of foam rheological behavior in porous media to more complex, heterogeneous systems in consolidated rocks.
3. Develop an understanding of steam foam generation, propagation, and destruction in different rock morphology environments through the core flood experiments.
4. Study the effects of geochemical reactions between injected solutions and rock environments at high temperature, including mineral dissolution, fines migration, and grain swelling.

5. Develop techniques to analyze the pore-scale system of porous media through CT imaging, MICP, and NMR tests in order to build an understanding of the relationship between pore-scale environments and steam foam rheological behavior.

1.3 Description of Chapters

Chapter 2 provides a review of the literature related to foam and steam foam as an EOR process. This discussion includes a review of the purpose of steam foam, fundamentals of foam physics, foaming surfactants, as well as recent advances in developing the technology.

Having established the necessary background knowledge in Chapter 2, Chapter 3 covers the first phase of the study on the effect of rock morphology on steam foam behavior and rheology. The chapter discusses the motivations and purposes of this phase of the study, in which sand packs were used, as well as outlines the objectives. The chapter includes a detailed description of the methodology used for pore-scale characterization and dynamic testing of foam in porous media. Finally, the chapter discusses in detail the results of the experiments and the interpretations of the data.

Chapter 4 covers the second phase of the study, in which consolidated rock cores were used. Chapter 4 discusses the experiments conducted using low permeability rocks. This chapter provides a discussion of the purpose and research objectives of this phase. A detailed description of all the experimental methods is given, and how they differ from those processes described in Chapter 3. Finally, results are presented, and the data are discussed. Due to the difficulties with low permeability rock cores, this phase of the study was discontinued, and work with high permeability rocks is proposed.

Chapter 5 covers advanced rock characterization techniques used to accurately determine rock properties, such as pore size distribution. The rock characterization tests described in this chapter were designed and conducted to supplement studying foam rheology in a more complex, high permeability, rock environment. The chapter includes a

discussion on the motivations and objectives of this study. A detailed description of all methodologies is provided. Finally, a discussion of the results of the experiments and the interpretation of the data is given.

Finally, Chapter 6 discusses in detail the conclusions reached in this study from the interpretation of the data. The chapter presents the conclusions reached and the knowledge developed about the relationship between rock morphology and steam foam rheology. A discussion on the efficacy and limitations of the experimental methods devised is also included. The chapter closes with a discussion on recommendations moving forward to advance the work and widen the scope of the study.

Chapter 2 Literature Review

This chapter provides a review of the literature related to foam and steam foam as an EOR process. This discussion includes a review of the purpose of steam foam, fundamentals of foam physics, foaming surfactants, as well as recent advances in developing the technology.

2.1 Purpose and History of Steam Foam

The injection of gas to improve the recovery of oil is one of the most widely used processes for enhanced oil recovery (EOR). In 2016, gas EOR accounted for 38.4% of all EOR methods onshore, and 68.4% of offshore EOR methods (Kang et al., 2016). Furthermore, the use of steam injection, a thermal EOR method, accounts for almost 50% of EOR methods in that year. Steam injection is the most efficient EOR method to recover heavy oil and bitumen. The injected steam condenses when it contacts the cooler oil, and liberates its heat and causes a reduction in oil viscosity. This allows the oil to flow towards producing wells. The injection of gaseous fluids is, therefore, a process of extreme importance (Gul et al., 2017). Despite its widespread use, however, gas and steam injection suffer from its high mobility.

The high mobility of the displacing gas as compared to the displaced fluid (oil and water) is unfavorable. Mobility ratio is the ratio of the mobility of the displacing fluid (gas) to that of the displaced fluid. An aimed, favorable mobility ratio is around 1 or less. This results in stable, piston-like displacement and flow. Due to the large contrast between gas and liquid viscosities, the mobility ratio of gas to oil and water ranges between 10 and 100 (Hematpur et al., 2018). Due to its mobility and lower density, gas and steam injection suffer greatly from gravity override and viscous fingering. This issue is compounded by reservoir heterogeneity, which results in gas loss to thief zones and channeling through high permeability streaks, bypassing oil in lower permeability strata. These issues lead to poor vertical sweep, early breakthrough of gas, and inefficiency in the injection scheme (Boeije and Rossen, 2015). The left-hand illustrations in **Fig. 2.1** displays the poor sweep

issues. In the figure, steam is shown in red, while oil is shown in green. Poor sweep is a result of gravity override, where gas segregates from the oil and flows along the top of the reservoir due to its low density, and viscous fingering.

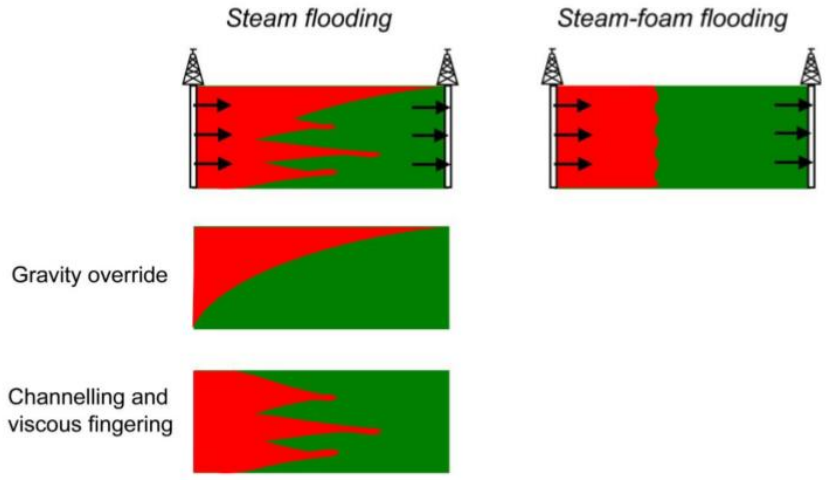

Figure 2.1 – Steam Foam Improves Steam Injection (Bagheri, 2015)

Foam has been widely used to mitigate the issues of poor sweep and to improve the efficiency of gas injection. Through the injection of surfactant with gas, foam is formed to reduce gas mobility and relative permeability. The use of foam was first proposed in 1958 (Bond and Holbrook, 1958). The creation of foam increases the apparent viscosity of the gas, lowering its mobility, and therefore, lowers the mobility ratio between the displacing and displaced fluids. Foam plugs up high permeability strata, and thus diverts flow to lower permeability intervals (Hirasaki, 1989). This results in better sweep and displacement of oil and water, thus promoting piston-like flow, shown in the right-hand illustration of **Fig. 2.1**. Lowering its mobility also mitigates gas loss to high permeability streaks or thief zones. The use of foam is a well-researched and tried approach to EOR. The prospect of using foam in high-temperature steam injection, however, is a newer concept.

The use of foam in steam injection processes was first proposed for mobility control in 1968 (Needham, 1968). Steam foam was first tested in a field application in 1973, with many subsequent tests and pilots following. Over 30 field pilots have been performed and

documented, particularly in California, during the 1970s and 1980s (Cooke and Eson, 1991). However, due to low oil prices, steam foam has not been performed since the mid-1990s. The lack of field utilization has also led to a lull in research work. Steam foam was an area of heavy interest in research and laboratory studies, particularly in developing foaming surfactant agents that can tolerate the high temperatures necessary during steam injection (Delamaide et al., 2016). Much of the work in the past has also focused on the physics and modeling of steam foam injection and transport.

Research interest in steam foam has resurged in recent years, however. In the last decade, much focus has returned to developing the steam foam process and new, high-temperature surfactants due to the wide-spread use of SAGD (Chen et al., 2010). As conventional resources are depleted and attention turns to unconventionals such as heavy oils and bitumen, the optimization of thermal EOR methods are becoming increasingly more important to produce hydrocarbons efficiently. Steam foam has, once again, emerged as a hot topic for research and development to efficiently tap into heavy oil resources.

2.2 Foam Fundamentals

Foam, in a simple sense, is defined as gas bubbles dispersed in a liquid. It is a colloid, a homogeneous, non-crystalline substance of microscopic particles dispersed through a second phase. Other examples of colloids are gels and emulsions. Foam is, therefore, a colloidal system of a disperse or internal phase (gas) that is dispersed in a continuous, external phase (liquid). Foam is formed when gas bubbles are injected faster than liquid films can drain away (Schramm, 1994). **Fig. 2.2** shows a simple illustration of a homogeneous foam system. The figure shows gas bubbles dispersed in a liquid. The bubbles are formed by pockets of gas surrounded by thin liquid films. These liquid films make up part of a region called a lamella. Lamellae include the liquid film, two gas-liquid interfaces on either side of the film, as well as the junction to other lamellae, called the plateau border. As described, a lamella is stable when gas bubbles are injected in faster than the liquid drains from the films. And thus, foam is formed. In a stable foam, bubbles transform to foam "cells." These cells are polyhedral with flat liquid films, such as the ones

shown in **Fig. 2.2**. Due to surface tensions, three lamellae come together to form 120° angles, and the meeting point is the plateau border.

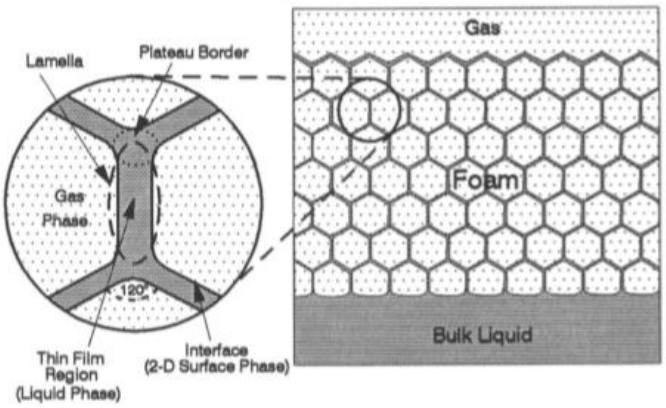

Figure 2.2 – A Generalized Foam System (Schramm, 1994)

Foams are unstable systems. Gas bubbles eventually coalesce, or come together, leading to foams being destroyed. This happens due to liquid draining from lamellae, causing rupture. The use of surfactants as a foaming agent in the liquid phase strengthens the lamellae to aid foam stability. Surfactants collect at the gas-liquid interface, mitigating lamellae rupture, and creates what is called persistent or stable foam (Schramm, 1994). Of course, stable in this sense means relatively stable, as foam films will rupture eventually. Stability refers mainly to the time scale at which foam collapses.

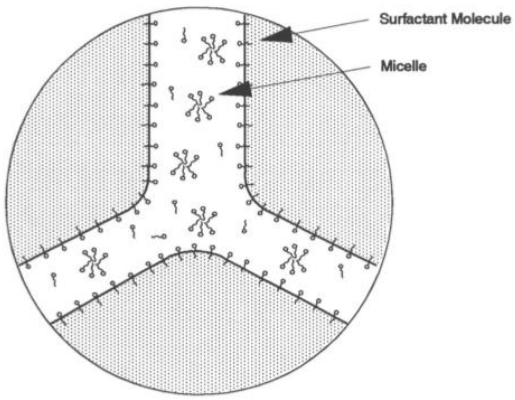

Figure 2.3 – Surfactant Associations in Foam Lamellae (Schramm, 1994)

Surfactants reduce the surface or interfacial tension, increase the interfacial area, and create protective films to prevent bubble coalescence. **Fig. 2.3** shows an illustration of surfactant molecules collecting at the interface between gas and liquid. These molecules are called monomers. Surfactant monomers have a nonpolar and polar side and form a monolayer on the gas-liquid interface. Monomers are adsorbed to the layer and lower surface tension and increase the resistance to film thinning. High concentrations and solubility of surfactant lead to the formation of micelles, which are groups of monomers. It is important for stable foam to have micelle formation, as that leads to an abundance of monomers for film stabilization. Research has shown that increasing the surfactant concentration aids in foam stability due to the creation of micelles. This is true up to a critical micelle concentration (CMC), above which increasing the surfactant concentration does not affect stability.

The rheology of foam films is also important for stability. High interfacial viscosity can increase stability by lowering the drainage rate and inhibiting coalescence (Schramm, 1994). The addition of surfactant can increase the surface viscosity. Due to the strong relationship between viscosity and temperature, foam stability strongly depends on temperature. This, of course, is a challenge in the case of high-temperature steam foam applications. The texture of the foam is also an important consideration. Smaller bubbles are more stable than larger ones. A wide distribution of bubble sizes is detrimental as there will be a pressure gradient between differently sized bubbles. This promotes gas diffusion, resulting in larger bubbles and foam degradation.

Foam can be formed in bulk by flowing gas into a bulk liquid solution. However, in the application of the oil and gas industry, foam must be formed to displace oil in porous media. Thus, the generation, destruction, and transport of foam have been greatly studied. Rather than in a bulk foam, where foams are a collection of gas bubbles separated by liquid films, foams in porous media are better described as trains of liquid films traveling through pore channels. This is shown in **Fig. 2.4**. The figure shows discontinuous gas that is separated by liquid lamellae. In reservoir applications, the gas is described as the

nonwetting phase and the liquid as the wetting phase. As time passes, the gas and lamella travel through the pore throat. Studies have found that bubbles are larger than the pore dimensions in reservoir rock, so that bubbles span a pore space, as shown in **Fig. 2.4**. This type of foam is called a confined foam, as compared to bulk foams mentioned previously and shown in **Fig. 2.2**. Foam films can rupture as it is traveling, due to the contraction and expansion of the film as it passes through constricted spaces.

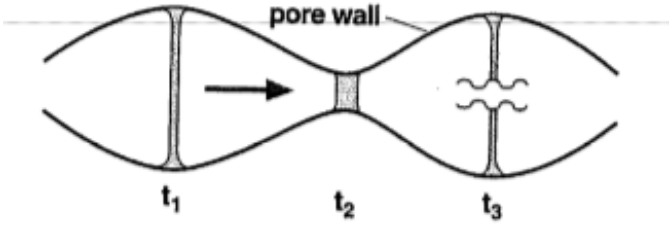

Figure 2.4 – Foam Transported in a Periodically Constricted Tube (Schramm, 1994)

There are three mechanisms of foam formation in porous media (Schramm, 1994). These are snap-off, division, and leave behind. **Fig. 2.5** shows the first of these mechanisms. Snap-off is where gas bubbles snap off a bulk gas phase when it travels through a pore throat. This occurs due to capillary pressure fluctuations across constricted pore throats (Hematpur et al., 2018). Snap-off is the most common and the main mechanism for foam formation in porous media.

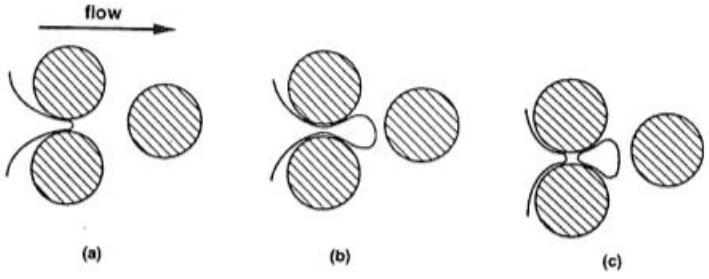

Figure 2.5 – Schematic of Snap-Off Mechanism (Schramm, 1994)

Fig. 2.6 shows a schematic of the division mechanism. In division, existing bubbles or lamellae are further subdivided when a branch or junction in the pore channel is encountered. Finally, leave behind occurs when a section of the pore body is not "invaded" by gas bubbles so that a liquid lens between grains is left behind. Due to the way it is formed, leave behind lamellae are generally parallel to flow direction. Thus, they do not create a discontinuity in the flowing gas in a pore channel and do not lead to a train of flowing gas and lamellae as illustrated in **Fig. 2.4**.

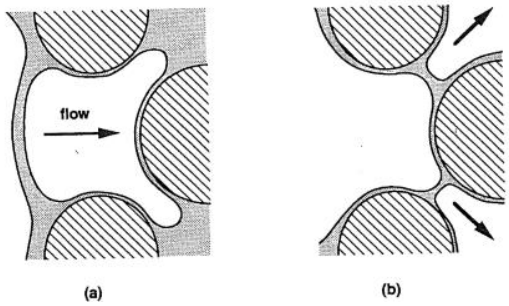

Figure 2.6 – Schematic of Division Mechanism (Schramm, 1994)

Net foam formation cannot continue unchecked, so foam generation is also coupled with foam destruction. Foam destruction occurs when bubbles coalesce via capillary suction and gas diffusion (Schramm, 1994). Capillary suction is the main mechanism that causes foam lamella rupture. The flow of foam through a pore channel causes rupture due to the continuous expansion and shrinkage of the lamellae, as described previously in **Fig. 2.4**. Foam stability is limited by a limiting capillary pressure, P_c* (Khatib et al., 1988). Foam becomes weak and easily collapses once the limiting capillary pressure is reached. This is especially true when the wetting phase saturation is low, as capillary pressure is high. Therefore, as liquid drains from the liquid films between gas bubbles, capillary pressure increases until it passes P_c*, where the chance of rupture greatly increases.

The purpose of using steam foam as an EOR method is to improve the recovery of heavy oil. Therefore, understanding the interaction between foam and oil is fundamental to designing and optimum injection and recovery process. Surfactants are often used in

EOR to improve oil recovery. Surfactants are able to lower the interfacial tension between oil and water and therefore, increase oil-water relative permeabilities (Amaefule and Handy, 1982). By decreasing the interfacial tension, the formation of emulsions is promoted. Emulsions are dispersions of a liquid within another liquid (Alvarado and Marsden, 1979). For example, oil-in-water emulsions is a fluid with oil dispersed in the aqueous phase. By having oil dispersed in water, the flow of oil is promoted due to the lack of competition between the oil and water phases to flow through a pore space. The surfactant in the foam wetting phase is able to solubilize, emulsify, and mobilize oil. Oil is then carried in the plateau borders during foam flow. This is shown in the photo in **Fig. 2.7**.

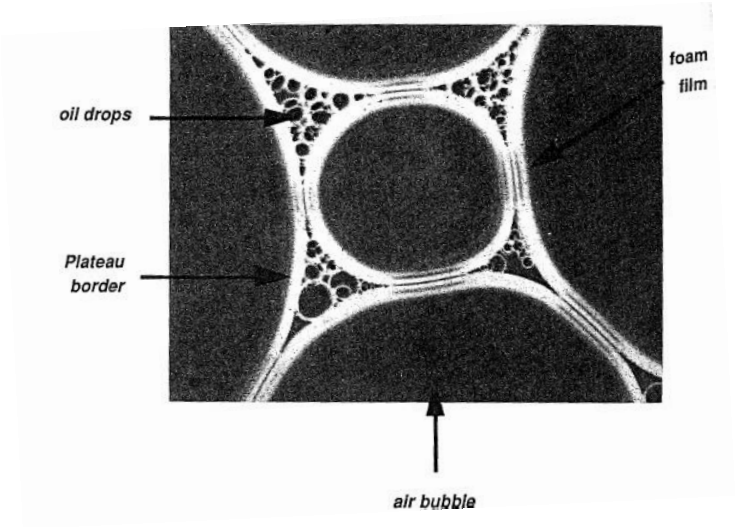

Figure 2.7 – Oil Droplets in Foam Lamellae (Schramm, 1994)

However, oil has a destabilizing effect on foam. Oil accelerates the rate of foam thinning, increasing the chance of film rupture. **Fig. 2.8** shows an illustration of lamellae containing oil. Oil droplets within the plateau borders are separated by emulsions films, and the oil droplets are separated from the gas-liquid interface by a pseudo-emulsion film. Foam stability in the presence of oil is strongly controlled by the stability of the pseudo-emulsion film. The stability of the pseudo-emulsion film depends on surfactant concentration, electrolyte concentration, film size, and capillary pressure (Schramm,

1994). Therefore, its stability is fragile. If the pseudo-emulsion film is not stable, oil acts as an anti-foaming agent. Oil destabilizes foam in a number of ways. Oil absorbs surfactant, oil components are adsorbed by porous media (changing wettability and affecting foam generation), oil spreads on lamellae (causing rupture), and oil emulsification allows droplets to breach the stabilizing interface. In the presence of oil, it is also difficult to form and propagate foam. Due to these reasons, it is important to inject foam when oil is at residual saturation. Some foams have been shown not to propagate when oil saturation is 10-15% (Schramm, 1994). Light oil has a stronger destabilizing effect on foam than heavy oils. Due to heavy oil's high viscosity, it emulsifies slower, which then slows the rate of lamellae breakage. The more viscous the oil, the more foam stability is present. This is an important result for the applicability of foam to a steam injection process.

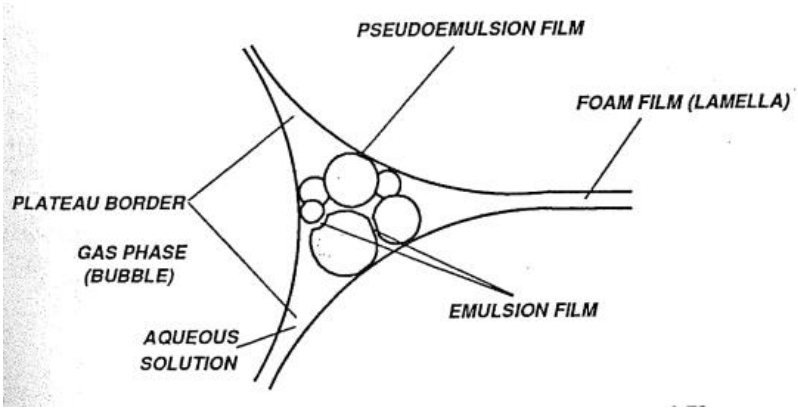

Figure 2.8 – An Illustration of Foam Lamellae Containing Oil Droplets (Schramm, 1994)

How foams are formed, destroyed, and transported at the micro- or pore-level have been described. However, as discussed, foams are used to decrease the mobility of gas on the reservoir level. For field applications, the properties and rheology of bulk foam are of importance. Foam reduces gas mobility by increasing the apparent viscosity of the bulk system. Foams are frequently pseudoplastic in nature. It is shear thinning: as the shear rate increases, the viscosity decreases. Some foams have a yield stress when it is a persistent foam and shows more plastic behavior than pseudoplastic. However, these rheological

properties are difficult to measure as foams are a two-phase system and can't be measured with classic rheological methods.

On the pore-scale, confined foam and discontinuous gas flow drastically reduce gas permeability. Research has found that the wetting phase permeability is relatively unaffected by foam flow. The apparent viscosity of the confined foam scales with bubble density, so foam texture greatly affects gas mobility. Finer texture foams, which contain larger bubbles and greater lamella density, increase flow resistance.

The properties and efficacy of a formed foam are generally tested through the use of static bulk foam experiments and dynamic core floods (Delamaide et al., 2016). These experiments can test a foaming agent's performance in terms of thermal stability, solubility, adsorption, foaming efficiency, and the effect of oil. Bulk foam properties, as mentioned, are made in static systems. Foam in dynamic systems, however, are continuously generated in porous media. Therefore, it is difficult to correlate the results of the two experiments. Bulk foam tests are often done to compare different formulations for their foamability.

Bulk foam stability experiments test the ability of a surfactant to stabilize lamellae. More specifically, they evaluate the effectiveness and efficiency of a surfactant solution. Effectiveness refers to the amount of foam generated, while efficiency refers to the amount of foam generated per unit mass of surfactant. In a bulk foam test, foam is generated in a vessel and allowed to decay. Common parameters measured are the column height of the foam, which gives the amount of foam created, and its half-life, the decomposition of foam as a function of time. This parameter gives a comparative method for the stability of a generated foam. Through these tests, investigators can test the impact of pressure, temperature, oil, and gas nature.

Dynamic core flood experiments can give information on the surfactant and foam's efficacy when injected into porous media. These can be conducted with or without oil. Foam generation is evaluated by measuring the pressure drop across the core or porous

medium. The pressure drop data can then be used to calculate the apparent viscosity of the foam or the mobility reduction factor (MRF). The mobility reduction factor is the capacity for the foam to decrease gas mobility and therefore reduce the mobility ratio between the gas and liquid phases.

Core floods are the most representative experiments that can be conducted for reservoir conditions. Foaming capacity in core floods is influenced by pressure, temperature, surfactant formulation, surfactant concentration, injection strategy, oil saturation, and a few more properties. Through these dynamic experiments, three additional important properties of foam injection can be evaluated to help optimize the design of a field process. The steam quality, foam quality, and interstitial velocity of the foam at the point of injection are important to carefully select and design for optimum foam generation and stability. Steam quality refers to the weight percent of water in the vapor phase (steam) against water in both the liquid and vapor phases. It is a ratio of the mass of vapor to the total mass of the fluid. Due to the difficulty of generating steam for laboratory purposes, N_2 is generally used instead. N_2 is a non-condensable gas, which has stabilizing properties on foam.

The foam quality, x_F, is the ratio of gas volume in the foam to the total gas and liquid volume, called the gas volume fraction. **Fig. 2.9** shows an illustration of the development of apparent viscosity with foam quality at a fixed interstitial velocity, based on trends reported in literature (Osterloh and Jante, 1992; Alvarez et al., 2001). As more gas is introduced into the foam, the apparent viscosity increases until an optimum value is reached, where a maximum viscosity is achieved. This is a generalized trend seen at both low and high temperatures. As seen in the figure, there is an optimum foam quality, x_F*, the quality at which foam reaches its maximum apparent viscosity. Literature has shown the optimum quality has generally fallen between 70-95% (Delamaide et al., 2016). Below x_F*, foam flows in a low-quality regime. In this regime, discontinuous foam flows and are stable. Above x_F*, there is a high-quality regime which is made up of mostly continuous

gas paths. Flow is dominated by coalescence. Foam quality in core floods is controlled by fluid injection rates, temperature, and pressure.

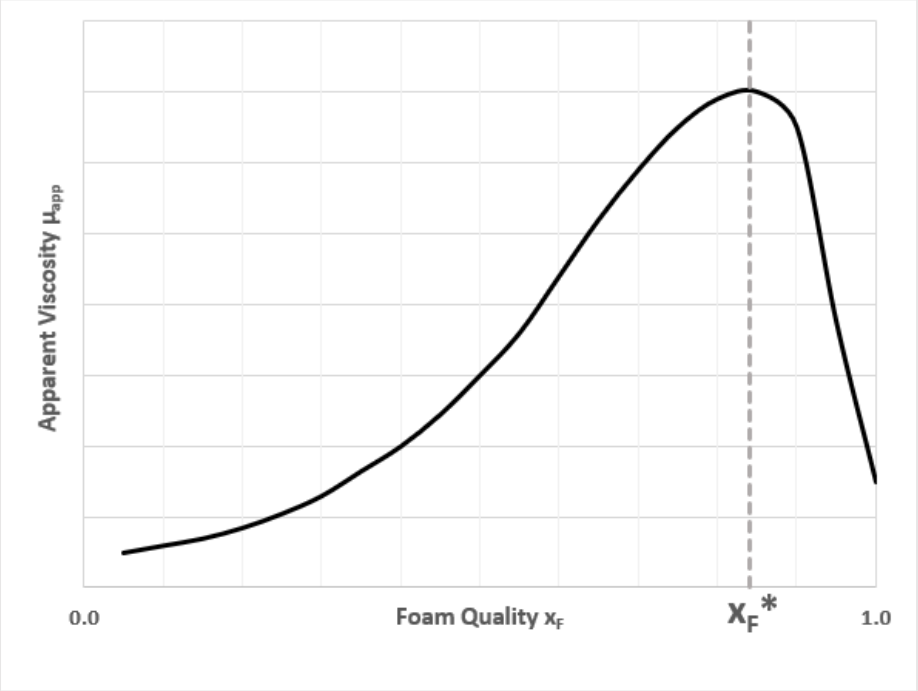

Figure 2.9 – Apparent Viscosity of Foam as a Function of Foam Quality at Fixed Interstitial Velocity

The interstitial velocity generally refers to the velocity of the foam within the porous media. **Fig. 2.10** shows an illustration of the generation and destruction of foam with increasing interstitial velocities at a fixed foam quality. Strong foams show a shear thickening behavior, until a critical velocity, v_i*, is reached, where it starts to show a shear thinning behavior at higher velocities, following power law behavior (Hirasaki and Lawson, 1985). The apparent viscosity and MRF are both functions of the foam quality and interstitial velocity. Both these parameters must be tested over a range of values in core floods in order to select optimum values to best design a foam field application. A strong foam with an intermediate velocity, flowing in a low-quality regime less than x_F* should be targeted.

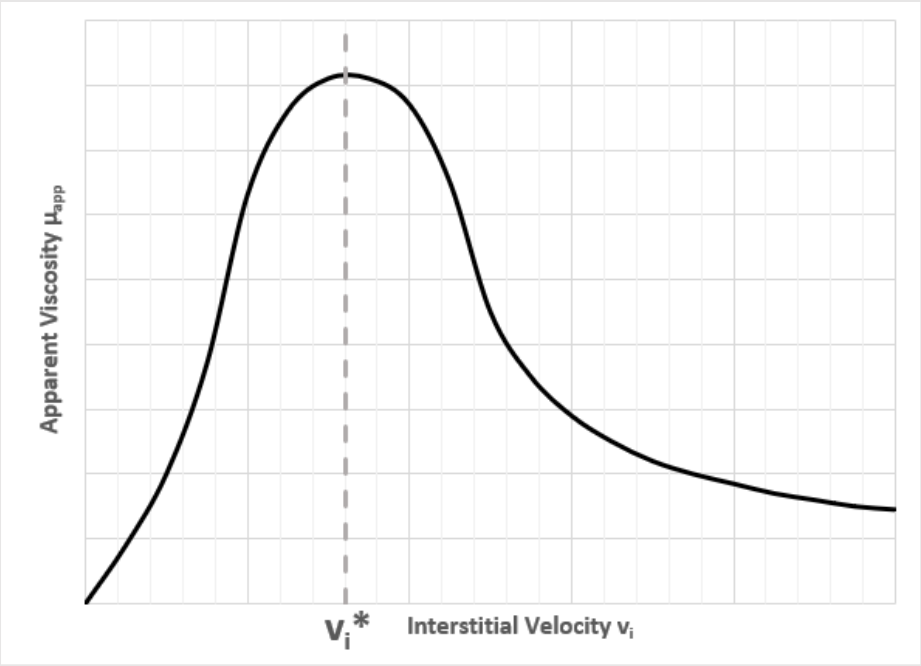

Figure 2.10 – Apparent Viscosity of Foam as a Function of Interstitial Velocity at Fixed Foam Quality

A number of studies have been conducted in literature between the relationship of porous media permeability and the apparent foam viscosity with foam quality. Researchers have investigated how the optimum foam quality and the quality-viscosity curve shifts with varying permeability. In CO_2 foams, it was found that optimum quality decreases with increasing permeability (Moradi-Araghi et al., 1997). However, it was found that the opposite holds true for methane foams, where optimum quality decreases with decreasing permeability (Zeng et al., 2018). The plot in **Fig. 2.11** shows this relationship for methane foam. Optimum foam quality here is labeled as $f_g^{transition}$. It is apparent that the relationship between optimum foam quality and permeability is dependent on the type of foam used and the fluid in the dispersed phase, whether it is methane, CO_2, or other gases. Thus far, no study on the relationship between optimum foam quality and permeability exist for steam foam at high temperature.

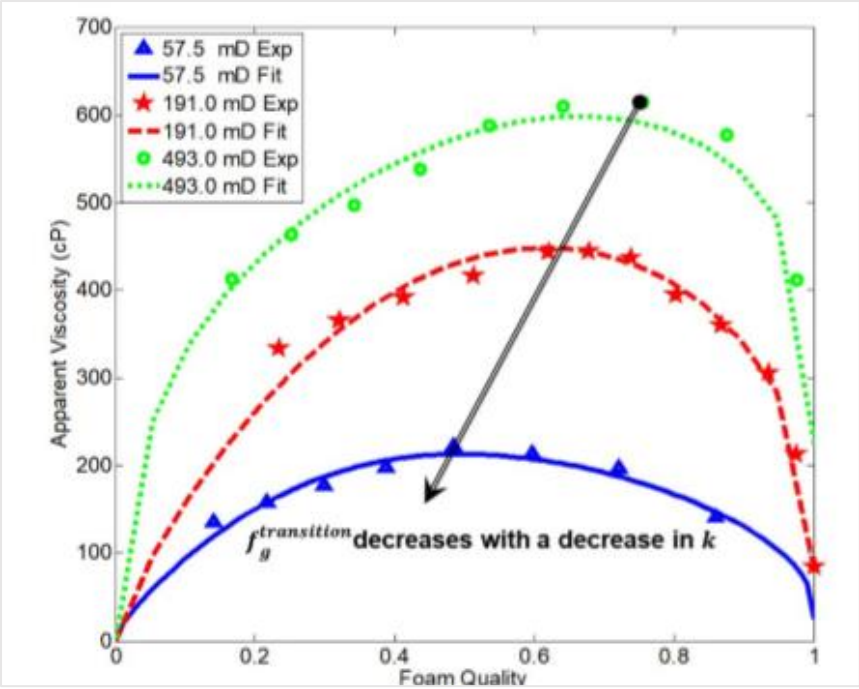

Figure 2.11 – Methane Foam Optimum Quality Decreases with Decreasing Permeability (Zeng et al., 2018)

The fundamentals discussed thus far relate mainly to foams in general. Steam foam is the same as other injected foams, other than what makes up the non-wetting phase. Instead of a gas, steam is injected directly along with a surfactant solution to generate foam in a reservoir. Some non-condensable gas such as N_2 is added to stabilize the foam. Another distinction is that rather than divert gas to promote piston-like flow, the use of steam foam diverts the heat into unheated intervals to lower the viscosity of the oil. Careful consideration has to be given to the durability and stability of both the surfactant and the generated foam at elevated temperatures. Foams are generally more stable at lower temperatures. So, the stability of steam at temperatures above 200°C is highly dependent on good surfactant formulations and foam injection design.

2.3 Foaming Surfactants

Surfactants are used as foaming agents for steam foam. Due to the high-temperature requirements of the surfactant to survive steam injection, only a few families of chemicals have been used in steam applications. Generally, stability at high temperature is one of the most important requirements of surfactants for this process, and much research has been conducted to develop foaming agents that are stable at higher and higher temperatures. Recent advances have pushed surfactant stability toleration past 250°C, with more work conducted to develop surfactants that would be stable for long periods at 300°C (Delamaide et al., 2016). The criteria to be met for a steam foam surfactant are high-temperature stability, foaming ability, solubility, and limited adsorption on reservoir rock. Due to these constraints, sulfonates have been the most widely used and developed.

Two main sub-families have been used in research and industry for the steam foam process. These are alkyl sulfonates and alkyl aryl sulfonates. Alkyl sulfonates include secondary alkane sulfonates (SAS), alfa-olefin sulfonates (AOS), and internal olefin sulfonates (IOS). AOS and IOS based agents have been widely used in recent research, and AOS agents have been shown to have superior foaming performance (Schallcross et al., 1990). Alkyl aryl sulfonates include alkyl toluene sulfonates (ATS), alkyl benzene sulfonates (ABS), and alkyl xylene sulfonates (AXS). The development of foaming agents has included investigating the degree of branching, variations in structural groups, and combining surfactants to improve solubility and decrease adsorption (Delamaide et al., 2016).

Careful selection of the foaming agent used is crucial for a successful and efficient steam foam process. Unfortunately, there is no single, unique formulation that can be used in any steam injection process, at the chemical must be tailored to the specific requirements of the EOR strategy and reservoir. Considerations include application temperature, the type of oil, desired foaming performance (in regards to quality, for example), surfactant concentration, production facility requirements, and the injection strategy (whether it is steam drive, cyclic, or SAGD). For example, long term thermal stability is important for a

steam drive process, while the impact of production facilities is a more important factor for cyclic injection. For each given field application, a formulation must be selected and tailored.

2.4 Recent Advances

Since first being proposed as a solution to steam loss issues, steam foam has been utilized in pilots from the 1970s through to the early 1990s. By the mid-1990s, the research and development of the steam foam process had slowed, but interest has reemerged in the last decade as heavy oil reservoirs continue to become an attractive source for petroleum resources. Much of the research on steam foam in recent years has focused on the development of high-temperature steam foaming agents, as well as improving the temperature range at which steam foam can operate. Due to the requirement of the surfactant to have high-temperature stability, mainly sulfonates and phosphonates have been used to generate steam foam (Delamaide et al., 2016). Recent work has tested the concept of using an alkali/surfactant mixture to improve steam foam propagation (Lau, 2012). Further knowledge has been added to the optimization of the foaming process. Work by Cuenca et al. made strides to explore the correlation between bulk viscosity and foam mobility reduction, as well as better understand the destabilizing impact of oil on steam foam at high temperatures (Cuenca et al. 2015; Cuenca et al. 2016). Etminan et al. studied the optimal conditions for steam foam generation and mobility control (Etminan et al., 2016). Recent work has developed better surfactant formulations at temperatures up to 250°C, which has extended the temperature range at which stable steam foam can be generated in the presence of oil (Sanders et al., 2017). Surfactants can also be optimized with respect to its hydrophobicity to tailor the foam's thermodynamic properties to target specific reservoir temperature and salinity conditions (Nguyen et al., 2018).

Research has also been conducted to explore the applicability and use of steam for SAGD processes (Chen et al., 2010). In fact, the possibilities of using steam foam in the widely-used SAGD process in Alberta, Canada is what has spurred on much of the new

research in the last decade. Chen et al. proposed a process called foam-assisted SAGD, or FA-SAGD, to improve uniform steam chamber formation and improved steam-oil ratios.

Modeling has also been an area of interest in the last few years. Much of the modeling work done in the past focused on simulating successful field pilots. Recently, however, strides have been taken to improve modeling techniques. Many approaches have focused on local equilibrium concepts (Rossen, 2013). Newer approaches have included the simulation of emulsification (Lashgari et al., 2014). Modeling has also been used to study the use of foam for FA-SAGD (Chen et al., 2010).

It is clear that recent advances in steam foam have focused on new, high-temperature surfactant formulations, novel foaming agents, modeling, and the optimization of the steam foam process. These advances have added significantly to the understanding of steam foam, but research in the last few years have neglected the effect of the rock environment. A better understanding of the physics and rheology of steam foam in highly heterogeneous and complex rock environments is key to optimizing the process when coupled with advances in surfactant formulation.

Chapter 3 Unconsolidated Sand Pack

This chapter covers the first phase of the study on the effect of rock morphology on steam foam behavior and rheology. The chapter discusses the motivations and purposes of this phase of the study, in which sand packs were used, as well as outlines the objectives. The chapter includes a detailed description of the methodology used for pore-scale characterization and dynamic testing of foam in porous media. Finally, the chapter discusses in detail the results of the experiments and the interpretations of the data.

3.1 Purpose and Objectives

As discussed, the purpose of this work was to study the effect of rock microheterogeneity on steam foam rheological behavior. The first step to approach this work was to conduct core flood experiments using sand packs, henceforth referred to as sand pack flood experiments. The objective was to use specific mixtures of sands to create specifically designed porous environments in order to study steam foam rheological behavior in controlled systems. Four sand mixtures were designed and made that would vary both permeability and heterogeneity. In this way, the effect of permeability and the effect of microheterogeneity could be independently investigated. Four sand pack flood experiments were conducted, two with low permeability sands, and two with high permeability sands. The two permeability ranges were selected to differ by a magnitude. Each sand pack pair of a specific permeability consisted of a homogeneous and heterogeneous sand pack. This was done by making sand mixtures with a narrow grain size distribution (GSD) and a wide GSD, respectively. **Fig. 3.1** shows an illustrated example of a pore size distribution (PSD), which shows similar trends to that of a GSD. A narrow PSD, denoted by the distribution shaded in red, leads to a homogeneous system. If the pores are all roughly the same size, then grains surrounding those pores are also the same size relative to each grain. Therefore, a sand pack with a narrow GSD leads to a well-sorted, homogeneous system. A wide PSD and GSD, on the other hand, creates heterogeneity within the sand pack, which is poorly-sorted. This is denoted by the distribution shaded in

yellow in the figure. By varying the GSD, and thus the PSD, the sand pack mimics microheterogeneity within a rock.

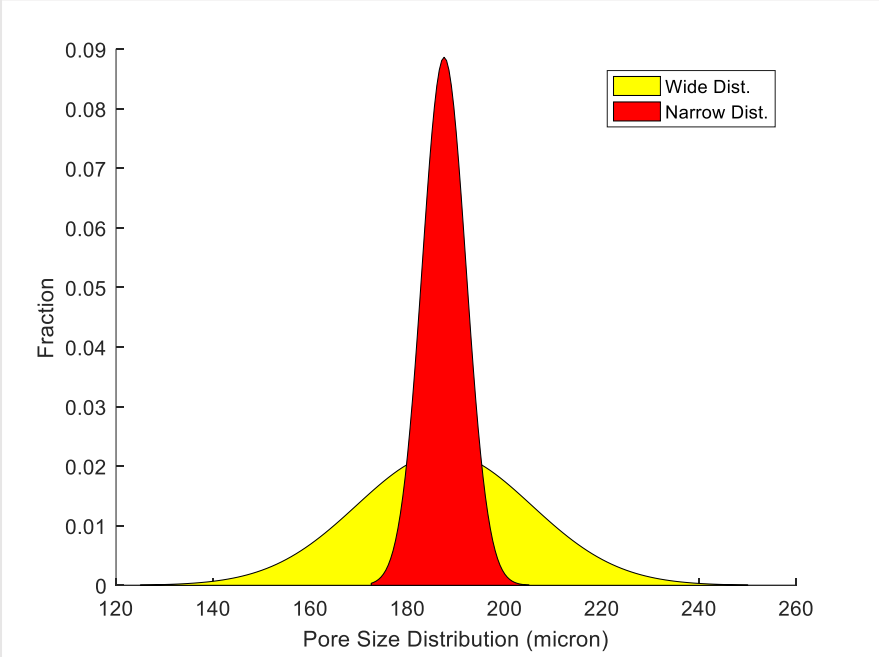

Figure 3.1 – Illustration of Pore Size Distribution

To evaluate the steam foam's rheological behavior, a range of apparent viscosities within a specific sand environment was measured by varying foam quality and interstitial velocity. For each sand pack flood, three velocities and four foam qualities were selected. **Fig. 3.2** shows a simple flow chart of how each sand pack flood was conducted. For each of the two permeabilities, low and high, there was a homogeneous and heterogeneous and pack, reflected in narrow or wide distributions of grain size. For a given sand, the lowest interstitial velocity of foam was performed first. Within that velocity, the quality was varied. Once the whole set of qualities were tested, the velocity was increased to the second value, and all qualities were tested with that velocity. This was repeated for the third and final velocity. The objective was to obtain a full range of apparent viscosity data in order to develop an understanding of steam foam's behavior and how to optimize its design under varying conditions.

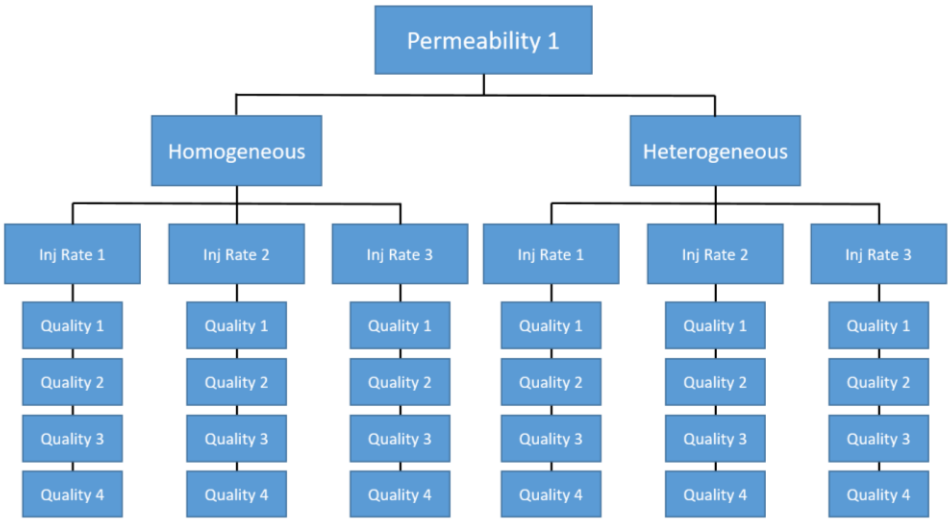

Figure 3.2 – Sand Pack Flood Flow Chart

3.2 Materials and Methods

3.2.1 Sand Preparation and Imaging

The sands used to create the different combinations of bed material for the sand pack floods were selected by utilizing the Krumbein and Monk equation (Krumbein and Monk, 1942):

$$k = 760 d_g^2 e^{-1.31\sigma_D} \quad (1)$$

where k is the permeability, d_g is the geometric mean of the grain diameters, and σ_D is the standard deviation of grain diameters, d, in *phi* units, where $phi = -log_2(d)$. The Krumbein and Monk equation is typically used to predict permeability from the grain size distribution of a rock. In this study, a grain size distribution was designed from a chosen permeability. With a target permeability in mind, a median grain size and standard deviation were obtained using the equation. From these data, a grain size distribution was determined, and grain sizes and quantities were selected. For the low permeability sand mixtures, grains between 120 and 200 mesh (75-125 microns in diameter) were used. The permeability targeted for these mixtures ranged between 4 to 6 Darcy. For the high permeability sands,

grains between 6 and 120 mesh (125-250 microns in diameter) were used. The permeability range for these mixtures was greater than the low permeability sands, targeted between 25 to 30 Darcy. **Table 3.1** gives a detailed breakdown of the sizes and percentages used in each sand pack. All sands used were silica Ottawa sands. **Fig. 3.3** shows a plot of the designed grain size distributions based on the results of using the Krumbein and Monk equation. Through the sand selection and sieving detailed in **Table 3.1**, it was hoped that a similar distribution shown in the figure is be obtained.

Table 3.1 – Sand Pack Mixtures

Low Permeability Homogeneous	**Low Permeability Heterogeneous**	**High Permeability Homogeneous**	**High Permeability Heterogeneous**
170-200 mesh (100%)	170-200 mesh (11%) 140-170 mesh (67%) 120-140 mesh (22%)	70-80 mesh (100%)	80-120 mesh (34%) 70-80 mesh (56%) 60-70 mesh (10%)

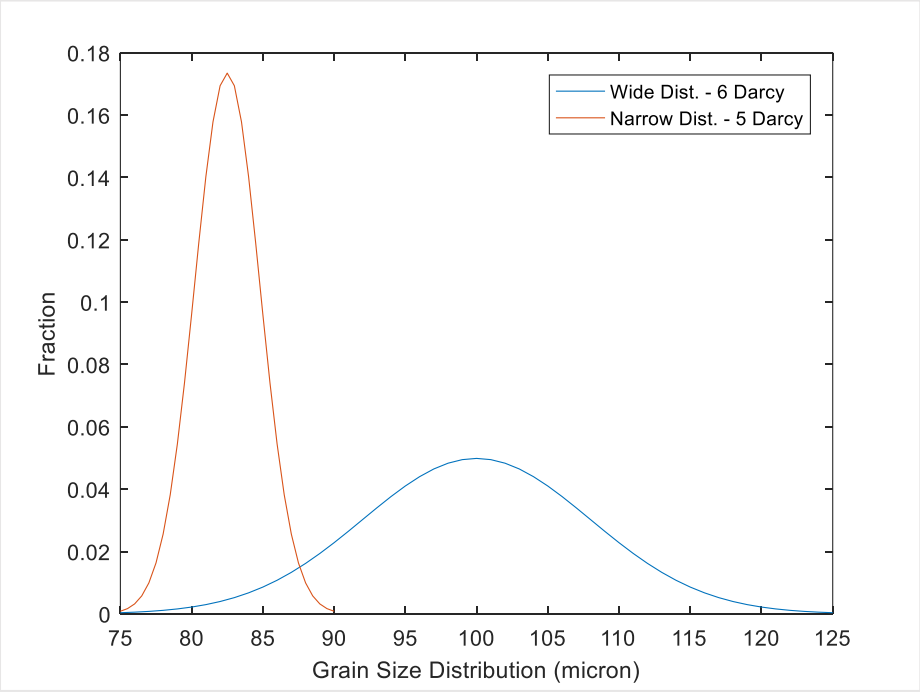

Figure 3.3 – Designed Grain Size Distribution for Low Permeability Sands

CT imaging was utilized to capture the actual distributions of grain sizes for each of the four sand mixtures. This involved taking sand images using a CT scan and using segmentation techniques to separate the pore space from the sand grains in the images. The grains were then analyzed for diameter, and the frequency of diameter sizes was plotted to obtain the distribution. The shape and range of the distribution ensure that a narrow or wide GSD was acquired within the sand mixtures. The images also allowed the qualitative visualization of the range of grain and pore sizes. To analyze the CT scanned images, Fiji ImageJ, an image processing and analysis program, was utilized.

The following is a procedure using UT PGE's CT scanning apparatus and Fiji ImageJ. First, a 1-cm diameter aluminum vessel containing a sample of sand was run through the X-ray CT scan to obtain thin, 2D image slices of the sample. Fiji ImageJ was then used to process the scanned images to obtain the GSD. The image contrast was enhanced to differentiate between grain and void space, and segmentation was applied to divide the data into two phases: solid and void. A watershed algorithm was applied to create boundaries between grains in order to identify each grain.

To determine the GSD of each of the sand samples, the area covered by the individual grains was measured in pixels for all images. There were approximately 1,500 images for each of the sands. Using a MATLAB script and assuming spherical grains, each individual radius was calculated by converting from pixels to microns. A final distribution was obtained by plotting a histogram of all the results for all images within one sand.

3.2.2 Sand Pack Floods

In order to study steam foam rheological behavior in porous media at high-temperature conditions, sand pack flood experiments were designed and conducted. Dow Chemical Company supplied two surfactants for the purpose of the study and to test their efficacy in a core flood. The two surfactants were UT-A and UT-B, both provided in a solution with 30% activity. Both are effective foaming agents, as seen in **Fig. 3.4**. The figure shows a solution of 1.0 wt. % brine with 0.5 wt. % of active UT-A surfactant. The

bottle of solution was shaken to generate foam, and allowed to decay over 4 hours. As seen from the figure, the foam column was quite stable. Despite bubble coalescence, the height of the foam column had only halved by 4 hours.

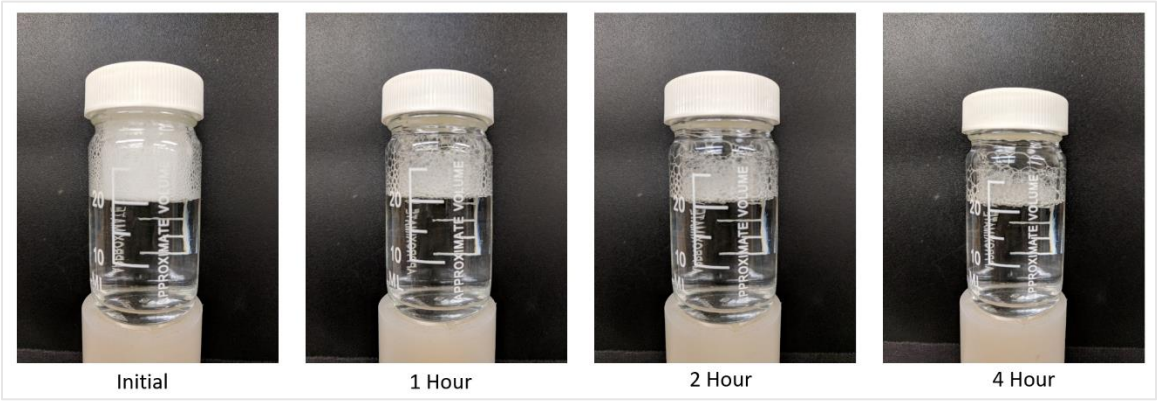

Figure 3.4 – UT-A Foam Decay over Time

The sand pack flood experiments consisted of different sand packs that mimicked different reservoir rock qualities. These were high and low permeability sands, with a narrow and wide grain size distribution. Sand pack floods were conducted at 250°C as recent work has shown that steam foam can generate and propagate at that temperature. Foam performance was determined by the measured pressure drop across the sand pack. The pressure drop is an indication of foam strength and propagation and was used to later calculate the apparent steam foam viscosity, μ_{app}. The sand pack flood experiments were conducted in the absence of oil, as the effect of rock heterogeneity was targeted, without the interference of the destabilizing effects that oil has on foam. Each sand pack flood was conducted at a number of foam qualities and interstitial velocities. The fluids were injected into the sand packs at 40, 80, and 120 ft/day. At each flow rate, the foam qualities were varied at 30%, 50%, 75%, and 90%. The velocities and qualities were controlled by varying the injection rates of the aqueous phase (containing brine and surfactant), and the gas phase (N_2). This was done using the following relations to calculate the gas rates:

$$v_{superficial}\ \left(\frac{cc}{\min}\right) = \frac{30.48 * v_{interstitial}\left(\frac{ft}{day}\right) * A\ (cm^2) * \varphi}{1440} \qquad (2)$$

$$v_{gas-core} = v_{superficial} x_F \quad (3)$$

$$v_{gas-pump} = \frac{P_c v_{gas-core} Z_p T_p}{P_p Z_c T_c} \quad (4)$$

where $v_{gas\text{-}core}$ is the gas velocity in the core (sand pack), $v_{gas\text{-}pump}$ is the pump velocity of the gas, x_F is foam quality, P_c is core pressure, T_c is core temperature, Z_c is the compressibility factor of gas in the core, P_p is pump pressure, T_p is pump temperature, and Z_p is the compressibility factor of gas in the pump. The following relation was then used to calculate the liquid rate for each pairing of velocities and foam qualities:

$$v_{liq-pump} = v_{liq-core} = v_{superficial} - v_{gas-core} \quad (5)$$

Fig. 3.5 shows a schematic of the sand pack flood set-up. Within the set-up, the test surfactant was co-injected at 0.5 wt. % in a 1 wt. % NaCl brine with nitrogen as a non-condensable gas. The co-injection of a non-condensable gas improves the effectiveness of a steam foam process. Non-condensable gas extends the lifetime of foam by limiting mass transfer between steam bubbles within the foam (Falls et al., 1988). Due to this, most sand pack flood experiments to study steam foam rely on nitrogen injection. Other gases such as CH_4 and natural gases are also known to be used in field applications. The 1-in diameter, 12-in length sand pack core holder was placed in a convection oven heated to 250°C. Absolute pressure transducers were connected to the inlet, outlet, and two side taps on the core holder. This allowed for the measurement of the pressure drop at different segments of the sand pack. The transducers used were Omega Engineering USB transducers that connected directly to the computer instead of a DAQ system. An associated program was used to record pressure data. The back-pressure was set at 800 psig to ensure the surfactant-brine solution remained in the liquid state. The injection system included two pumps that separately fed into two piston accumulators. The pumps displaced the surfactant solution out of one accumulator, and N_2 out of the other. The injection rates for each pump were chosen and set using the equations discussed previously. The flow of N_2 was controlled by a back-pressure regulator, and both fluids met downstream of the injection line to be co-injected in the sand pack through a 100-ft coil. The coil was placed in the oven to ensure

that the injected fluid would preheat to the target temperature before entering the sand pack. Two thermocouples were placed on the set-up, with one at the inlet and another at the outlet. Temperature data were recorded to ensure that the injected fluid was reaching the experimental temperature before entering the sand pack.

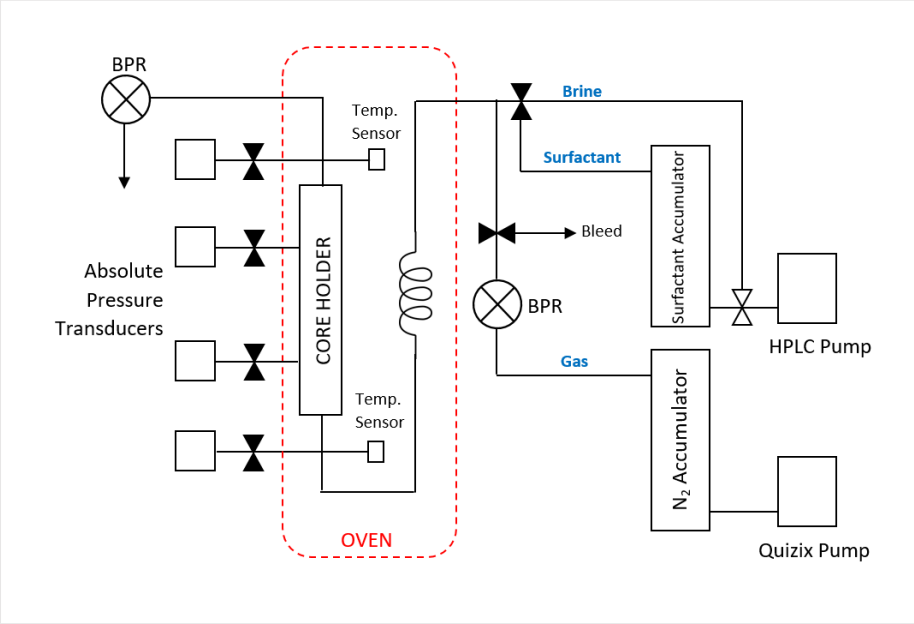

Figure 3.5 – Sand Pack Flood Set-Up Schematic

The following presents a procedure for the sand pack floods. The prepared mixtures of silica Ottawa sand were packed into a core holder. The core holder was secured to a vibrating table, and two 325 mesh screens and a Teflon plug was placed in the bottom assembly. Mesh screens were also placed into the side taps. The mesh screens were used to prevent any sand migration out of the sand pack during fluid injection. The vibrating table was set to a certain frequency and sand was added in 10 cc increments every minute. The shaking of the core holder by the vibration table promoted tight sand packing to minimize the amount of void space. Once the core holder was filled, mesh screens and a Teflon plug were placed at the top before securing the top cap. Once the caps were secured, the sand pack was pressurized with nitrogen and checked for leaks and weighed.

The sand pack was mounted into the convection oven, and the porosity φ and permeability k were measured at ambient temperatures. To measure the porosity, the sand

pack was placed under vacuum to remove trapped air. A 1 wt. % NaCl brine solution was then injected from the inlet at the bottom of the sand pack at 1 cc/min until the pressure inside the pack reached experimental conditions. The slow rate of injection minimized channeling or fingering. Once experimental pressure was reached and maintained by the back-pressure regulator, brine injection was continued at 40 cc/min for about three pore volumes of injected fluid to get rid of all air trapped by capillary trapping. The core holder was then removed from the set-up and weighed. The difference of mass between the saturated and dry sand pack conditions were used to calculate, accounting for dead volume, the pore volume. Once placed back into the oven, the absolute brine permeability was measured. Brine was injected at 10, 20, 30, 40, 30, 20, then 10 cc/min while the pressure data were recorded. The stable pressure drop value at each flow rate was used to calculate the permeability *k* by using Darcy's Law. An average permeability was taken across the flow rates.

The system was then heated to 250°C over a few hours. The temperature data from the thermocouples were monitored to ensure that the experimental temperature was reached. Before foam injection, a baseline flood was conducted with just brine and gas, with no surfactant in the solution. This would not produce foam, and the pressure drop data from this flood were used to calculate the mobility reduction factor (MRF). At the start of foam injection, the sand pack was flushed with 4 to 5 pore volumes of a slug of surfactant solution to meet adsorption requirements using a bottom-to-top injection regime. Once a few pore volumes (PV) of slug were injected at a low rate of 10 PV/day, N_2 was co-injected with the surfactant solution to generate foam. The rates of both fluids were controlled to obtain a specific foam quality at the inlet of the sand pack. At a specific rate and foam quality, steady-state was reached before changing the rates to obtain a new quality and injection rate. This was done for all three rates and four foam qualities. Foam injection started with the lowest rate of 40 ft/day, and all foam qualities were tested with this interstitial velocity before moving onto 80 ft/day, and then 120 ft/day. Foam qualities were increased from 30% up to 90%, then back down again to 30% before switching rates. The pressure data were recorded throughout the flood.

Once the pressure drop data were collected, the apparent viscosity was calculated using Darcy's law:

$$\mu_{app} = \Delta P_{foam} \frac{k}{v_{darcy} L} \tag{6}$$

where ΔP_{foam} is the pressure drop across the sand pack, k is the permeability, L is the length of the sand pack, and v_{Darcy} is the Darcy velocity. The Darcy velocity is simply the interstitial velocity multiplied by the porosity of the sand pack. The mobility reduction factor was calculated using:

$$MRF = \frac{\left(\frac{\Delta P_{foam}}{Q_{foam}}\right)}{\left(\frac{\Delta P_{water-gas}}{Q_{water-gas}}\right)} = \frac{\Delta P_{foam}}{\Delta P_{water-gas}} \tag{7}$$

where ΔP_{foam} and Q_{foam} is the pressure drop and flow rate of the flowing foam, and $\Delta P_{water-gas}$ and $Q_{water-gas}$ is the pressure drop and flow rate of the baseline flood. As the flow rates with and without foam were kept the same, the MRF is a ratio of the pressure drops with and without foam. As the pressure drop increases with foam formation, the reduction factor is expected to be greater than 1.

The pressure drop, apparent viscosity, and MRF data were used to assess the optimum steam foam conditions for each sand pack system, as well as to make comparisons between them to determine the effect of rock heterogeneity on steam foam rheology and behavior.

3.3 Results and Discussions

3.3.1 Sand Imaging

The porosity and permeability of each sand mixture were determined through the flood experiments. The low permeability sand packs obtained permeabilities of 5.71 Darcy and 5.06 Darcy for the homogeneous and heterogeneous sands, respectively. These were within the target range of 4 to 6 Darcy. The high permeability sand packs obtained

permeabilities of 18.00 Darcy and 16.53 Darcy for the homogeneous and heterogeneous sands, respectively. These were well below the target of 25 to 30 Darcy; however, the sands were deemed acceptable as the permeability difference between the two was small, and they were much higher than the low permeability sands. All of the sands had comparable porosities, ranging from 31.7 to 37.7%.

Using a segmentation method, each of the images was processed in order to analyze the grain size distribution. An example for each of the sand mixtures is shown in **Fig. 3.6** below. The left four images show the raw CT images obtained from the scan, while the right set of images show the same slices processed in ImageJ. In the raw images, black denotes void space, while grains are shown in the grayscale. In the processed images, it is the opposite, where black represents sand grains and white represents pore space. The differences in sand sorting can be observed in the processed images. In the narrow GSD sands, which were well-sorted, relatively similar-sized grains can be seen for both high and low permeability sands, leading to large pore spaces and throats. The opposite is observed in the wide GSD, poorly-sorted sands, where smaller grains can be seen in the spaces between larger grains. This leads to tighter and constricted pore spaces. Overall, from the sample images in **Fig. 3.6**, it can be observed that the procedure used in ImageJ was successful at separating and identifying the grains vs. the pores.

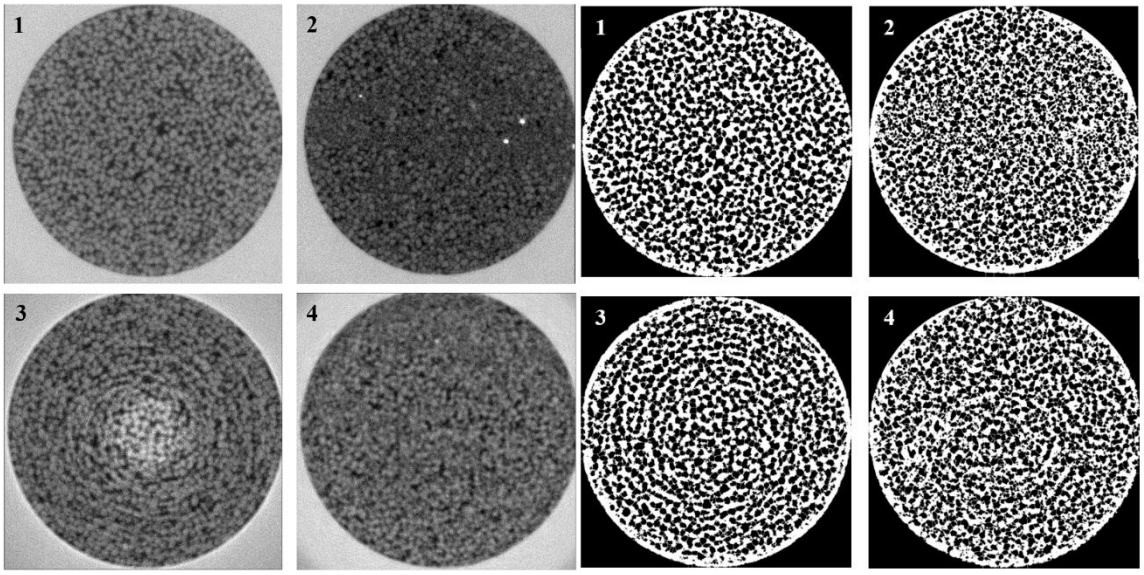

Figure 3.6 – Raw and Processed CT Scanned Sand Images
(1 – Low Permeability, Narrow GSD; 2 – Low Permeability, Wide GSD;
3 – High Permeability, Narrow GSD; 4 – High Permeability, Wide GSD)

The grain measurements for thousands of images were made and imported into the MATLAB script in order to plot the grain size distribution. The analysis of the grain sizes was successful in plotting the distributions of the sand grain diameters. The GSD plots for the two low permeability sands are shown in **Fig. 3.7** as an example.

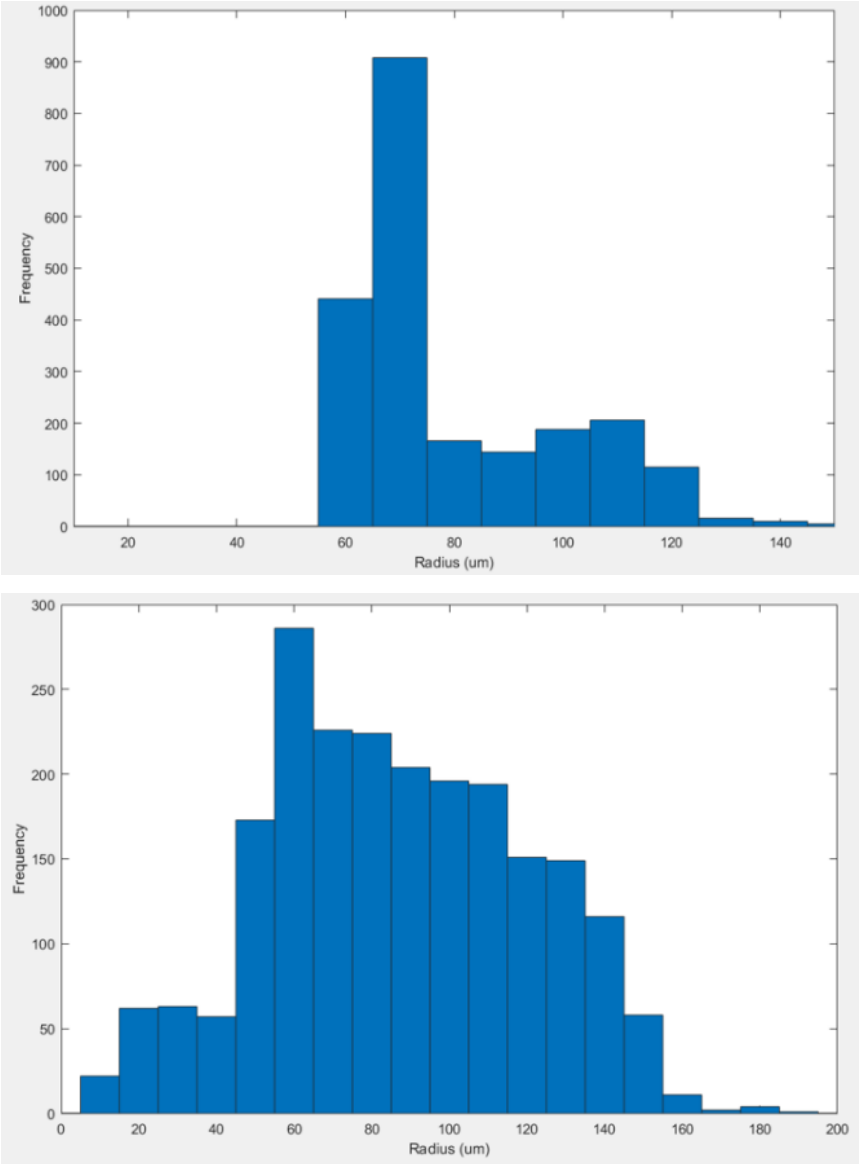

Figure 3.7 – Grain Size Distributions of Low Permeability Sands; Narrow GSD and Wide GSD (note the x-axis is mislabeled as radius when it is diameter)

If both of the distributions in **Fig. 3.7** is compared to the predicted distribution in **Fig. 3.3**, it can be seen that the actual GSD is considerably wider for both sands than the predicted. This is likely due to the failure of the sieving to perfectly separate out small and large grains. Despite this, roughly the same median grain size value is reached for both sands.

Comparing the two GSD plots in **Fig. 3.7**, the distribution for the homogeneous, well-sorted sand is much narrower than that of the heterogeneous, poorly-sorted sand. The homogeneous sand had a grain size range between 60 and 150 μm. The heterogeneous sand, on the other hand, had a much wider range between 10 and 190 μm. Through this method of analyzing the grain size distribution through CT scanned images, the target range of grain sizes in each sand mixture was verified, and the variance in pore sizes was visualized. Furthermore, the knowledge of grain size and pore size aids in the interpretation of sand pack flood results.

3.3.2 Sand Pack Floods

The four sand pack floods were successfully conducted, with the raw pressure drop data shown in **Fig. 3.8-3.11**. **Table 3.2** below shows the parameters for each sand pack flood, including the porosity and permeability. As discussed through the sand imaging results, the porosities were similar in value and permeability met acceptable targets. The systems for each core flood were well designed and controlled.

Table 3.2 – Sand Pack Flood Parameters

	Flood 1 ***Low k Homogeneous***	**Flood 2** ***Low k Heterogeneous***	**Flood 3** ***High k Homogeneous***	**Flood 4** ***High k Heterogeneous***
Porosity	33.7%	31.7%	37.7%	35.0%
Absolute Brine Permeability (D)	5.71	5.06	18.00	16.53
Grain Size Distribution	Narrow	Wide	Narrow	Wide

As can be seen in the plots, the pressure drops are shown for each of the three flow rates (40, 80, 120 ft/day). Within each flow rate, the foam qualities were increased from 30% to 90%, then decreased back down to 30%. This ramping down of the foam qualities was to see any effect of hysteresis. From the plots, it can be seen that the pressure drops

were stable at the same qualities, so hysteresis does not play a role in the sand packs. In these plots, higher pressure drops signify stronger foams and the ability of the foam to reduce steam mobility. The highest pressure drops occur at 50-75% foam quality, depending on the properties of the sand pack. Across all sands, however, the lowest pressure drops occurred at 90% foam quality. At this condition, the foam is said to be "dry," and the lack of aqueous surfactant solution results in less formation of foam or easy rupture of lamellae. The changes in pressure drop within a fixed foam quality are magnified at higher flow rates. This observation is more pronounced in environments with greater degrees of heterogeneity. Despite differences in magnitude, the general trends of pressure drop changes due to altering the foam quality and interstitial velocity were relatively constant.

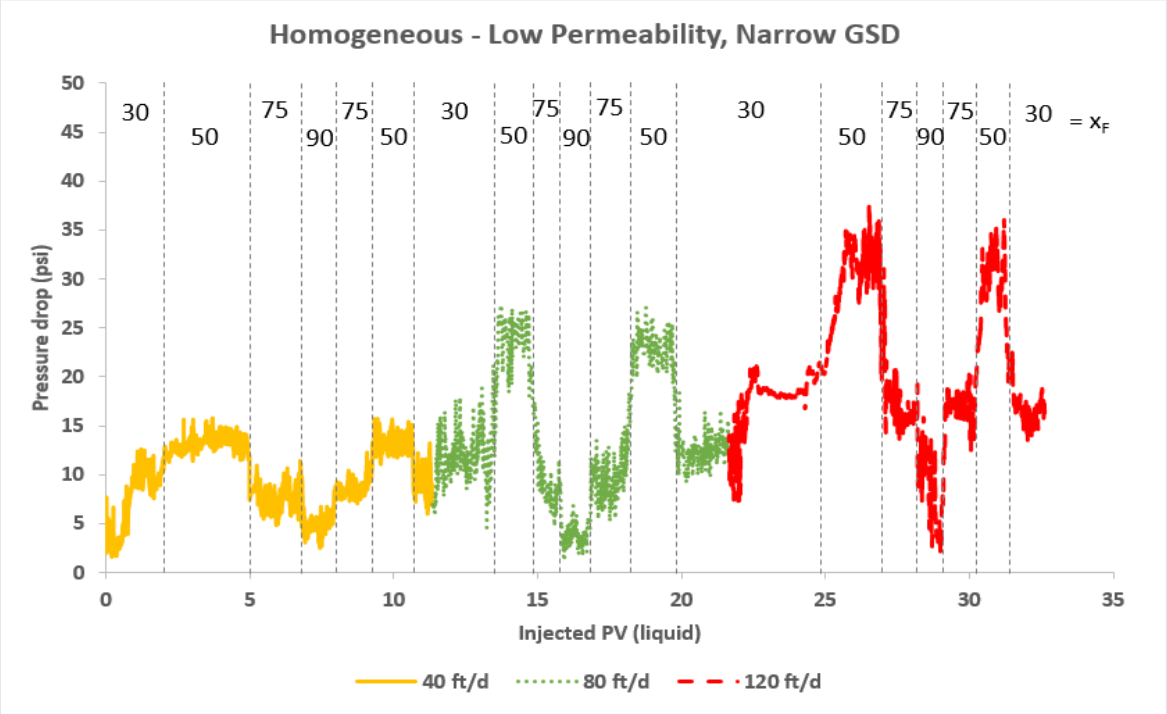

Figure 3.8 – Pressure Drop at Varying Rates and Qualities for Homogeneous, Low Permeability Sand

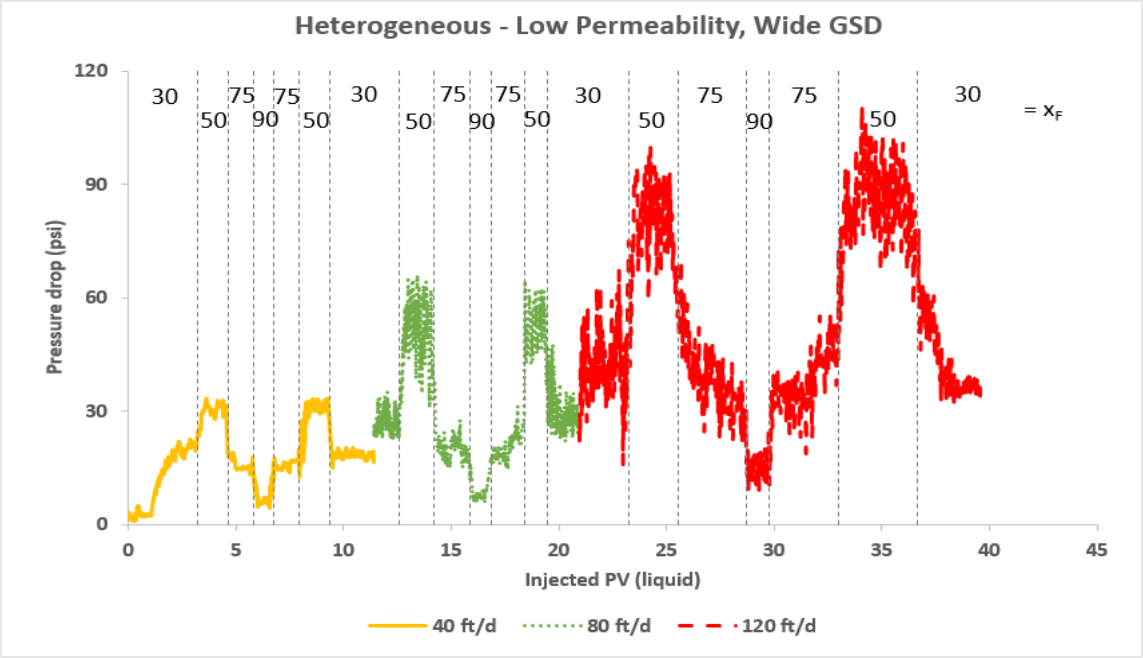

Figure 3.9 – Pressure Drop at Varying Rates and Qualities for Heterogeneous, Low Permeability Sand

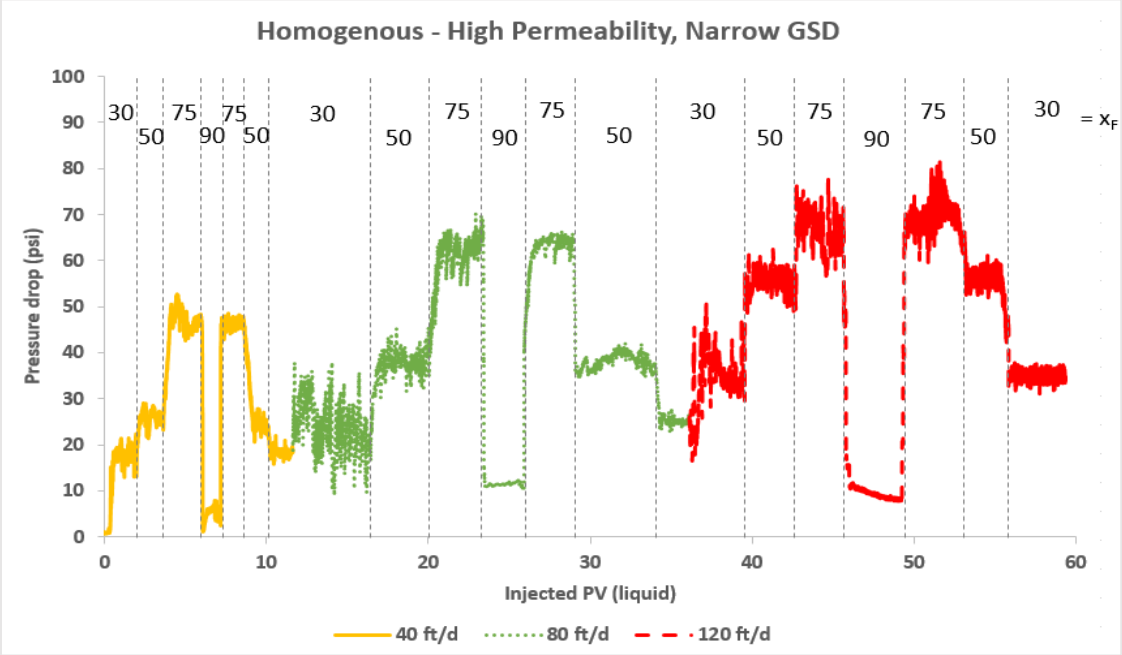

Figure 3.10 – Pressure Drop at Varying Rates and Qualities for Homogeneous, High Permeability Sand

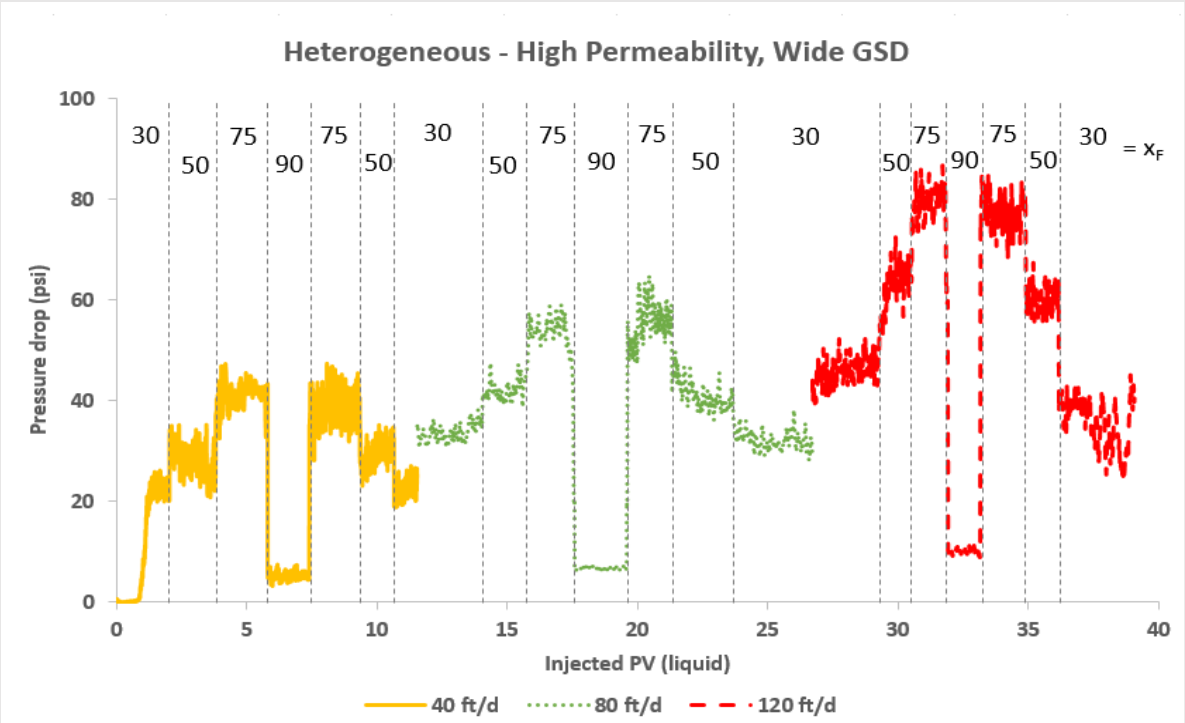

Figure 3.11 – Pressure Drop at Varying Rates and Qualities for Heterogeneous, High Permeability Sand

In general, the high permeability sands lead to greater pressure drops than the low permeability sands. In low permeability sands, the greatest pressure drops were obtained at a foam quality of 50%. This differs in high permeability sands, where a 75% foam quality leads to the greatest pressure drop. These optimum qualities do not differ between sands of varying heterogeneity. These observations, as well as other results, are better analyzed through the mobility reduction factor and the apparent viscosity of the steam foam.

Fig. 3.12 shows the MRF for the homogeneous, low permeability sand. A baseline sand pack flood with only brine and N_2 injection was done only with this first flood. The pressure drops were very low in the water flood due to the high permeability of the sand and the low viscosity of brine at 250°C. For the lowest velocity of 40 ft/day, the pressure drops were so low that the pressure transducers could not accurately measure it. Pressure drop data hovered around 0 psi, with some negative numbers recorded. Therefore, an MRF

at 40 ft/day could not be obtained. For this reason, baseline floods were not conducted for the subsequent three sand pack floods.

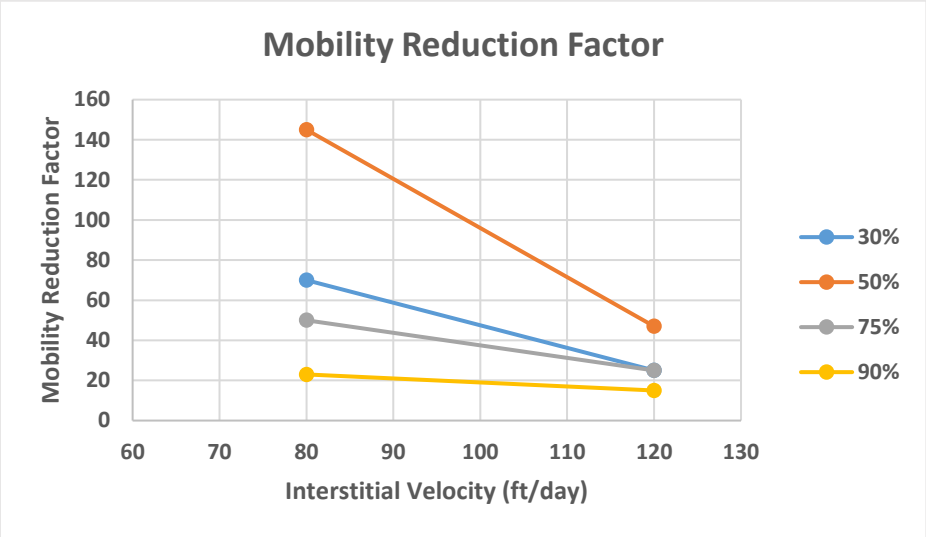

Figure 3.12 – Mobility Reduction Factor of Foam in Homogeneous, Low Permeability Sand

Fig. 3.12 displays the MRF plotted with interstitial velocity. The first observation to be made is that mobility reduction is greater at the intermediate rate of 80 ft/day, and drops when increased to 120 ft/day. This is most apparent when the MRF is high. This is expected, as with a higher velocity, the shear rate increases, making the foam weaker. From the figure, it can be seen that a foam quality of 50% leads to the greatest reduction of mobility. Therefore, foam is strongest in this sand at a quality of 50%. This is the same conclusion made from the pressure drop data, as pressure drop was greatest at 50% throughout the low permeability sands. Foam is weakest at 90% due to the dryness of the foam.

Similar conclusions can be made from the full set of data acquired from calculating the apparent viscosity. The apparent viscosity was calculated from the core flood data, and averages for each quality-velocity pair were determined. These results were plotted with foam quality and interstitial velocity.

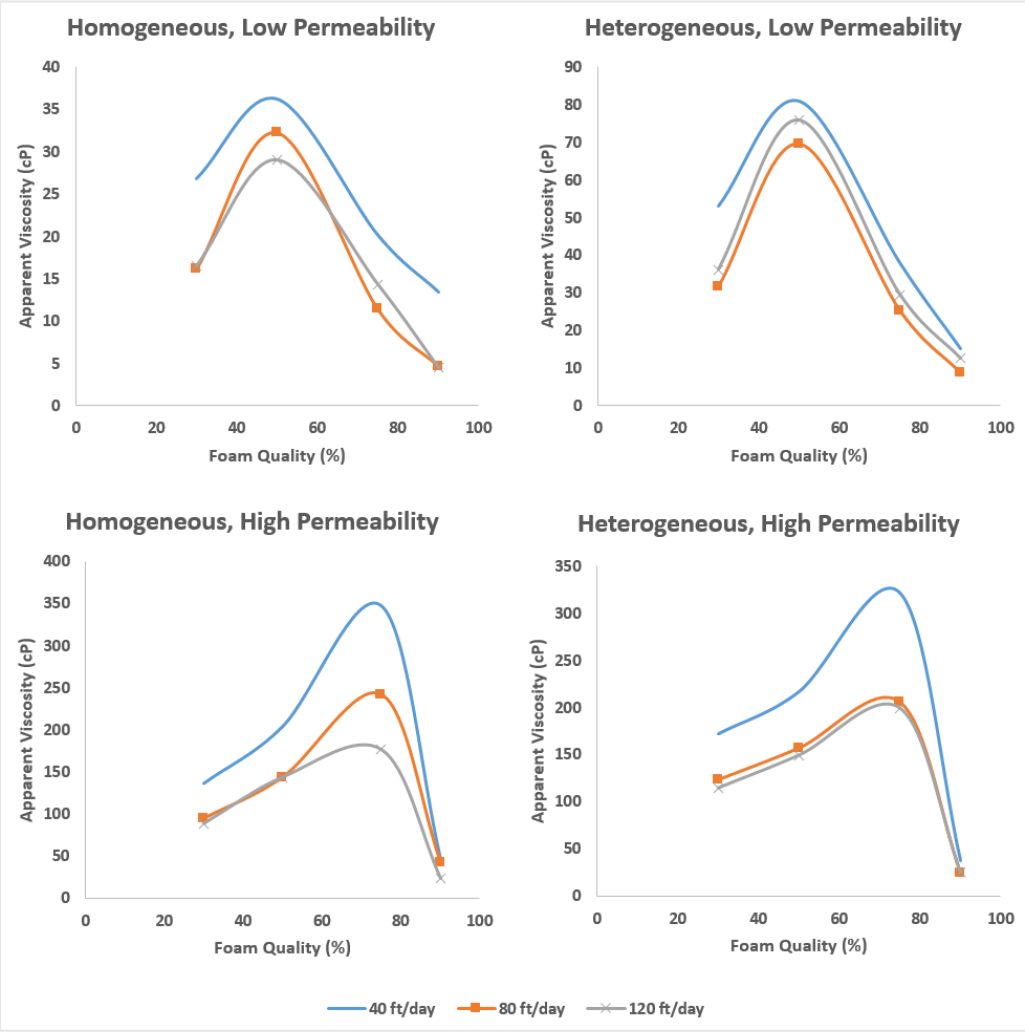

Figure 3.13 – Evolution of Apparent Viscosity with Foam Quality for Each Sand Pack Flood

Fig. 3.13 shows the evolution of apparent viscosity with foam quality in each of the four core floods. The parabolic shape of the apparent viscosity behavior follows the trend illustrated in **Fig. 2.9**. A number of observations were made from the plots. The difference in permeabilities leads to an offset in the optimum foam quality, as well a magnitude difference in the apparent viscosities. The foam viscosities were much greater in the high permeability sands. This result enforces the concept of using foam to reduce mobility in

high permeability zones, in order to divert steam into low permeability, un-swept intervals. Furthermore, when observing the magnitudes of the viscosities, a difference is seen between homogeneous and heterogeneous environments. Lastly, the apparent viscosity drops as the interstitial velocity of the foam is increased. However, there is an exception to this trend in the heterogeneous, low permeability sands due to additional foam generation. This effect is expected and well documented in literature. The drop in apparent viscosity is due to the shear thinning behavior of foam (Hirasaki and Lawson, 1985; Schramm, 1994). Foam behaves as a pseudo-plastic, and as interstitial velocity increases, so does the shear rate, resulting in decreasing viscosities.

The optimum foam quality, x_F*, shifts when the permeability of the sand changes. This observation can be better visualized in **Fig. 3.14**, where the apparent viscosity curves are compared between each core flood at an interstitial velocity of 80 ft/day. As discussed, the low permeability sands lead to an x_F* of 50%, while high permeability sands lead to 75% quality. The optimum foam quality is permeability controlled and is invariant with the injection rate and heterogeneity of the sand. High permeability rocks are typically associated with less grain surface area, and thus, a lower shear rate acting on the flowing fluids. Literature gives that shear rate scales inversely with permeability (Hirasaki and Pope, 1974), such that:

$$\dot{\gamma}_a \sim \frac{1}{\sqrt{k}} \tag{8}$$

where $\dot{\gamma}_a$ is shear rate. Therefore, in high permeability environments, less of a shear thinning effect occurs due to a lower shear rate, resulting in stronger foams. While foam generation is promoted by wetter flow conditions (Rossen, 1999), the weaker shear rate in the high permeability sands allow stable foam generation at 75% gas fraction and foam quality. This is not the case in the constricted pore topology of low permeability sands, where shearing and dry conditions inhibit stable foam generation.

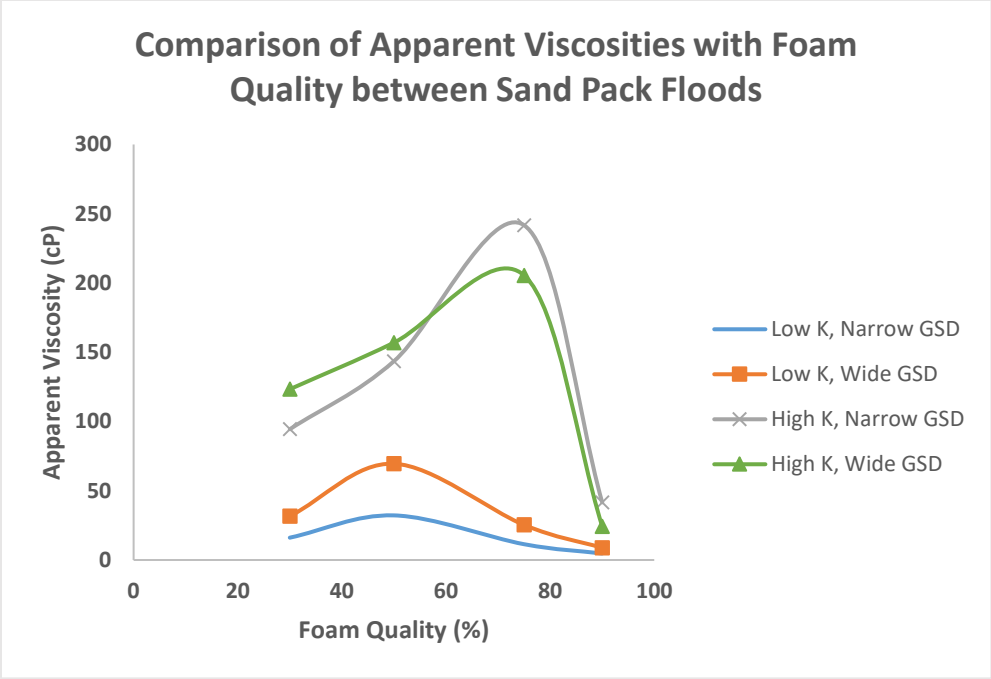

Figure 3.14 – Comparison of Apparent Viscosities with Foam Quality between Sand Pack Floods at 80 ft/day

The core flood data clearly demonstrate that the high permeability sands lead to much greater apparent viscosities, signifying stronger foams. At optimum foam qualities, foam viscosities in high permeability sands can range between 3 to 5 times greater than those measured in low permeability sands. It is well known in literature that foams are more stable in high permeability strata as foam generates more readily. Theory describes that foam generates by exceeding a minimum capillary pressure for entry into narrow pore throats (Gauglitz et al., 2002). Due to this effect, a minimum pressure gradient for foam generation, ∇P_{min}, exists. Rossen gives that ∇P_{min} inversely scales with permeability, k (Rossen, 1990):

$$\nabla P_{min} \sim k^{-1} \tag{9}$$

Tanzil argues that the minimum pressure gradient scales with the square root of the permeability (Tanzil, 2001):

$$\nabla P_{min} \sim k^{-1/2} \tag{10}$$

Overall, however, the minimum pressure gradient needed to be exceeded in the rock decreases as permeability increases. This results in a greater generation of foam in the pore spaces of high permeability strata. Within the homogeneous sands, the effect of ∇P_{min} can result in the apparent viscosity of foams being upwards to 10 times greater in high permeability sands as compared to low permeability sands.

From examining **Fig. 3.14**, it can be observed that the apparent viscosity in both the high and low permeability sands do differ in magnitude. However, there is a difference in whether the heterogeneous or homogeneous environments promote a greater viscosity. In the low permeability systems, the heterogeneous sand leads to significantly greater viscosities. This is the reverse in the high permeability sands, where the homogeneous sand results in greater viscosities. For the low permeability sands, the viscosity difference is greatest at x_F*, but at all foam qualities, the heterogeneous system consistently leads to viscosities 2 to 2.5 times greater than in the homogeneous sand. This relationship is consistent across all flow rates at low permeability. Therefore, in low permeability systems, foams are stronger in heterogeneous porous media, and differences in viscosities between heterogeneous and homogeneous environments are quality-controlled. This effect is due to the local heterogeneity of the sand on the pore-scale. As shown by the results of the sand imaging in **Fig. 3.6**, there is a range of pore throat sizes in the heterogeneous sands. This is supported by **Fig. 3.7**, where the wide range of grain sizes plotted results in a range of pore sizes. Entry capillary pressure, P_c, and ∇P_{min} inversely scale with pore size, and due to the range of pore sizes, there is a range of local capillary pressures. Theory gives that lamellae can be created by brief local fluctuations in capillary pressure, resulting in foam generation (Rossen, 1988; Gauglitz, 2002). Due to the dynamic capillary pressures at pore throats, lamellae are created via snap-off, which depend on both capillary pressure and pore geometry. Due to this condition, constricted pore throats promote snap-off occurrences. Therefore, reservoir heterogeneity aids to promote foam generation due to variations in pore size.

Unlike the low permeability sands, the viscosity relationship between foam generated in the heterogeneous and homogeneous systems in the high permeability sands

is not constant. At low qualities, similar to low permeability sands, the apparent viscosity of foam in the heterogeneous system is greater than the viscosity in the homogeneous sand. Between 50% and 75% quality, however, this observation flips. At higher qualities, the high permeability, homogeneous sand leads to greater viscosities. As x_F* is 75% for the high permeability system, this relationship is the opposite of what was observed in low permeability sands. This is due to the "dryer" quality of the foam. The differing morphologies of the low and high permeability sands lead to two different regimes of foam flow. Due to the differing regimes, the foam behaves differently in the high permeability sands, resulting in stronger foam in the homogeneous environment at high quality. Khatib et al. report that foam stability is limited by capillary pressure (Khatib et al., 1988). They found that there is a transition from strong foam to weak foam when a limiting capillary pressure, P_c*, is reached. Osterloh and Jante describe how high-quality foams closely follow this P_c* model. At high foam qualities, the strength of the foam is controlled by P_c* (Osterloh and Jante, 1992; Alvarez et al., 2001). The capillary pressure increases up to P_c* as foam quality is raised and becomes increasingly dry. As foam quality is increased further, the capillary pressures in the system remain unchanged, while the foam itself becomes coarser and weaker. Literature gives that the capillary pressure inversely scales with pore throat radius, r_t, such that:

$$P_c \sim r_t^{-1} \tag{11}$$

Therefore, in smaller pore sizes, the capillary pressure is greater. Due to the wide range of pore sizes, the heterogeneous sand has a greater number of smaller and more constricted pore throats, as compared to the homogeneous sand. Due to this, fluid flow develops higher capillary pressures throughout the pore network. Flowing liquid and gas, therefore, attain the limiting capillary pressure much quicker, resulting in weak foam generation or existing foam breaking down. Furthermore, as the capillary pressure increases, the work necessary to break lamellae decreases (Overbeek, 1960). A combination of a dry foam, where the amount of surfactant may be too low to stabilize lamellae, and high capillary pressures may result in mechanical disturbances, such as the stretching and contracting of a liquid film as it travels through a pore throat with changing

radius, rupturing the film. This phenomenon does not occur in the homogeneous sand, as greater pore sizes lead to less capillary resistance, allowing foam to form and propagate (Alvarez et al., 2001). As local capillary pressures are lower, P_c* is not reached at the same foam quality. Due to the larger pores in the homogeneous sand, it is able to generate stronger foam and thus develop a greater viscosity, even at high foam qualities. Overall it can be concluded that in high permeability sands, foam is stronger in heterogeneous systems at low quality, but is stronger in homogeneous systems at high quality. This phenomenon in the apparent viscosities is clearly observed when plotted against interstitial velocity in **Fig. 3.15**.

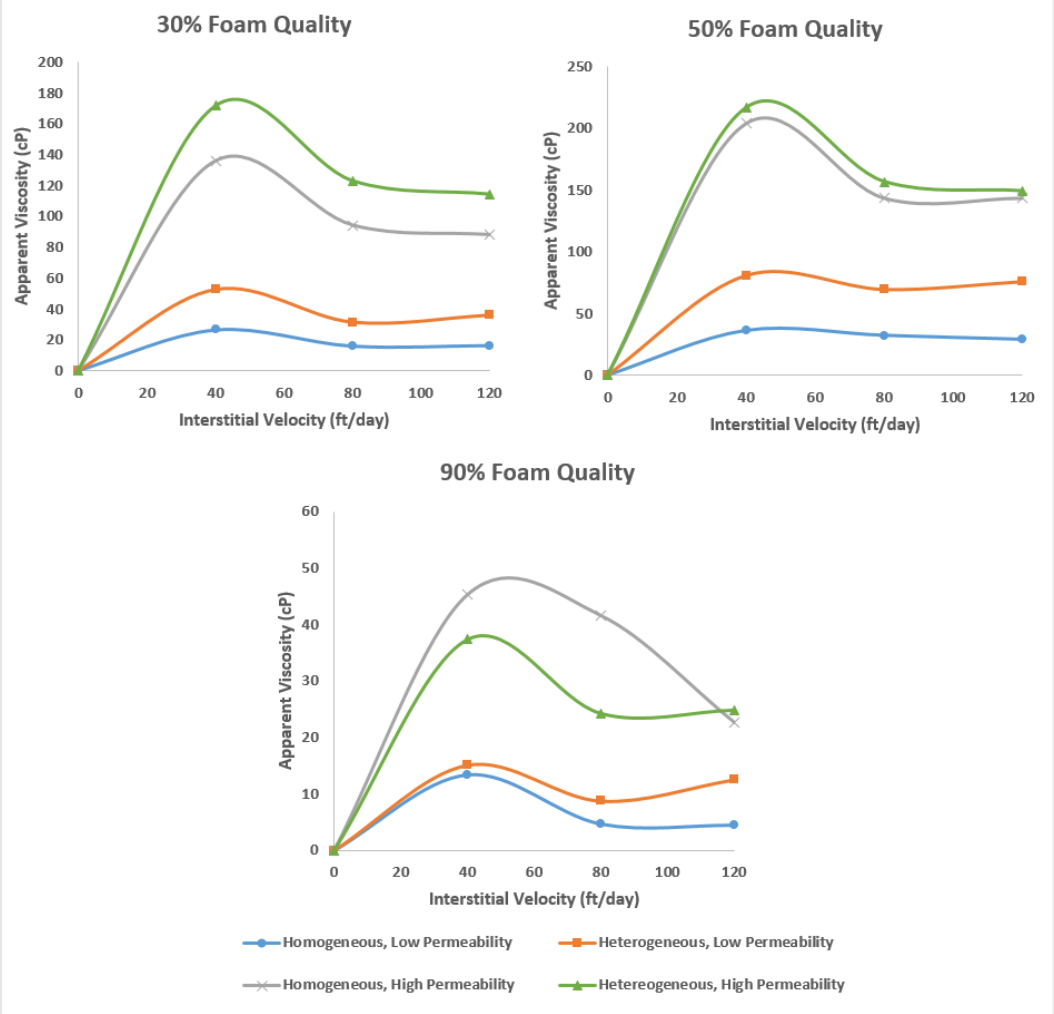

Figure 3.15 – Comparison of Apparent Viscosities with Interstitial Velocity between Sand Pack Floods

Fig. 3.15 plots apparent viscosity with interstitial velocity at fixed foam qualities. As can be seen in the figure, for 30% and 50% foam quality, the offset of apparent foam viscosity between the low permeability homogeneous and heterogeneous sands stays relatively constant as rate increases. A foam quality of 50% gives the greatest difference in apparent viscosities between foam in the two low permeability sands. As observed from the foam quality plots, this is the optimum foam quality in the low permeability sands. The apparent viscosity of foam generated in the high permeability sands was much greater than those generated in the low permeability sands, and the flip in which sand environment produces the greatest foam viscosity is clearly observed. At 30% quality, the foam in the heterogeneous sand leads to a significantly greater viscosity. This gap starts to close in the 50% quality foam, and once higher qualities were reached, foam viscosity in the homogeneous system became greatest. However, at 90% quality and 120 ft/day, the strength of the foam in the homogeneous sand once again drops below that of the foam in the heterogeneous sand. It can be seen that the trends of foam generation and stability were not consistent.

As described in **Fig. 2.10**, strong foams show a shear thickening behavior, where apparent viscosity increases until a critical velocity, v_i*, is reached. Once v_i* has been reached, foams show a shear thinning behavior at higher velocities. This follows a typical power law behavior after the maximum viscosity is obtained. The results in **Fig. 3.15** generally do not exhibit the typical power law behavior, except in the low permeability, homogeneous sand. The apparent viscosity trend of steam foam in the low permeability, homogeneous sand does show a classic shear thickening and shear thinning behavior. This is most evident at 90% foam quality. The viscosity trend of foam in the low permeability, heterogeneous sand shows a shear thinning behavior when the velocity is increased from 40 to 80 ft/day, but viscosity then increases as the rate is increased further to 120 ft/day. This phenomenon can be, once again, attributed to the local heterogeneity of the sand on the pore-scale. Due to the range in pore throat sizes in the heterogeneous, poorly-sorted sand, there is a range of ∇P_{min} and P_c that needs to be overcome by the injected fluid to

generate foam in the pore spaces. Similar to capillary pressure, the minimum pressure gradient inversely scales with the pore throat radius such that:

$$\nabla P_{min} \sim r_t^{-1} \tag{12}$$

The more constricted a pore throat, the greater the capillary pressure, and thus a greater force is needed to enter the pore throat and generate foam. At low velocities, the flow of steam foam does not have enough force to flow through tighter pore spaces. Therefore, foam generates and propagates within larger pore throats. Once a higher velocity is reached, the shear thinning effect takes place on the existing, decreasing its apparent viscosity. This is observed when the rate is increased from 40 to 80 ft/day. However, due to the increased velocity around 80 ft/day, the injected fluid now has enough force to overcome the local minimum pressure gradients and capillary pressures in the tighter pores, allowing steam foam generation and propagation. This effect results in an increase in apparent foam viscosity. The new generation of foam in smaller pore throats offsets the shear thinning effect of foam in the larger pores, resulting in the increase of apparent foam viscosity in **Fig. 3.15**. This is not observed in the low permeability, homogeneous sand, where the pore sizes are relatively constant.

A similar phenomenon is observed in the high permeability sands, both homogeneous and heterogeneous. However, rather than cause an increase in apparent viscosity, the new foam generation in tighter pores results in a constant viscosity. This is seen in the relatively flat, level portion of the high permeability curves at higher velocity in **Fig. 3.15**. This observation suggests that new foam generation perfectly offsets the shear thinning of foam in the larger pore spaces in the core flood experiments. An injection rate of around 80 ft/day appears to be the velocity needed to overcome ∇P_{min} in a critical number of smaller pores to trigger enough foam generation to offset the shear thinning effect. This trend is seen across all foam qualities; however, it deviates at 90% foam quality for the high permeability, homogeneous sand. There is no new foam generation to offset the decrease of apparent viscosity at higher velocities. However, this is not representative of a shear thinning foam either, as the drop in viscosity is not following a power law

relationship. Rather than foam viscosity decreasing due to shearing, foam is being destroyed. Foam destruction occurs when lamellae rupture, in part, due to the lack of surfactant in the liquid to stabilize the film. At 90% foam quality, the foam is quite dry, and so there is not enough liquid and surfactant to sustain foam lamellae, causing foam destruction and a subsequent drop in its apparent viscosity. This is not observed in the heterogeneous sand, as the fluctuations in ∇P_{min} aid in the creation of lamellae. Therefore, wet (lower quality foam) and heterogeneous environments promote the generation of steam foam through continuous lamellae generation in large and tight pore throats.

Overall, this study was successful in determining the effect of sand microheterogeneity on steam foam rheological behavior. A number of conclusions have been made from the results and analysis of the CT imaging and sand pack floods. From the successful application of the grain size distribution results in aiding to interpret trends seen in the sand pack floods, it is concluded that the use of CT imaging has the potential to build a better understanding of the system that steam foam is injected into. With better understanding, the potential for a better optimized design exists.

The purpose of steam foam to lower the mobility of steam significantly in high permeability zones, while allowing steam flow in low permeability zones, was confirmed. It was determined that steam foam has the greatest apparent viscosity at lower rates. High rates by the injection well would increase foam mobility and thus improve foam injectivity. With lower rates far into the formation, foam can stabilize and generate, reducing mobility. The optimum foam quality is offset between low and high permeability sands.

The optimum quality is greater in high permeability sands due to the shear rate of the flowing foam. Lower shear rates at higher permeability lead to strong, stable foam formation at higher qualities and dryer conditions. The foam quality can be optimized in field application with regards to this relationship. The microheterogeneity of a rock affects the generation of steam foam. In low permeability rocks, a heterogeneous rock leads to higher apparent viscosities that remain relatively constant even at high injection rates in low permeability rocks. In high permeability rocks, this relationship is only seen at low

foam qualities. At higher foam qualities, where the foam is dryer, the poorly-sorted environment of heterogeneous systems inhibits the formation of foam. At sufficiently high rates, the apparent viscosity of steam foam remains constant or increases. Due to the range of pore throat sizes in a poorly-sorted environment, there is a range of minimum pressure gradients within the rock. Local fluctuations of pressure gradients and capillary pressures result in further generation of foam at higher flow rates, offsetting the shear thinning effect. While the microheterogeneity affects the generation of foam, steam foam rheological behavior is more sensitive to the permeability of the rock and quality of the injected steam. Differences in permeability result in changes in the optimum foam quality and greatly impact the magnitude of the apparent viscosity. Furthermore, the growth and decay of foam viscosity are largely governed by quality, rather than rate.

This study has added knowledge and understanding of the behavior of steam foam in highly complex systems and reservoirs. However, more work needs to be conducted to better understand these relationships in representative rock cores, rather than sand packs. Through a better understanding of the physics of steam foam, steam foam as a thermal EOR process can be better designed, optimized, and utilized in oil recovery operations.

Chapter 4 Low Permeability Rock Cores

This chapter covers the second phase of the study, in which consolidated rock cores were used. Chapter 4 discusses the experiments conducted using low permeability rocks. This chapter provides a discussion of the purpose and research objectives of this phase. A detailed description of all the experimental methods is given, and how they differ from those processes described in Chapter 3. Finally, results are presented, and the data are discussed. Due to the difficulties with low permeability rock cores, this phase of the study was discontinued, and work with high permeability rocks is proposed in Chapter 5. Furthermore, due to difficulties with CT imaging of consolidated rocks, other methods were proposed to determine rock properties, which are discussed in Chapter 5.

4.1 Purpose and Objectives

The studies conducted using sand pack experiments revealed novel results and behaviors of steam foam. The purpose of transitioning to rock cores was to continue and up-scale the study of the effect of rock morphology on steam foam rheological behavior. Consolidated rock cores were used to validate the results from the sand pack floods in order to assess if sand pack floods are an accurate and effective testing method for steam foam efficacy. The study continued to investigate the effect of both permeability and microheterogeneity (through the use of grain and pore size distributions) on steam foam rheology. Up-scaling to more realistic reservoir conditions from idealized sand packs was done by sourcing a number of sandstones with varying permeability and degrees of heterogeneity. Compared to consolidated reservoir rocks, sand packs are both micro- and macro-homogeneous. They are made up of one mineral, with similar grain shapes, and are uniform. By transitioning to a consolidated rock, the environment in which steam foam is tested is more heterogeneous. The rock environments are heterogeneous on both the micro- and macro-scale, with abundant mineral variation and the presence of layering. Therefore, the objectives of the core floods were to study the steam foam rheological behavior in increasingly complex environments, moving closer to mimicking reservoir conditions.

Core floods were conducted in a similar fashion to the sand pack flood. Each core flood tests a total of three interstitial velocities and the same four foam qualities that were selected for sand pack floods. Apparent viscosity and MRF data were used to draw conclusions on steam foam physics and rheology.

Real reservoir rocks are much more complex than idealized sand packs. The pore network is tighter and more complex. The rocks are not made up of one mineral, as opposed to the quartz sands. Consolidated rocks also react differently to high-temperature environments as compared to sand. The geochemical and thermal reactions were investigated. This includes fines migration and mineral dissolution into the foam and surfactant solution and any destabilizing effect that dissolution may have on the injected fluid. The objectives of this area of the study were to determine the effects of continued foam injection into a core at high temperature and to investigate how the core and injected solution change from their initial condition to after a core flood.

Furthermore, the work conducted using CT imaging was successful when used with sand packs. Likewise, with the core floods, the work aimed to further develop CT imaging and up-scale it for use with consolidated rock cores. CT imaging has been used widely to study the morphology and geology of rocks, and thus, hold the potential for the same in this study. The objective of expanding the work on CT scanning was to develop an accurate methodology for analyzing a rock's pore size and grain size distributions and to develop a link between the PSD and GSD and the results of the core flood experiments, in order to develop strategies to predict the behavior of a steam foam based on rock morphology.

4.2 Materials and Methods

Three rocks were selected for the purpose of studying the effect of increasing porous media heterogeneity on steam foam rheology. Two Berea sandstones and a Buff Berea sandstone were acquired for the purpose of these core floods. These rocks are shown in **Fig. 4.1**. Berea sandstones can vary significantly in permeability and microheterogeneity (Churcher et al., 1991). Of the two Berea sandstones acquired, one was low permeability,

and one was high permeability. The low permeability had a permeability of 250 mD to air, while the high permeability was 500 mD to air. They were selected in order to isolate the permeability effect. These Bereas have a high degree of microheterogeneity. They are also heterogeneous on the macro-scale. It can be observed in the Berea images in **Fig. 4.1** that the Berea has subtle streaks across it, signifying layering. The Buff Berea had a higher permeability of 200 mD to brine. This sandstone is more heterogeneous than the Bereas, which can be seen from the specks of darker mineral on the rock surface in **Fig. 4.1**.

Figure 4.1 – Rock Samples; Low-k Berea, High-k Berea, and Buff Berea

4.2.1 Rock Imaging

The process to scan the rock samples followed a similar method to what was used for sand samples. CT imaging was utilized to capture the actual distributions of grain sizes for each of the core samples. This involved taking images using a CT scan and using segmentation techniques to separate the pore space from the grains in the images. The pore spaces were then analyzed for their size and diameter was calculated, and the frequency of diameter sizes was plotted to obtain the distribution. The images allowed the qualitative visualization of the range of pore sizes, and thus was utilized as a comparative method for different rocks. To analyze the CT scanned images, Fiji ImageJ, an image processing and analysis program, was utilized.

The following is a procedure using UT PGE's CT scanning apparatus and Fiji ImageJ. First, a 1-cm^3 block sample was taken from the rock. **Fig. 4.2** shows a photo of

one of the rock samples with its dimensions. This small cube was run through the X-ray CT scan to obtain thin, 2D image slices of the sample. Fiji ImageJ was then used to process the scanned images to obtain the PSD. The image contrast was enhanced to differentiate between grain and void space, and segmentation was applied to divide the data into two phases: solid and void.

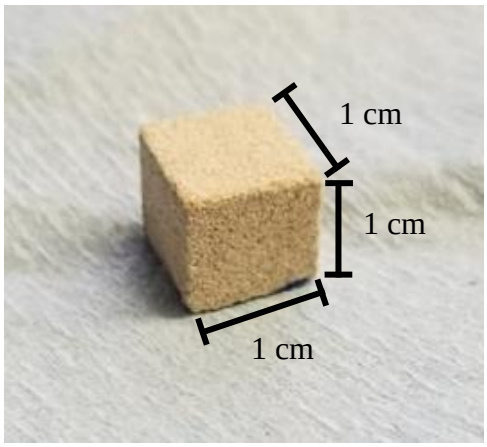

Figure 4.2 – Cubical Rock Sample for CT Scanning

To determine the PSD of each of the rock samples, the area covered by the individual pores was measured in pixels for all images. There were approximately 1,500 images for each of the rocks. Using a MATLAB script and assuming spherical pore spaces, each individual diameter was calculated by converting from pixels to microns. A final distribution was obtained by plotting a histogram of all the results for all images within one rock sample.

4.2.2 Core Floods

Core flood experiments were conducted at 200°C and 500 psi back-pressure. This was lower than the sand pack floods due to equipment limitations. The core holder is more complex than a simple sand pack holder, and its systems of seals are generally not rated for temperatures greater than 200°C. Foam performance was determined by the measured pressure drop across the core. The pressure drop is an indication of foam strength and

propagation and was used to later calculate the apparent steam foam viscosity, μ_{app}. The core flood experiments were conducted in the absence of oil, as the effect of rock heterogeneity was targeted, without the interference of the destabilizing effects that oil has on foam. Each core flood was conducted at a number of foam qualities and interstitial velocities. The fluids were injected into the cores at 10, 20, and 30 ft/day for the chosen sandstones. These rates were selected based on the ones used for the sand pack, with the aim of achieving the same shear rate at a lower permeability. An equation relating the apparent shear rate to porosity and permeability was utilized (Hirasaki and Pope, 1974):

$$\dot{\gamma}_a = \left(\frac{3n+1}{4n}\right)^{\frac{n}{n-1}} \frac{12u}{\sqrt{150k\varphi}} \tag{13}$$

where $\dot{\gamma}_a$ is the apparent shear rate, *n* is the bulk solution power law index, and *u* is the Darcy velocity. By keeping $\dot{\gamma}_a$ constant and using the relation following relation between interstitial velocity *v* and Darcy velocity:

$$u = v\varphi \tag{14}$$

The above equation was simplified to:

$$v_{sandpack}\sqrt{\frac{\varphi_{sandpack}}{k_{sandpack}}} = v_{core}\sqrt{\frac{\varphi_{core}}{k_{core}}} \tag{15}$$

Using this equation, the appropriate interstitial velocity for the core was calculated based on the permeability and porosity of the sand packs and cores. At each flow rate, the foam qualities were varied at 30%, 50%, 75%, and 90%. The qualities were increased, then decreased back down to study the effects of hysteresis. The velocities and qualities were controlled by varying the injection rates of the aqueous phase (containing brine and surfactant), and the gas phase (N_2). This was done using the following relations to calculate the gas rates:

$$v_{superficial}\ \left(\frac{cc}{\min}\right) = \frac{30.48 * v_{interstitial}\left(\frac{ft}{day}\right) * A\ (cm^2) * \varphi}{1440} \tag{16}$$

$$v_{gas-core} = v_{superficial} x_F \tag{17}$$

$$v_{gas-pump} = \frac{P_c v_{gas-core} Z_p T_p}{P_p Z_c T_c} \quad (18)$$

where $v_{gas\text{-}core}$ is the gas velocity in the core, $v_{gas\text{-}pump}$ is the pump velocity of the gas, x_F is foam quality, P_c is core pressure, T_c is core temperature, Z_c is the compressibility factor of gas in the core, P_p is pump pressure, T_p is pump temperature, and Z_p is the compressibility factor of gas in the pump. The following relation was then used to calculate the liquid rate for each pairing of velocities and foam qualities:

$$v_{liq-pump} = v_{liq-core} = v_{superficial} - v_{gas-core} \quad (19)$$

Fig. 4.3 shows a schematic of the core flood set-up. It is the same set-up as the sand pack floods, but with additional modifications. A mechanical oil injection system was included to add confining pressure to the core. An additional brine accumulator was also added to streamline the procedure. Within the set-up, the test surfactant is co-injected at 0.5 wt. % in a 1 wt. % NaCl brine with nitrogen as a non-condensable gas. The co-injection of a non-condensable gas improves the effectiveness of a steam foam process. Non-condensable gas extends the lifetime of foam by limiting mass transfer between steam bubbles within the foam. The 1.5-in diameter, 12-in length core was placed within a core holder and was placed in a convection oven heated to 200°C. Absolute pressure transducers were connected to the inlet, outlet, and two side taps on the core holder. This allows for the measurement of the pressure drop at different segments of the core. The transducers used were Omega Engineering USB transducers that connect directly to the computer instead of a DAQ system. An associated program is used to record pressure data. The back-pressure was set at 500 psig to ensure the surfactant-brine solution remained in the liquid state. The injection system includes two pumps that separately feed into two piston accumulators. The pumps displace the surfactant solution out of one accumulator and N_2 out of the other. The injection rates for each pump were chosen and set using the equations discussed previously. The flow of N_2 is controlled by a back-pressure regulator, and both fluids meet downstream of the injection line to be co-injected in the core through a 100-ft coil. The coil is placed in the oven to ensure that the injected fluid would preheat to the target temperature before entering the core. Two thermocouples were placed on the set-up, with

one at the inlet and another at the outlet. Temperature data were recorded to ensure that the injected fluid is reaching the experimental temperature before entering the core.

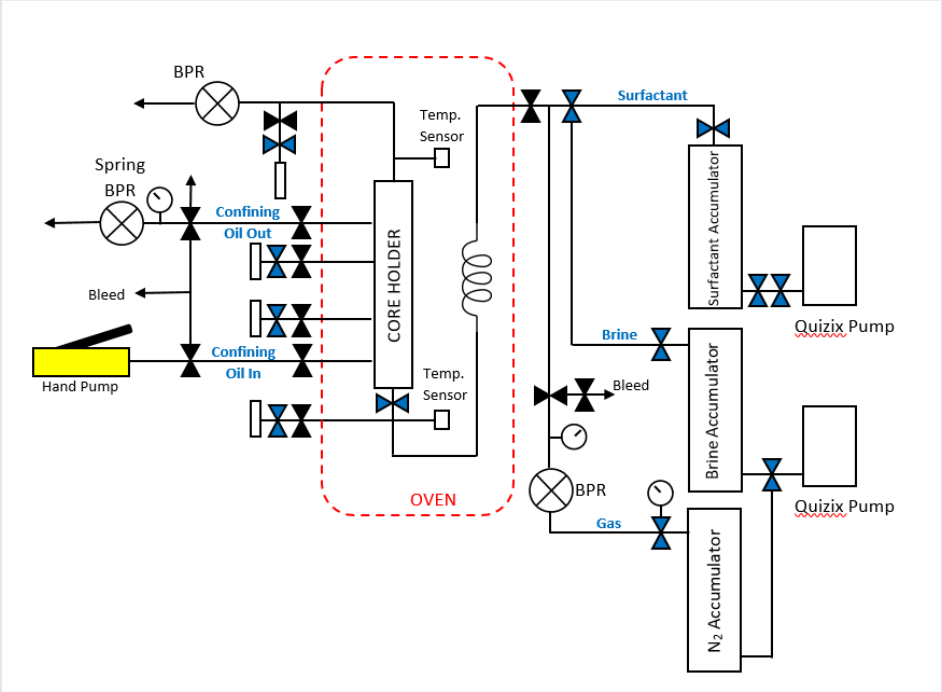

Figure 4.3 – Core Flood Set-Up Schematic

The following presents a procedure for the core floods. The core sample was heated in an oven at 50C to remove any moisture in the pore spaces. It was then loaded into a Phoenix Instruments, high-temperature core holder with AFLAS seals and confining pressure sleeve. AFLAS has a higher temperature rating than the traditional Viton material. The top and bottom pieces were screwed in tightly to add axial pressure. The core holder was mounted into the convection oven, and leak testing was conducted. A confining pressure of 1100 psi was added by manually pumping mechanical oil in the annulus space between the core holder and AFLAS sleeve. Nitrogen was injected into the system above the experimental pressure, and the core holder was monitored for leaks.

The porosity φ and permeability k were measured at ambient temperatures. To measure the porosity, the core holder was placed under vacuum to remove trapped air. A 1 wt. % NaCl brine solution was then injected from the inlet at the bottom of the core holder at a stable rate of 2 PV/day until the pressure inside the core reached experimental

conditions. The slow rate of injection minimized channeling or fingering. Once experimental pressure was reached and maintained by the back-pressure regulator, brine injection was continued at 5 cc/min for about three pore volumes of injected fluid to get rid of all air trapped by capillary trapping. The pore volume was then calculated from the total cumulative injected volume from the pumps, the collected volume after flowing through the core, and the dead volume. The absolute brine permeability was measured. Brine was injected at 1, 2, 3, 2, then 1 cc/min while the pressure data were recorded. The stable pressure drop value at each flow rate was used to calculate the permeability *k* by using Darcy's Law. An average permeability was taken across the flow rates.

The system was then heated to 200°C over a few hours in a step-wise process, in order to minimize expansion stress on the equipment. The temperature data from the thermocouples were monitored to ensure that the experimental temperature was reached. At the start of foam injection, the core was flushed with 4 to 5 pore volumes of a slug of surfactant solution to meet adsorption requirements using a bottom-to-top injection regime. Once a few pore volumes (PV) of slug were injected at a low rate of 2 PV/day, N_2 was co-injected with the surfactant solution to generate foam. The rates of both fluids were controlled to obtain a specific foam quality at the inlet of the core holder. At a specific rate and foam quality, steady-state was reached before changing the rates to obtain a new quality and injection rate. This was done for all three rates and four foam qualities. Foam injection started with the lowest rate of 10 ft/day, and all foam qualities were tested with this interstitial velocity before moving onto 20 ft/day, and then 30 ft/day. Foam qualities were increased from 30% up to 90%, then back down again to 30% before switching rates. The pressure data were recorded throughout the flood.

Once the pressure drop data were collected, the apparent viscosity was calculated using Darcy's law:

$$\mu_{app} = \Delta P_{foam} \frac{k}{v_{darcy} L} \tag{22}$$

where ΔP_{foam} is the pressure drop across the core, k is the permeability, L is the length of the core, and v_{Darcy} is the Darcy velocity. The Darcy velocity is the interstitial velocity multiplied by the porosity of the core. If a baseline flood without foam is conducted, the mobility reduction factor was calculated using:

$$MRF = \frac{\left(\frac{\Delta P_{foam}}{Q_{foam}}\right)}{\left(\frac{\Delta P_{water-gas}}{Q_{water-gas}}\right)} = \frac{\Delta P_{foam}}{\Delta P_{water-gas}} \quad (21)$$

where ΔP_{foam} and Q_{foam} is the pressure drop and flow rate of the flowing foam, and $\Delta P_{water-gas}$ and $Q_{water-gas}$ is the pressure drop and flow rate of the baseline flood. As the flow rates with and without foam were kept the same, the MRF is a ratio of the pressure drops with and without foam. As the pressure drop increases with foam formation, the reduction factor is expected to be greater than 1. The pressure drop, apparent viscosity, and MRF data were used to assess the optimum steam foam conditions for each core system.

4.3 Results and Discussions

Experimentation work on relatively low permeability sandstones was discontinued due to a number of challenges. CT scanning and imaging were conducted for all rock samples; however, challenges were met and addressed to better develop the process used to analyze the pore size and grain size distributions. Despite refining the process, limitations were encountered. The methodology requires further refinement to properly handle and analyze the complexity of the consolidated rocks. Due to this, other methods to characterize PSD were devised and are discussed in the next chapter.

Core flooding commenced with the low permeability Berea. Due to the slow rate at which the foam was injected, the time required for this core flood was long. More than half the data were collected for the 10 ft/day rate, with 30%, 50%, 75%, 90% tested, and 75% tested during the ramp-down process to study the effect of hysteresis. Due to the long time commitment, the core flood was stopped in order to begin steam foam injection into high

permeability cores, discussed in Chapter 5. Thus, work with the Bereas and Buff Berea sandstones were discontinued.

4.3.1 Rock Imaging

CT imaging of the rock samples was successful. An example of the raw CT image for the high permeability Berea is shown in **Fig. 4.4**. The detail in the grains and void space can be clearly seen in the 2D slice image. Using the ImageJ analysis method, each of the images was processed in order to analyze the pore size distribution. It was found that using the same procedure as the one used for sand packs was unsuitable for the consolidated rocks. The left image in **Fig. 4.5** shows a processed image from using the original procedure. In this image, black denotes the pore space, while white denotes the grains. It can be easily seen when compared to **Fig. 4.4** that this image greatly overestimates the amount of pore space in the rock. Due to this, the procedure in ImageJ was refined in order to make it suitable for a consolidated porous medium. The right image in **Fig. 4.5** shows the results of this refinement. It can be seen that the refined procedure successfully processes the CT scans to obtain a more accurate image. Overall, from the sample image in **Fig. 4.5**, it can be observed that the refined procedure used in ImageJ was successful at separating and identifying the grains vs. the pores.

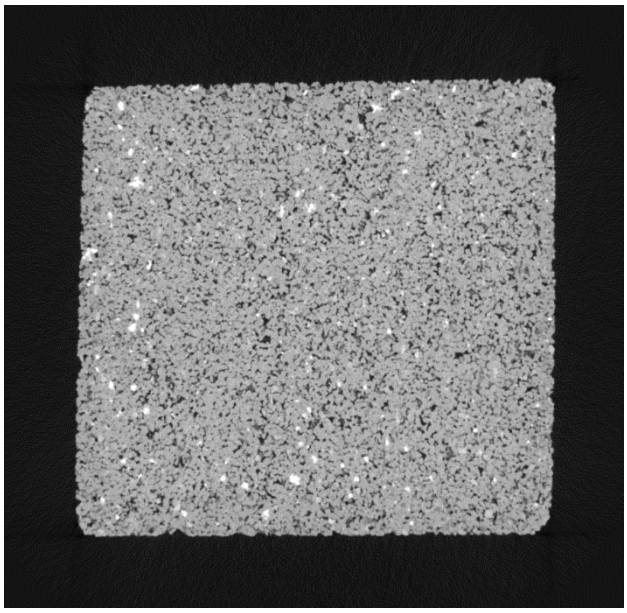

Figure 4.4 – CT Image of 500 mD Berea

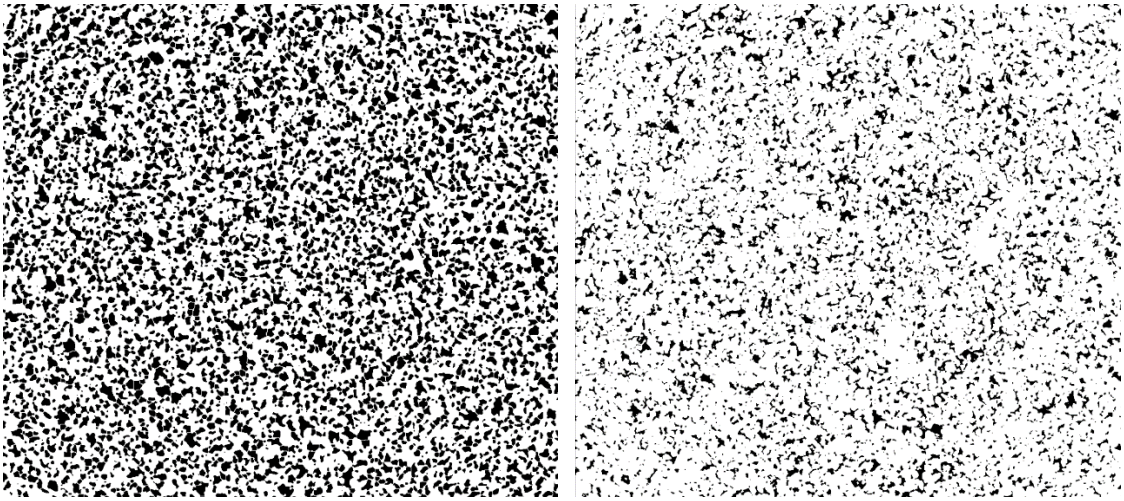

Figure 4.5 – Comparison of Processed CT Images when using the Old vs. Refined ImageJ Procedure

The grain measurements for thousands of images were made and imported into the MATLAB script in order to plot the grain size distribution. **Fig. 4.6** shows the pore size distribution plots for each of the three rocks. The PSD's show a typical distribution shape for pore sizes. However, the results were not as expected. As can be seen in the figure, the

distributions are all nearly identical. The low permeability Berea has a lower frequency of very small pores between 10 and 20 microns in diameter as compared to the other two, but other than that distinction, the plots have near identical frequencies for each of the pore diameter ranges. The Bereas is expected to have different distributions due to the differences in permeability, particularly in the mean of the pore size distribution (Beard and Weyl, 1973). The Buff Berea, on the other hand, is more heterogeneous than the Bereas and is also expected to have a different distribution. It is hypothesized that the frequency of very small pore sizes greatly outnumbers the visible pores. This can be considered as "noise" from the images, where these small pore sizes are specs on the order of one pixel in the image. The procedure requires further refinement to eliminate these smaller sized dots on the image, in order to capture a more accurate distribution.

Due to the challenges in using CT imaging and associated software, conducting classic pore size determination tests such as MICP and NMR was proposed. These methods are used widely in industry and research and are a trusted and robust method to gain information on both pore throat and pore body sizes. The use of these methods allows to accurately gain pore size distributions, as well as the aspect ratio of the pores.

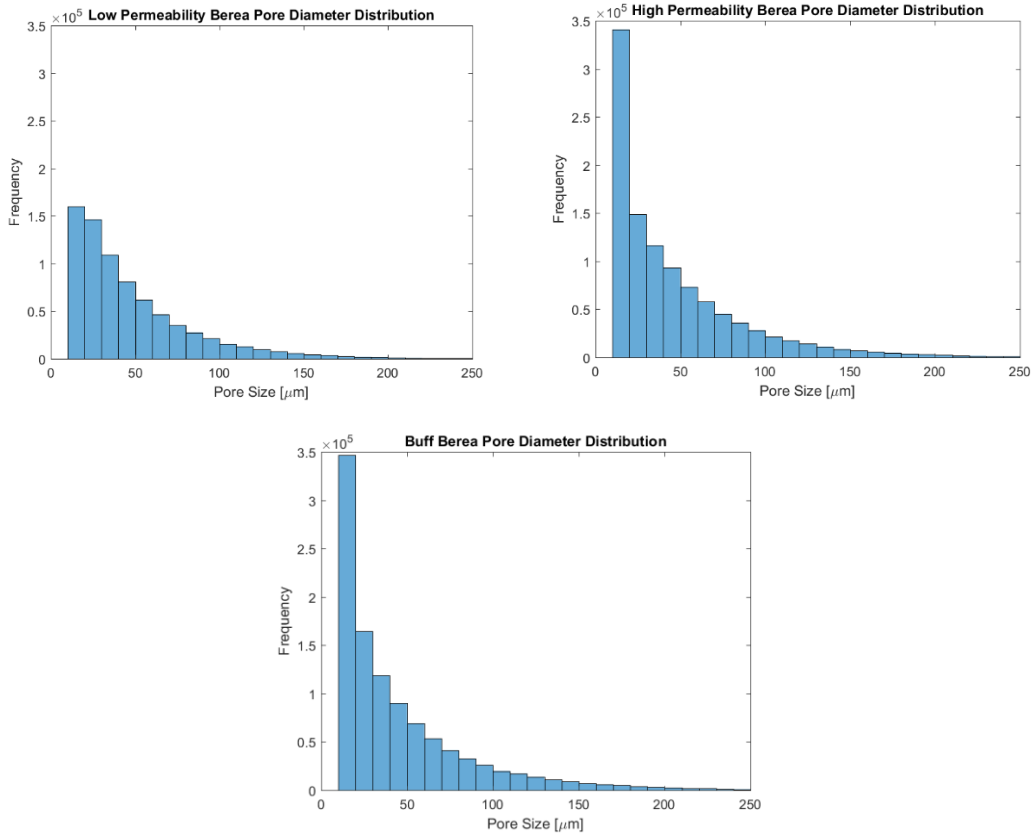

Figure 4.6 – Pore Size Distributions of All Rock Samples

4.3.2 Core Floods

The low permeability Berea core was the first rock selected to test in core flood experimentation. The porosity of the core was 25.1%, and the permeability was 80 mD to brine. The interstitial velocities selected were 10, 20, and 30 ft/day based on the permeability and porosity of the core. Due to the time commitment, only four rates were tested for the initial velocity of 10 ft/day. The core flood was discontinued before completion due to the time commitment. **Fig. 4.7** displays the raw pressure data, with annotations showing the segments for different foam qualities present. Almost 25 pore volumes of liquid were continuously injected over the course of four weeks. A complete core flood would have taken months. It can be seen from the plot that the pressure data became increasingly unstable as time has passed. While the inlet pressure has remained

fairly level, the outlet pressure has fluctuated greatly. This is due to rapid gas expansion in a faulty back-pressure regulator. Despite the poor resolution of the data, it still gave valuable information, as the trends can be clearly interpreted.

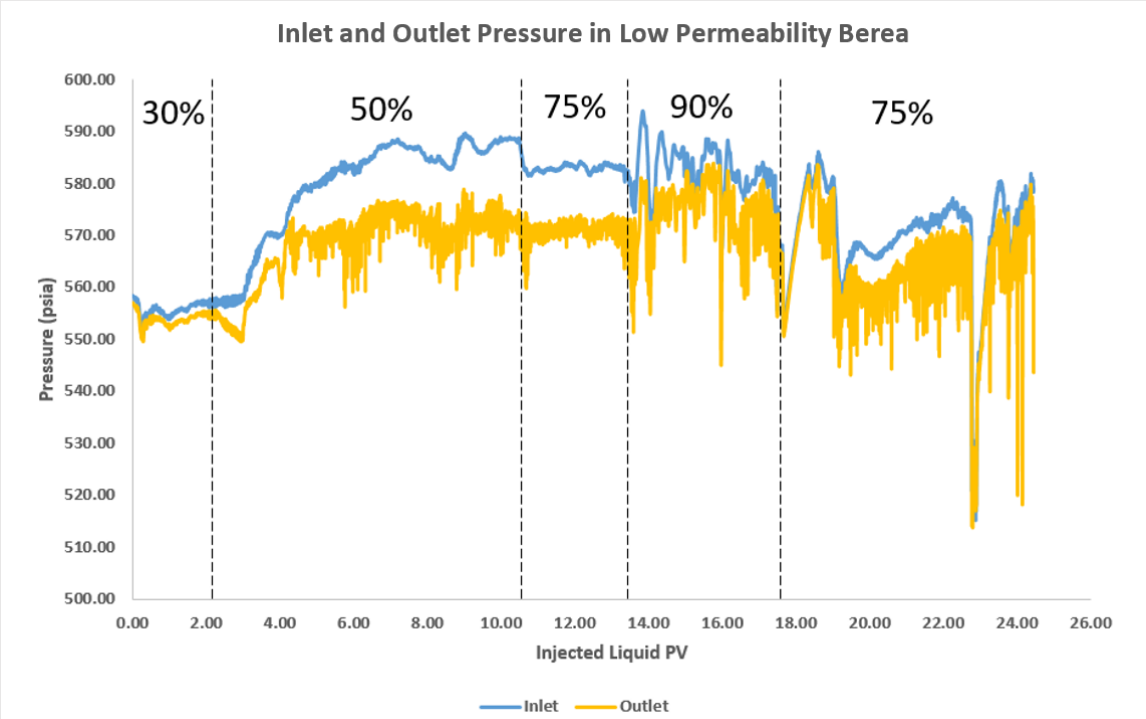

Figure 4.7 – Inlet and Outlet Pressure in Low Permeability Berea

A number of observations were also made from the produced effluent. The produced fluid from the core was a very weak and coarse foam. Furthermore, the fluid had an opaque tan color to it. This is contrasted with the sand pack floods, where stable, strong foam was produced from the core, and the effluent had no discoloration. It is hypothesized that mineral dissolution affected the injected solution, resulting in the discoloration and a weaker foam through surfactant precipitation. The instability of the foam is supported by the apparent viscosity data.

The apparent viscosity of steam foam in this core has been calculated from the available pressure data. **Fig. 4.8** plots the apparent viscosity with injected liquid pore volumes. Similar to **Fig. 4.7**, it can be seen that as more time has passed, the data continue to fluctuate more vigorously. The data show that it has generally taken many PV of injected

fluid to reach an acceptable steady-state. It can be seen that at 30% foam quality, the viscosity of the foam is very low. Most likely, not enough time was given for foam to generate, as this is the viscosity expected if only brine was injected through the core. Water viscosity at 200°C and 500 psi is roughly 0.134 psi, which matches closely with the apparent viscosity at 30% quality. As evidenced, nearly 4 PV of injected fluid is needed to see proper foam formation.

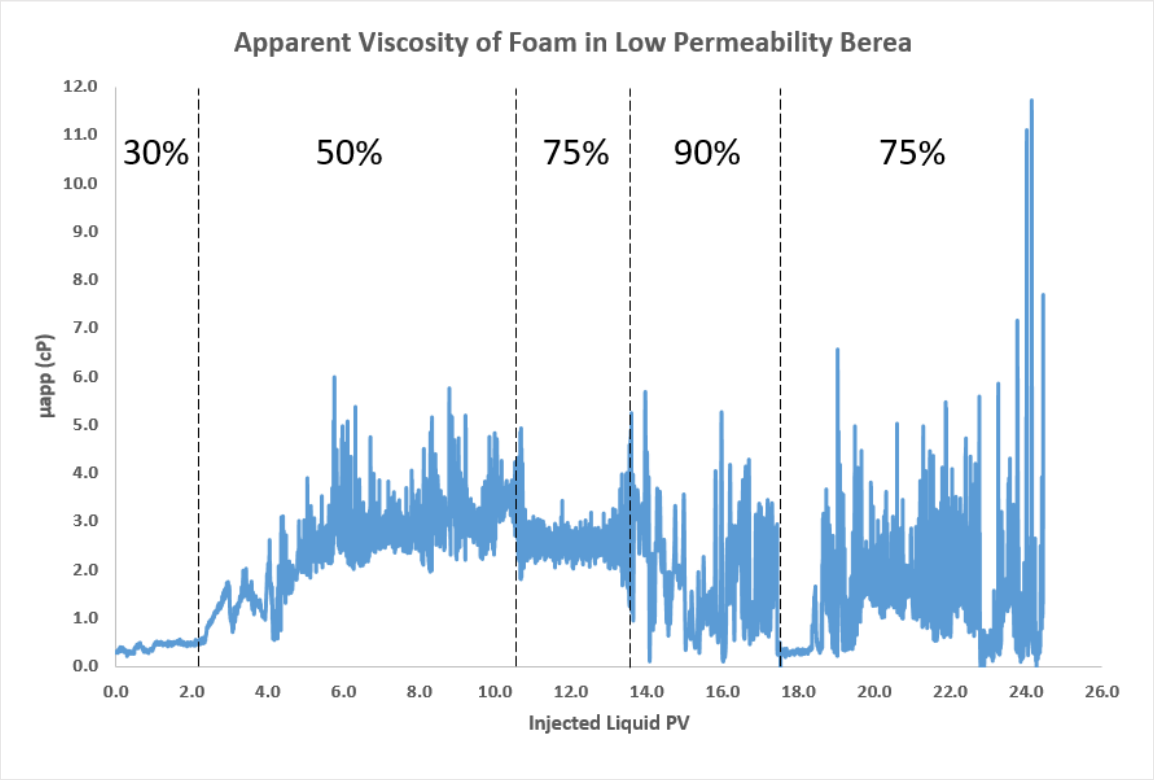

Figure 4.8 – Apparent Viscosity of Foam in Low Permeability Berea

From the viscosity plot, it can be seen that the strongest foam was formed at 50% foam quality. The highest viscosities appear to be between 3.0 and 3.5 cP. As compared to the viscosity of water at these conditions, foam is roughly 25 times more viscous than water at 50% quality. Despite lower viscosities expected in the much tighter rock as compared to the sand packs, the pressure drop and viscosities were much lower than anticipated. The viscosities reached in the sand packs were in the range of 35 to 70 cP in the low permeability sands, and 200 to 400 cP in the high permeability sands. However, data show

that mobility control is feasible in this core due to the contrast between water and foam viscosities at 200°C.

This result may be due to a number of reasons. It was hypothesized that geochemical reactions and mineral dissolution into the surfactant solution greatly affected the performance of the foaming agent. Thermal degradation and adsorption were also considerations. However, data from The Dow Chemical Company showed that the surfactant is stable at high temperatures for weeks at a time. This is shown in **Fig. 4.9**, where a solution of 0.5 wt. % surfactant and 1 wt. % NaCl was kept at 200°C and 250°C under an N_2 atmosphere and measured for their remaining concentration after one and two weeks. At 200°C, the surfactant is still very stable after two weeks, with around 98% of active surfactant remaining in the solution. Furthermore, adsorption should not be significant at this time scale. Testing of the produced solution is required to investigate the effects of possible mineral dissolution.

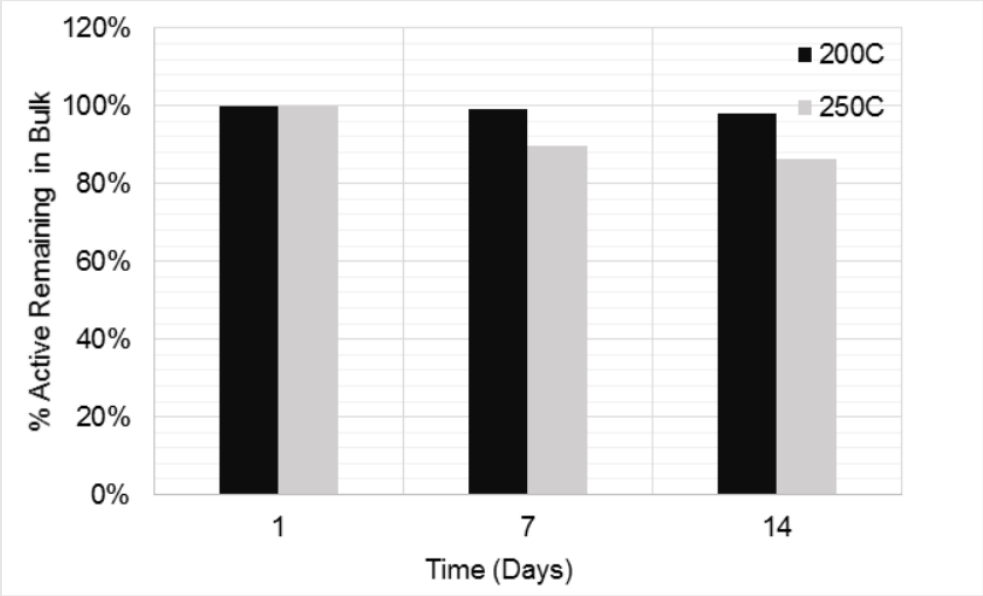

Figure 4.9 – Surfactant Thermal Stability (The Dow Chemical Company)

The apparent viscosity was also analyzed in each individual section of the core. Due to the placement of the pressure taps, the pressure drop could be measured at each third of the length of the core (every 4 inches). **Fig. 4.10** displays the apparent viscosity

across the core in blue, and the apparent viscosity for the middle third of the core, where it is most stable. The purpose of this was to investigate if any end effect was in play. While the middle third has greater fluctuations in the data, it can be seen that the apparent viscosity data closely match between the two sets. It can be concluded from this close match that end effects do not play a significant role in this steam foam injection system.

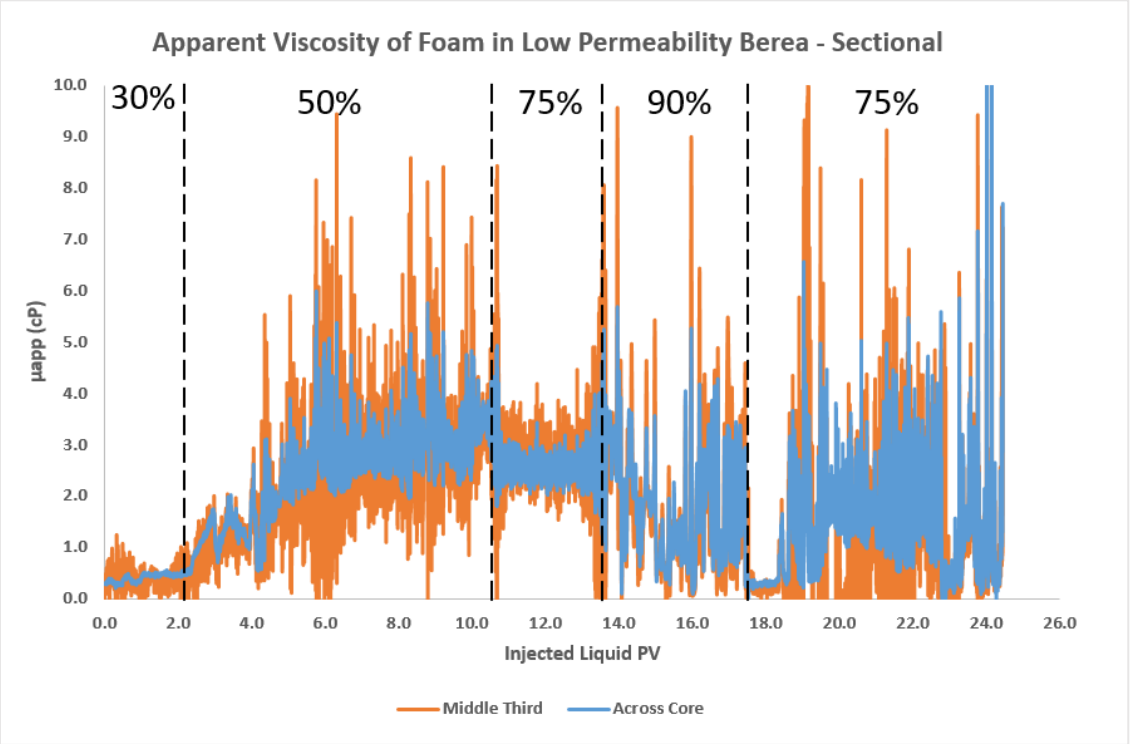

Figure 4.10 – Sectional Viscosity in Low Permeability Berea

Due to the long time requirement of this core flood, it was decided to discontinue this core flood and experimentation with high permeability sandstones was proposed. Due to their high permeability, fluids can be injected into the cores at a greater velocity, and steam foam can generate quicker and reach a pseudo-steady-state sooner. This allows the collection of data quicker and to draw conclusions. Experimentation with Berea sandstones and other low permeability sandstones are recommended to continue in the future as a step to a more complex porous system.

Chapter 5 Rock Characterization

This covers advanced rock characterization techniques used to accurately determine rock properties, such as pore size distribution. The rock characterization tests described in this chapter were designed and conducted to supplement studying foam rheology in a more complex, high permeability, rock environment. The chapter includes a discussion on the motivations and objectives of this study. A detailed description of all methodologies is provided. Finally, a discussion of the results of the experiments and the interpretation of the data is given.

5.1 Purpose and Objectives

The success of the studies to obtain pore size and grain size distributions varied greatly between unconsolidated sand and consolidated rock. CT imaging of small sand samples and processing and analyzing the 2D image slices to obtain the grain size distribution was successful in obtaining accurate and distinct GSD curves for the different sand mixtures. This method was implemented and up-scaled unsuccessfully to characterize consolidated sandstone pore size distributions. While CT scanning to obtain 2D image slices was successful in producing clear images of the rocks, processing them in imaging software with the developed procedure was met with limitations. Despite procedure refinement, due to the complex and consolidated nature of the rocks, the process developed with ImageJ software was deemed unsuitable for consolidated rocks. Work to further refine the procedure was discontinued. However, it was still necessary to obtain information on the morphology of the rocks tested in steam foam core floods.

The purpose of this work was to utilize classical methods to determine and study rock characteristics and morphology. Likewise, with the work undertaken with CT scanning and imaging of consolidated rocks, the focus of this study was on the pore size distribution of the selected sandstones. The PSD of the rocks were used to qualitatively compare different rocks that are used for steam foam flood experiments. By understanding differences in a rock's morphology as compared to another rock, differences in the

behavior of steam foam in the rock environments can be analyzed and explained. As seen from the sand pack experiments, sand mixtures of the same permeability can have very different results in terms of foam rheological behavior and foam strength if the mixtures have different grain size and pore size distributions. Therefore, if the steam foam in two different rocks of similar permeability behaves differently, the pore size distribution of the rocks and its morphologies can be used to interpret these differences in behavior. The work undertaken tests simple methods to gain important morphology and characterization data on the rocks for the purpose of comparison.

This work expanded the study of rock morphology to include investigating the aspect ratio as well. The generation of foam via snap-off is greatly controlled by the aspect ratio of the rock pore network, which must exceed a critical value (Kharabaf and Yortsos, 1998). The aspect ratio is the ratio of the pore body size to that of the pore throat. The critical value for the aspect ratio has been found to be around 1.5 in literature (Li and Wardlaw, 1986). The relative strength of foams can be interpreted by, in part, determining the aspect ratio of a rock pore network.

This was achieved by employing classical rock characterization techniques. Mercury intrusion capillary pressure (MICP) and nuclear magnetic resonance (NMR) was utilized to determine the pore throat sizes and pore body sizes of a rock, respectively. These methods are trusted methodologies in literature to gain many different types of information regarding rock properties.

The objectives of this work were to test and develop simple experimentation techniques with MICP and NMR to characterize a selected rock's morphology through pore size distribution and aspect ratio. Successful use of these methods opens the potential to use MICP and NMR for quick rock characterization used to interpret steam foam core flood data. Establishing a link between PSD and the results of core flooding experiments allows the development of strategies to predict the behavior of a steam foam based on rock morphology.

5.2 Materials and Methods

Two additional rocks were selected for the purpose of studying the effect of increasing porous media heterogeneity on steam foam rheology. A Bentheimer and Castlegate sandstones were acquired for the purpose of rock characterization experiments. These sandstones are of higher permeability and more homogeneous than the Berea sandstones discussed in Chapter 4. These rocks are shown in **Fig. 5.1**. Bentheimer sandstones generally have a brine permeability between 0.5 and 2 Darcy, making them very high permeability rocks (Al-Yaseri et al., 2015; Peska et al., 2015). This sandstone is relatively homogeneous at both the macro- and pore-scale. The mineralogy is composed of a high fraction of quartz, generally between 90-96 wt. %, and a low clay content of below 2 wt. % (Peksa et al., 2015; Shikhov et al., 2017). The clean and homogeneous nature of Bentheimer can be seen in the left image of **Fig. 5.1**, compared to the Castlegate that shows specks of darker mineral on the rock surface. Castlegate sandstones have a lower permeability than that to Bentheimer, upwards to 1 Darcy. It is less homogeneous than Bentheimer, with a quartz content of less than 90 wt. % and a clay content around 6 wt. % (Shikhov et al., 2017).

Figure 5.1 – Rock Samples; Bentheimer and Castlegate

5.2.1 Rock Imaging

CT imaging was utilized to capture the distributions of pore sizes for each of the core samples. This procedure was utilized with high permeability rocks, despite the complications, to demonstrate that the methods developed were inadequate to accurately capture the pore size distribution. This process involved taking images using a CT scan and using segmentation techniques to separate the pore space from the grains in the images. The pore spaces were then analyzed for their size and diameter was calculated, and the frequency of diameter sizes was plotted to obtain the distribution. To analyze the CT scanned images, Fiji ImageJ, an image processing and analysis program, was utilized.

The procedure used to CT scan rock samples was the same as what was used for the Bereas previously. The following is a procedure using UT PGE's CT scanning apparatus and Fiji ImageJ. First, a 1-cm^3 block sample was taken from the rock. This small cube was run through the X-ray CT scan to obtain thin, 2D image slices of the sample. Fiji ImageJ was then used to process the scanned images to obtain the PSD. The image contrast was enhanced to differentiate between grain and void space, and segmentation was applied to divide the data into two phases: solid and void.

To determine the PSD of each of the rock samples, the area covered by the individual pores was measured in pixels for all images. There were approximately 1,500 images for each of the rocks. Using a MATLAB script and assuming spherical pore spaces, each individual diameter was calculated by converting from pixels to microns. A final distribution was obtained by plotting a histogram of all the results for all images within one rock sample.

5.2.2 Mercury Intrusion Capillary Pressure

Mercury intrusion capillary pressure (MICP) methods, also called mercury intrusion porosimetry, are used to determine and characterize the porosity, pore volume, and pore size distribution of a porous medium. This is a mature technology for characterizing a reservoir rock's pore network and is widely used in the petroleum industry

(Abell et al., 1999). Mercury, a non-wetting fluid, is forced into a porous sample at high pressures. Porosity is determined from the volume of mercury intruded into the rock, while the pore size distribution is determined from entry pressure data.

MICP methods involve using a porosimeter and penetrometer. A rock sample is placed into the penetrometer. The penetrometer is loaded into a pressurized chamber in the porosimeter which introduces mercury to the system. The pressurized chamber with the rock sample forces mercury to intrude the sample's void space. Mercury is injected in a step-wise process with increasing pressure. Large pores are filled first, and with additional pressure increases, smaller and smaller pores are filled with mercury. The pore size distribution is determined from the pressure needed to force mercury into the pores and the volume intruded. As entry pressure into a pore is controlled by capillary pressures at pore throats, MICP techniques measure the distribution of pore throat sizes.

As mercury only intrudes capillaries under pressure, the Washburn equation is used to describe the relationship between the pore throat diameter and pressure (Washburn, 1921; Abell et al., 1999):

$$P = -\frac{4\gamma cos\theta}{d} \tag{22}$$

where P is the applied pressure, γ is the surface tension of the fluid, θ is the contact angle of the fluid, and d is the pore diameter. The surface tension of mercury is 485 dynes/cm, while the contact angle is generally assumed to be 130°. Furthermore, this equation simplifies the pore network and assumes that pores are of uniform geometry and are interconnected. The volume of the mercury intruded into the porous material is measured as a function of pressure. These relationships allow the determination of pore diameter distribution with pressure increment and intruded volume.

The following is a procedure using an in-lab UT Micrometrics Auto Pore III porosimeter. First, a core sample of the rock was acquired. The samples for each rock had dimensions of 1-in diameter and 1-in in length. The sample is weighed, and according to

its dimensions, an appropriate penetrometer is selected, such as one shown in **Fig. 5.2**. For the samples acquired, a penetrometer with a 15-cc bulb was selected.

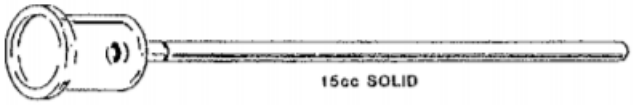

Figure 5.2 – MICP Penetrometer (Micrometrics Auto Pore III Manual)

The rock sample was loaded into the bulb and the penetrometer sealed. Vacuum grease was applied to the lip of the glass bulb to ensure a vacuum-tight seal. The penetrometer with the sample was then weighed. These data were inputted into the associated software. The penetrometer was then loaded into the low-pressure port of the porosimeter to fill the bulb with mercury. The penetrometer was then removed, weighed again, and loaded into the high-pressure port of the porosimeter and sealed. The high-pressure port contains the pressure chamber. Once loaded, pressure was applied in increments by high-pressure fluid, and the porosimeter measured the volume intruded with each pressure increment. The pressure was first increased, then decreased, in steps. Once the process was complete, the penetrometer was removed. The sample was removed, and penetrometer cleaned. Since the rock sample was intruded by mercury, it could not be used again and was properly disposed of. From the raw data obtained and inputted parameters, the porosimeter software processed and plotted all the data for porosity, pore diameter distribution, and other properties.

5.2.3 Nuclear Magnetic Resonance

Nuclear magnetic resonance (NMR) is a mature technology with a wide variety of application in many different industries and disciplines, including in medicine, chemistry, physics, and other sciences. An application of interest of NMR is with rock analysis and imaging in both field and laboratory studies for the petroleum industry. This, too, is a mature technology. NMR is widely used for formation evaluation in the field and for

determining petrophysical properties of fluid-saturated porous media in the lab, such as porosity, fluid saturation, fluid identification, and permeability.

NMR determines properties of the pore space geometry by measuring a signal by an induced magnet moment of hydrogen atoms in reservoir fluid. The signal decay, called the relaxation times, give information about the fluids present and the physical and chemical properties of the rock material (Jackson, 1984; Jerosch-Herold et al., 1991; Knight, 2011). The transverse relaxation time, called T_2, describes the return of a system to equilibrium after disturbance by an electromagnetic pulse. T_2 is a function of the relaxation time of the bulk fluid, pore surface, and diffusion. Due to its relation to the pore surface, T_2 data can be used to gain information about pore body sizes by measuring signals from water within the pores. NMR measurements of rocks give a distribution of T_2 measurements. T_2 distribution curves from water-saturated rocks directly correlate with the pore size distribution of the rock (Marschall et al., 1995; Knight, 2011). T2 can be generally described by the following equation (Kleinberg and Horsfield, 1990):

$$\frac{1}{T_2} = \frac{1}{T_{2B}} + \frac{1}{T_{2S}} + \frac{1}{T_{2D}} \tag{23}$$

where T_{2B} is the bulk fluid relaxation, T_{2S} is the surface relaxation, and T_{2D} is the relaxation due to diffusion in the presence of magnetic gradients. T_{2S} is simply $\rho S/V$, where ρ is the relaxivity of the pore surface, V is the volume of the pore, and S is the surface area of the pore. Through the T_{2S} term, pore sizes are determined from T_2 measurements.

Determining the pore size distribution of a rock through NMR was split into two phases: vacuum brine saturation and measurement of the sample in an NMR spectrometer. In order to obtain T_2 relaxation time measurements of the sample, the rock samples were required to be fully saturated with fluid. Brine was chosen due to the ease of saturation and also to discourage clay swelling in the rock. After fully saturating the rock samples, they were placed in the NMR spectrometer for T_2 measurement.

The following is a procedure using a vacuum saturation set-up to saturate the core with brine. First, a core sample of the rock was acquired, and its dry weight was measured.

The samples for each rock measured 1.5-in in diameter and 3-in in length. This was the maximum size for measurement by the NMR spectrometer, and larger samples sizes result in more accurate measurements. The cores were saturated with a 1 wt. % NaCl brine solution. Due to the low clay content of the Bentheimer and Castlegate, 1 wt. % of NaCl was adequate to inhibit clay swelling. The core samples were placed inside a desiccator, to which a system of vacuum tubing was attached. Tubing was linked to a three-way valve which led to the desiccator, a vacuum pump through a desiccant, and a container of brine solution. The lid of the desiccator is lubricated with vacuum grease before vacuuming and saturation. Once the sample was placed in the desiccator, the chamber was vacuumed using the vacuum pump over several hours. The vacuum pump was switched off, and the valve was turned to allow brine solution to flow into and fill the vacuumed desiccator chamber. Once the core samples were completely submerged in the fluid, the valve was turned again, and the vacuum pump was switched on to degasify the liquid. Introduction of the brine solution to the vacuumed cores theoretically saturates the rocks instantaneously, but the vacuum pump was left on for a few hours to ensure they were fully saturated. Once fully saturated, the desiccator was vented, the lid removed, and the cores lightly dried on the surface and weighed for their wet weight. Using the dry and wet weights of the sample, the porosity of the rock was calculated using a mass balance technique.

For making T_2 measurements to calculate pore sizes, an Oxford Instruments GeoSpec 2 NMR spectrometer was used. After saturation, the core samples were immediately wrapped in cling film to ensure no fluid is lost. Furthermore, due to the moving particles induced by the NMR, the sample warms up during measurement. The cling film ensures no loss of brine through evaporation. The following is a procedure to measure T_2 relaxation time using the GeoSpec 2 spectrometer. Once the sample was wrapped in cling film, it was placed in a glass cell that was then inserted into the NMR spectrometer probe. Dimension information of the sample was then inputted into the spectrometer application, and other settings were set. The NMR then measured T2 once the run was commenced. The spectrometer makes signal decay measurements by inducing a magnetic moment on the brine hydrogen atoms through an electromagnetic pulse. The

NMR spectrometer was made to run 100 scans and to average the measured signal to eliminate any noise in the data. Once the run was complete, the sample was removed from the spectrometer and stored. The T_2 data were exported and was processed to calculate pore size.

The pore sizes were calculated from the T_2 data using Equation 23. T_{2B} for sandstones is 2500 ms, and so, the T_{2B} term is small and can be disregarded (Tandon and Heidari, 2016). For T_2 measurements of water in a water-wet rock, the surface relaxation mechanism dominates, and T_{2D} is very small and can be disregarded as well. As T_{2S} is simply $\rho S/V$, the relation for T_2 then becomes (Kleinberg and Vinegar, 1996):

$$\frac{1}{T_2} = \frac{\rho S}{V} \tag{24}$$

Assuming that the pores are spherical and that the pore surface relaxivity of sandstone is 23 μm/s, the equation can thus be simplified, with r denoting the radius of the pore:

$$\frac{1}{T_2} = \rho \frac{4\pi r^2}{\frac{4\pi r^3}{3}} \tag{25}$$

$$\frac{1}{T_2} = \frac{3\rho}{r} \tag{26}$$

$$r = 69T_2 \tag{27}$$

Using the above equation, the T_2 data were converted into pore size radius and diameter, and the distribution can be then plotted with incremental volume of brine.

5.3 Results and Discussions

Experimentation to determine the pore size distribution of Bentheimer and Castlegate sandstone was successful. Accurate PSD's for the pore throat and pore body diameters for both rocks were obtained using the classical methods of MICP and NMR. The aspect ratio of the rocks was calculated from the data gained from both tests. Along

with CT imaging, quantitative and qualitative comparisons between the two sandstones were made.

Porosity measurements were made during the MICP experiments and the saturation stage of the NMR experiments for both Bentheimer and Castlegate. One sample was tested for MICP, while two were tested for NMR. **Table 5.1** shows the results of porosity measurements for all samples. As seen in the table, the mass balance measurements made from vacuum suturing the core sample were very consistent within one rock. For the Bentheimer, the difference between the two samples was 0.42%, while the difference between the Castlegate samples was only 0.07%. The porosity closely matched between NMR and MICP as well. For the Bentheimer, porosity from MICP was more than 1% greater than measurements from mass balance. While for the Castlegate, the difference was less than 0.15%. Due to the precision of the two methods, porosity measurements were deemed successful. Overall, the porosity of the Castlegate is slightly higher than that of the Bentheimer. Castlegate porosities averaged at 26.45% from mass balance measurements, while Bentheimer was averaged at 24.64%. These figures are consistent with porosity measurements reported in literature (Shikhov et al., 2017).

Table 5.1 – Bentheimer and Castlegate Porosity

Rock	**Porosity (%)**		
	MICP Sample	**NMR Sample 1**	**NMR Sample 2**
Bentheimer	25.93	24.85	24.43
Castlegate	26.54	26.48	26.41

5.3.1 Rock Imaging

CT imaging of the rock samples was successful. Examples of the raw CT images for both Bentheimer and Castlegate is shown in **Fig. 5.3**. The detail in the grains and void space can be clearly seen in the 2D slice image. From the two images in **Fig. 5.3**, it can be seen how distinct the two rocks are. Individual grains appear to be larger and more easily distinguishable from each other from the high permeability Bentheimer. The Castlegate,

on the other hand, appears to be a much tighter rock with a higher degree of compaction. The 2D images are useful in making qualitative comparisons between the two rocks. Using the ImageJ analysis method, each of the images was processed in order to analyze the pore size distribution. Using the procedure developed when processing the Berea sandstone images, the void space and grains were successfully segmented in the processed CT images for both rocks.

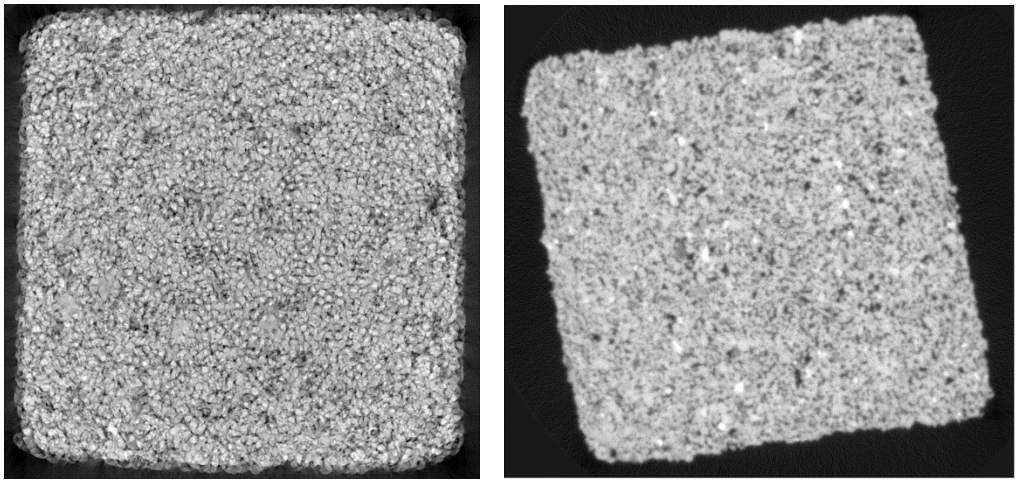

Figure 5.3 – CT Images of Bentheimer and Castlegate

To further demonstrate that the procedure developed in ImageJ was unsuitable for consolidated rocks, the grain measurements for thousands of images of the Bentheimer were made and imported into the MATLAB script in order to plot the grain size distribution. **Fig. 5.4** shows the pore size distribution plots for the high permeability Berea sample from Chapter 4 and the Bentheimer. The figure clearly shows that the results were nearly identical in both frequency and pore diameter range, despite the great difference in the pore network of the two rocks. The Bentheimer is distinctly different from the Berea and is expected to have a much different distribution due to its high permeability and homogeneity (Churcher et al., 1991; Peksa et al., 2015). This exercise further demonstrated the limitations of the ImageJ procedure developed to analyze 2D CT images and confirmed the need for the other methods proposed to determine the pore size distribution.

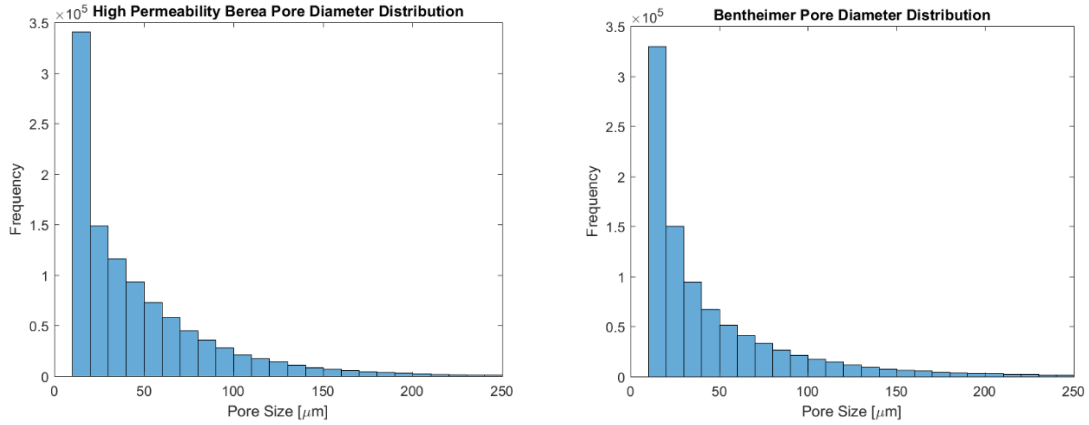

Figure 5.4 – Pore Size Distributions of 500 mD Berea and Bentheimer

5.3.2 Mercury Intrusion Capillary Pressure

MICP experiments with the porosimeter were successful in obtaining pore throat size distribution curves for both Bentheimer and Castlegate sandstone samples. **Fig. 5.5** plots the distributions for pore throat diameter on the same plot. The curves are plotted in reverse for the pore diameters, as MICP measurement intrudes the largest pores first. The figure shows typical distribution shapes for the pore throat diameters of reservoir rocks, which show lognormal distribution. This contrasts with the idealistic sand packs, which exhibited normal or Gaussian distribution curves. Both rocks had a range of pore throat diameters between 0.003 and 100 microns, with the Bentheimer generally having greater pore throat diameters than the Castlegate. The mode of the Bentheimer pore throat diameter distribution is around 33 microns, while that of the Castlegate is 17 microns. This is expected, as Castlegate sandstones are tighter and less permeable than Bentheimer. The data support that Castlegate sandstones have more constricted pathways than Bentheimer. Furthermore, one literature source gives the median pore throat diameter for Bentheimer as 37.49 microns and for Castlegate as 25.21 microns (Shikhov et al., 2017). This is relatively consistent with the results of the MICP tests.

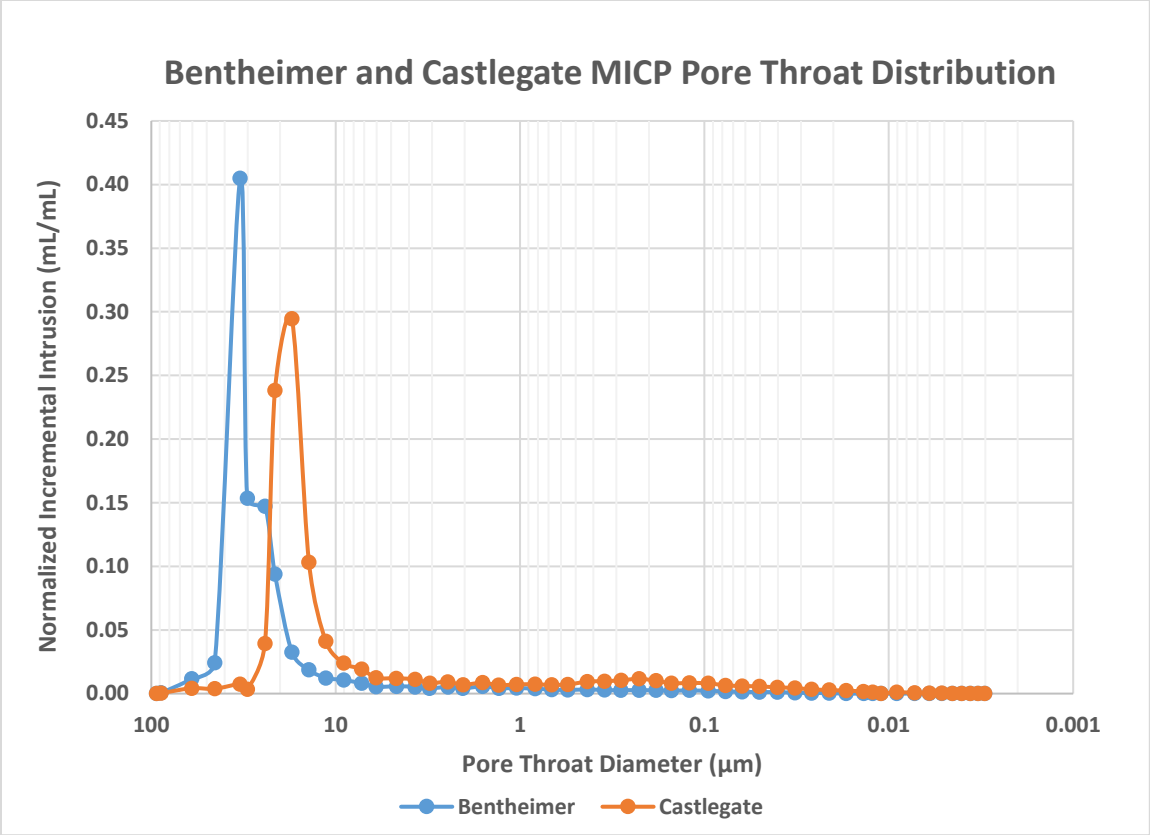

Figure 5.5 –Pore Throat Diameter Distributions of Bentheimer and Castlegate

The distribution of the Castlegate, as discussed, is a typical lognormal distribution. This typical distribution shape is apparent in the Bentheimer as well; however, it is not a perfect lognormal curve, but appears to be bimodal. Fig. 5.6 shows that no additional mercury intruded between pore throat diameters of 20 and 30 microns. This represents that there were no pore throats in this diameter range in the rock. This result suggests that the Bentheimer exhibits a dual-porosity system, where there are two different distributions of pore sizes. The range between 20 and 30 microns represent a range of dead porosity in the rock.

The use of pore throat diameter distributions gained from the MICP tests was successful for qualitative and quantitative comparison of the two sandstone samples, particularly in determining which rock had more constricted pore throats. However, these

data are best coupled with pore body diameter distributions obtained from NMR to gain more information about the pore network.

5.3.3 Nuclear Magnetic Resonance

T2 measurements made with the NMR spectrometer were successful in gaining a relaxation time distribution. These raw data were then exported, and using Equation 27, the pore body radii were calculated. **Fig. 5.6** plots the pore diameter distribution for both Bentheimer and Castlegate sandstones. As opposed to the MICP plot in **Fig. 5.5**, the data are not plotted in reverse order. The range of pore diameters in the Bentheimer range between less than 0.002 microns to 300 microns. The Castlegate pore diameters range between 0.01 and 500 microns. As the figure shows, the Bentheimer has greater pore sizes than the Castlegate. The mode of the Bentheimer pore diameter distribution is around 98 microns, while that of the Castlegate is 48 microns. Once again, this is consistent with the knowledge that Castlegate sandstones are tighter rocks than Bentheimer sandstones.

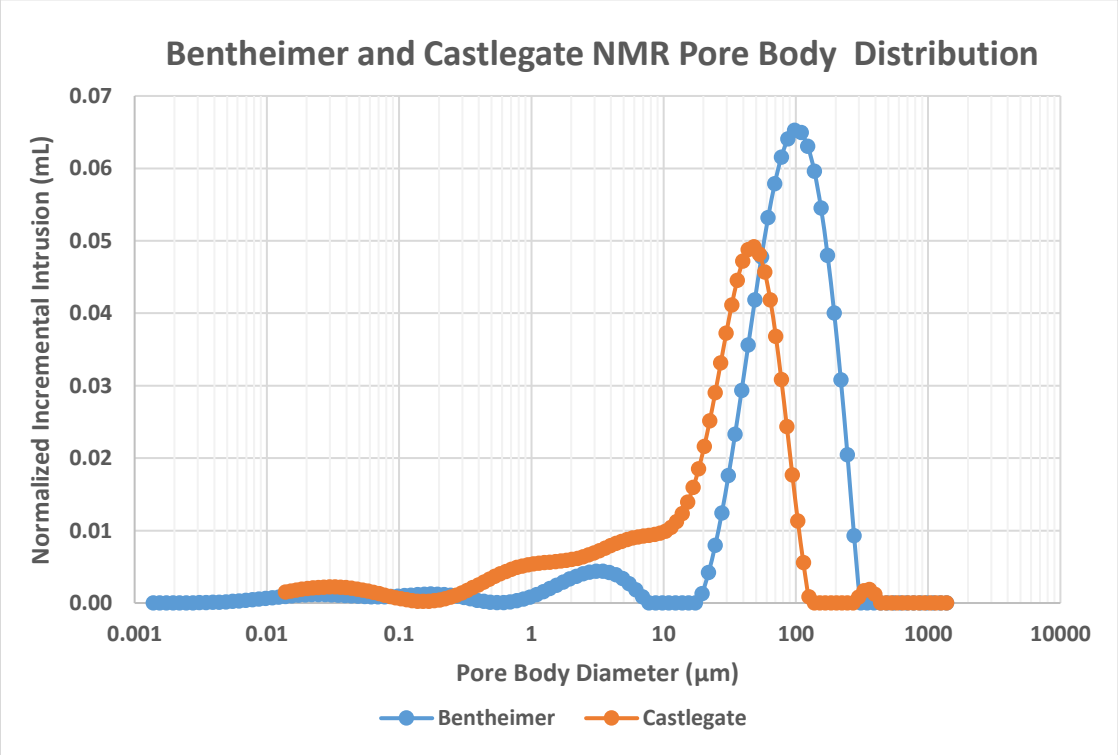

Figure 5.6 – Pore Body Size Distribution of Bentheimer and Castlegate

While showing typical distribution curves for consolidated rocks, the distributions for the two sandstones are very different. The distribution of pore body diameters for the Castlegate shows a typical lognormal distribution. However, there is a range of pore body diameters between 150 and 300 microns that exhibit dead porosity. The number of grains above this range, however, is small and negligible. The tail of the distribution of Castlegate pore diameters is prominent, representing a large number of pores small than 10 microns. In contrast to the Castlegate, the Bentheimer distribution shows a bimodal distribution, with the mode of the secondary porosity at around 3 microns. The bimodal distribution and existence of a dead porosity zone are consistent with the distribution from the MICP test. The secondary porosity zone comprises of a small number of pores, and the vast majority of Bentheimer pores are between 20 and 300 microns.

From the pore body diameter distributions, the bulk of pores in the Bentheimer sandstone is between 20 and 300 microns. This range is between 0.2 and 150 microns for the Castlegate due to the prominent tail in the lognormal distribution. Based on the distributions in **Fig. 5.6**, it was concluded that the Castlegate sandstone has a greater degree of microheterogeneity than the Bentheimer. Even though the Bentheimer has a greater range of pore body diameters, all of these pores are relatively large and within a single order of magnitude. The Castlegate, while also exhibiting large pores, has a significant number of smaller-scale pores. The Castlegate pores are within two orders of magnitude, and this has a greater degree of heterogeneity.

Further conclusions can be made by plotting the distributions from both the MICP and NMR tests. **Fig. 5.7** and **Fig. 5.8** plot the MICP and NMR data on one plot for the Bentheimer and Castlegate sandstones, respectively. As can be evidenced from both plots, the pore diameter distributions from NMR are greater than those from MICP. This is the expected result, as NMR measures the size of the pore body and MICP measures the pore throat. Comparison of these two distributions allows for the determination of pore aspect ratios. By using the mode values for pore sizes, the aspect ratio of Bentheimer is 2.96:1. The aspect ratio for Castlegate is 2.78:1. They are fairly comparable. These aspect ratios exceed those of the critical aspect ratio of 1.5 to promote snap-off to generate foam.

Therefore, both Bentheimer and Castlegate sandstones have the potential for strong steam foam generation and propagation.

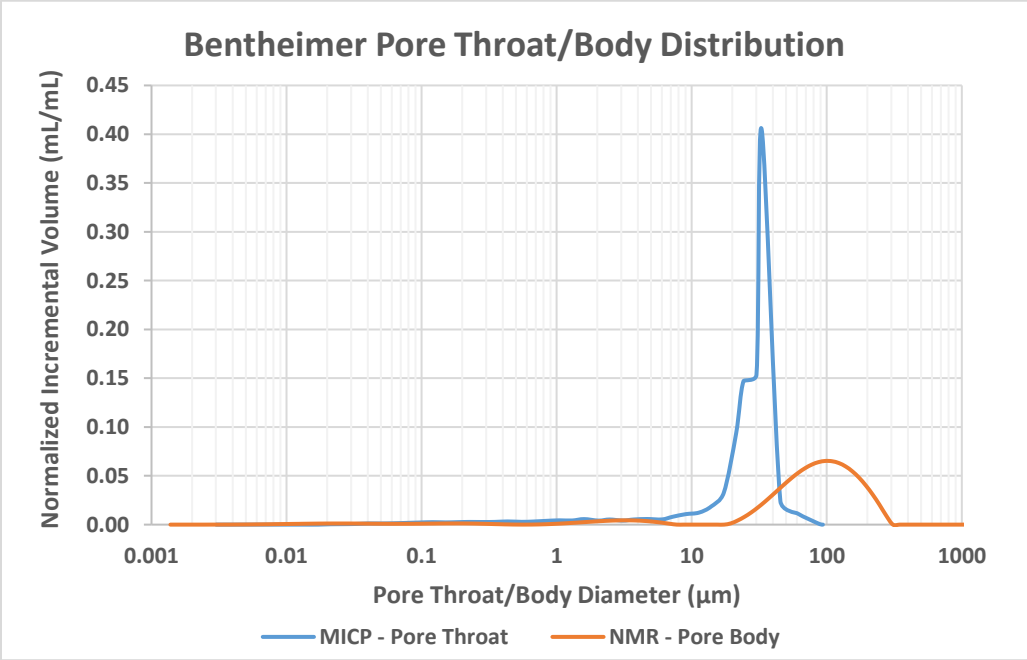

Figure 5.7 – Pore Throat and Body Size Distributions of Bentheimer

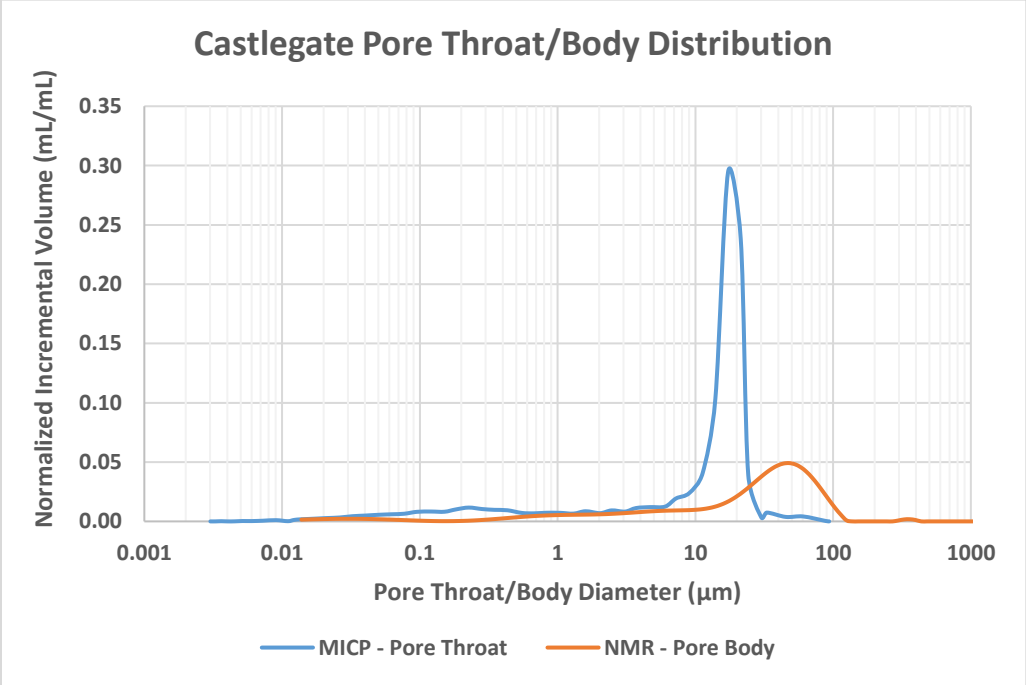

Figure 5.8 – Pore Throat and Body Size Distribution of Castlegate

The results of the MICP and NMR tests show that they have been successful in obtaining accurate pore size distributions for both Bentheimer and Castlegate rocks. These pore size distributions were successful in making qualitative and quantitative comparisons of the two rocks in terms of their relative tightness, heterogeneity, and aspect ratios. Coupling these quick and simple methods for characterizing rock pore networks with steam foam core flood results hold the potential for greater interpretation of dynamic foam test data.

Chapter 6 Conclusions and Recommendations

This chapter discusses in detail the conclusions reached in this study from the interpretation of the data. The chapter presents the conclusions reached and the knowledge developed about the relationship between rock morphology and steam foam rheology. A discussion on the efficacy and limitations of the experimental methods devised is also included. The chapter closes with a discussion on recommendations moving forward to advance the work and widen the scope of the study.

6.1 Conclusions

The purpose of this work was to study and determine the effect of rock morphology, namely permeability and microheterogeneity, on steam foam rheological behavior. This work studied controlled systems made of sand packs to mimic heterogeneous porous media, and correlated grain size and pore size distribution to mechanisms that control steam foam generation, propagation, and destruction. The work also attempted to up-scale this study to more complex consolidated rock cores in order to develop an understanding of steam foam physics in differing rock morphology environments. An additional objective of this study was to develop techniques to analyze the pore network through CT imaging, MICP, and NMR in order to develop an understanding on the relationship between pore-scale environments and steam foam rheological behavior. This work has added knowledge to the behavior of steam foam in varying pore network systems. Through a better understanding of the physics of steam foam, as well as recent advancements in high-temperature surfactant formulation, steam foam as a thermal EOR process can be better designed, optimized, and utilized in oil recovery operations. The key results and conclusions are summarized.

From the sand pack experiments, a number of important conclusions are made that have added knowledge to the behavior of steam foam in complex systems.

1. The purpose of steam foam to lower the mobility of steam significantly in high permeability zones, while allowing steam flow in low permeability zones, was confirmed.
2. It was determined that steam foam has the greatest apparent viscosity at lower rates. High rates by the injection well would increase foam mobility and thus improve foam injectivity. With lower rates far into the formation, foam can stabilize and generate, reducing mobility.
3. The optimum foam quality is offset between low and high permeability sands. The optimum quality is greater in high permeability sands due to the shear rate of the flowing foam. Lower shear rates at higher permeability lead to strong, stable foam formation at higher qualities and dryer conditions. The foam quality can be optimized in field application with regards to this relationship.
4. The microheterogeneity of a rock affects the generation of steam foam. In low permeability rocks, a heterogeneous rock leads to higher apparent viscosities that remain relatively constant even at high injection rates in low permeability rocks. In high permeability rocks, this relationship is only seen at low foam qualities. At higher foam qualities, where the foam is dryer, the poorly-sorted environment of heterogeneous systems inhibits the formation of foam.
5. At sufficiently high rates, the apparent viscosity of steam foam remains constant or increases. Due to the range of pore throat sizes in a poorly-sorted environment, there is a range of minimum pressure gradients within the rock. Local fluctuations of pressure gradients and capillary pressures result in further generation of foam at higher flow rates, offsetting the shear thinning effect.
6. While the microheterogeneity affects the generation of foam, steam foam rheological behavior is more sensitive to the permeability of the rock and quality of the injected steam. Differences in permeability result in changes in the optimum foam quality and greatly impact the magnitude of the apparent viscosity. Furthermore, the growth and decay of foam viscosity are largely governed by quality, rather than rate.

Despite the discontinuation of the initial core flood experiment with low permeability Berea, a number of important conclusions can be made about the limitations encountered.

1. Steam foam generated in low permeability rocks is much weaker than in high permeability sands. This is expected, as the sand pack experiments revealed that lower permeabilities lead to weaker foams. However, the steam foam viscosity observed in low permeability rocks revealed limited mobility control. However, this may be due to mineral dissolution adversely affecting the surfactant solution, causing precipitation.
2. Core flood experiments are more complex than those involving sand packs. Rock cores introduce a number of different factors that may affect foam generation and destruction. Geochemical reactions at high temperature cause mineral dissolution.
3. Due to the tight nature of the core and slower total interstitial velocities, experiments with low permeability rocks require long periods of time to reach a steady-state for steam foam. For this reason, assessing the strength of steam foam in low permeability systems is overly time-consuming if the purpose is to test the surfactant.

Through extensive work with the techniques of CT imaging, MICP, and NMR, a number of conclusions are made on their efficacy for quick and accurate pore network characterization.

1. Obtaining a grain size distribution curve for sand mixtures was successful with CT scanning and imaging methods. The method developed with Fiji ImageJ were able to clearly segment and analyze the grains and void space in the processed 2D slice images.
2. Despite the refinement of the procedure, there were limitations in obtaining a pore size distribution for consolidated rock systems. CT imaging was successful in obtaining clear rock images; however, the segmentation and analysis with Fiji

ImageJ fell short. Due to the consolidated nature of the rock, pores were difficult to define, and inaccurate distributions were acquired.

3. MICP measurement of pore throat sizes was successful. The data obtained were accurate and the results were as expected.
4. NMR measurement of pore body sizes was successful. The data obtained were accurate and the results were as expected.
5. Using MICP and NMR in combination showed good agreement. As expected, the NMR distributions of pore bodies were greater than the MICP distributions of pore throats. Data gained from both tests successfully allowed for the determination of pore aspect ratio.

6.2 Recommendations

Many successes were made and limitations identified during the course of this study. Upon reflection of the conclusions made and the success of the developed methodologies, a number of recommendations are made.

1. Steam foam core flood experiments in low permeability rock are very complex and time-consuming. These experiments should not be conducted if the purpose is to assess the efficacy of a surfactant. Sand packs have been the standard in the industry and are simpler to set up and conduct.
2. Extensive flushing of the core is necessary before steam foam floods are conducted. Due to issues with mineral dissolution and fines migrations adversely affecting the surfactant, it is important to clean the core thoroughly. Solution analysis at all stages of the core preparation and flood is recommended to study the effect of geochemical reactions between the rock, minerals, and surfactant solution. It is recommended that conductivity be measured to assess mineral concentration in the produced solution, and pH be measured to determine if any surfactant is decomposing into acid.
3. Porous media flood experiments require multiple pore volumes of surfactant solution to be injected to generate and propagate a steady-state steam foam. From

the data gathered, at least four pore volumes of surfactant solution should be injected into a core before a proper steady-state is reached and before changing either the foam quality or injection rates.

4. Based on its successes, CT scanning and imaging should continue to be used for pore-scale characterization of sand pack systems. Despite the limitations encountered in this study with CT scanning of rocks, the technology holds much potential for pore-scale rock characterization. As literature has shown, CT imaging has been widely and successfully utilized. For the purpose of this study, more advanced techniques and methodologies are required to refine the process to accurately obtain pore size distributions for consolidated rocks.
5. It is recommended to continue utilizing MICP and NMR methods for rock pore network characterization. These methods are relatively quick and simple and provide an accurate wealth of data on a rock's pore-scale properties.

Despite the knowledge gained and developed from the work undertaken during this study, much is left to be explored on the topic of the relationship between rock morphology and its effects on steam foam rheology. As discussed, complete studies with consolidated rock cores were not completed. It is necessary to extend the knowledge made through the steam foam floods in sand pack systems to more complex rock environments. With the success of pore network characterization through MICP and NMR, the potential for linking rock morphology and steam foam performance and physics should be investigated. A number of recommendations are made for future work.

1. To expand the study on rock morphology and steam foam rheology, high permeability rocks should be used. High permeability allows faster interstitial velocities and a shorter time required to reach a foam steady-state. From the data gained in the study, Bentheimer and Castlegate sandstones are an attractive candidate.
2. Mobility reduction factor should be determined from core flood data to be used alongside apparent viscosity calculations to assess the strength of steam foam. Hot water floods should be conducted with rock cores.

3. Studying the relationship between rock morphology and steam foam behavior in low permeability rocks should be returned to. Despite their long time requirement, important conclusions can be made from the data collected. If similar patterns are observed between low permeability rocks and sand packs, then sand packs are appropriate to test steam foam in for field injection purposes. If different relationships are observed and interpreted, then sand packs are not appropriate for assessing the behavior of steam foam for field application.
4. To complete the study on the relationship between rock morphology and steam foam behavior, oil should be introduced into the system. Oil has a destabilizing effect on foam, and may greatly change the patterns observed from the sand pack floods. As steam foam is used as an EOR method, it is important to understand the physics of foam at high temperature when it encounters heavy oil. The conclusions and results made from the sand pack and rock studies will be tested for their validity when the system is up-scaled to an environment more closely resembling an unconventional reservoir.

References

Abell, A. B., Willis, K. L., & Lange, D. A. (1999, January 1). *Mercury Intrusion Porosimetry and Image Analysis of Cement-Based Materials*. Journal of Colloid and Interface Science, 211, pp. 39-44

Alvarado, D. A., & Marsden, S. S. (1979, December 1). *Flow of Oil-in-Water Emulsions Through Tubes and Porous Media*. Society of Petroleum Engineers. doi:10.2118/5859-PA

Alvarez, J. M., Rivas, H. J., & Rossen, W. R. (2001, September 1). *Unified Model for Steady-State Foam Behavior at High and Low Foam Qualities*. Society of Petroleum Engineers. doi:10.2118/74141-PA

Al Ayesh, A. H., Salazar, R., Farajzadeh, R., Vincent-Bonnieu, S., & Rossen, W. R. (2017, October 1). *Foam Diversion in Heterogeneous Reservoirs: Effect of Permeability and Injection Method*. Society of Petroleum Engineers. doi:10.2118/179650-PA

Al-Yaseri, A. Z., Lebedev, M., Vogt, S. J., Johns, M. L., Barifcani, A., & Iglauer, A. (2015, January 1). *Pore-scale analysis of formation damage in Bentheimer sandstone with in-situ NMR and micro-computed tomography experiments*. Journal of Petroleum Science and Engineering, 129, 48-57, ISSN 0920-4105. https://doi.org/10.1016/j.petrol.2015.01.018.

Amaefule, J. O., & Handy, L. L. (1982, June 1). *The Effect of Interfacial Tensions on Relative Oil/Water Permeabilities of Consolidated Porous Media*. Society of Petroleum Engineers. doi:10.2118/9783-PA

Bagheri, S. R., & Clark, H. P. (2015, October 11). *Steam-Foam Technology as an Option to Improve Steam Drive Efficiency.* Society of Petroleum Engineers. doi:10.2118/175278-MS

Beard, D. C., & Weyl, P K. (1973, February 1). *Influence of Texture on Porosity and Permeability of Unconsolidated Sand*. AAPG Bulletin, 57. 349-369.

Boeije, C. S., & Rossen, W. (2015, May 1). *Fitting Foam-Simulation-Model Parameters to Data: I. Coinjection of Gas and Liquid*. Society of Petroleum Engineers. doi:10.2118/174544-PA

Bond, D. C., & Holbrook, O. C. (1958, December 30). *Gas drive oil recovery process.* U.S. Patent No. 2,866,507. Washington, DC: U.S. Patent and Trademark Office.

Chen, Q., Gerritsen, M. G., & Kovscek, A. R. (2010, January 1). *Improving Steam-Assisted Gravity Drainage Using Mobility Control Foams: Foam Assisted-SAGD (FA-SAGD)*. Society of Petroleum Engineers. doi:10.2118/129847-MS

Churcher, P. L., French, P. R., Shaw, J. C., & Schramm, L. L. (1991, January 1). *Rock Properties of Berea Sandstone, Baker Dolomite, and Indiana Limestone*. Society of Petroleum Engineers. doi:10.2118/21044-MS

Cooke, R. W., & Eson, R. L. (1991, January 1). *Field Results of Optimizing the Steam Foam Diversion Process in Cyclic Steam Applications*. Society of Petroleum Engineers. doi:10.2118/21531-MS

Cuenca, A., Lacombe, E., Chabert, M., Morvan, M., & Delamaide, E. (2016, March 21). *Impact of Oil on Steam Foam Formulations at 250°C. Society of Petroleum Engineers.* doi:10.2118/179806-MS

Cuenca, A., Lacombe, E., Chabert, M., Morvan, M., & Delamaide, E. (2015, June 9). *Enhanced Viscosity Formulations For Steam Foam Applications: Impact On Performances In Bulk And Porous Media*. Society of Petroleum Engineers. doi:10.2118/174469-MS

Delamaide, E., Cuenca, A., & Chabert, M. (2016, October 19). *State of the Art Review of the Steam Foam Process*. Society of Petroleum Engineers. doi:10.2118/181160-MS

Dusseault, M. B. (2001, January 1). *Comparing Venezuelan and Canadian Heavy Oil and Tar Sands*. Petroleum Society of Canada. doi:10.2118/2001-061

Etminan, S. R., Goldman, J., & Wassmuth, F. (2016, March 21). *Determination of Optimal Conditions for Addition of Foam to Steam for Conformance Control*. Society of Petroleum Engineers. doi:10.2118/179841-MS

Falls, A. H., Lawson, J. B., & Hirasaki, G. J. (1988, January 1). *The Role of Noncondensable Gas in Steam Foams*. Society of Petroleum Engineers. doi:10.2118/15053-PA

Gauglitz, P. A., Friedmann, F., Kam, S. I., & Rossen, W. R. (2002, January 1). *Foam Generation in Porous Media*. Society of Petroleum Engineers. doi:10.2118/75177-MS

Gul, S., Kuru, E., & Parlaktuna, M. (2017, November 13). Experimental Investigation of Cuttings Transport in Horizontal Wells Using Aerated Drilling Fluids. Society of Petroleum Engineers. doi:10.2118/188901-MS

Hematpur, H., Mahmood, S. M., Nasr, N. H., & Elraies, K. A. (2018, May 1). *Foam flow in porous media: Concepts, models and challenges*. Journal of Natural Gas Science and Engineering, 53, 163-180. doi:10.1016/j.jngse.2018.02.017

Hirasaki, G. J. (1989, January 1). *Supplement to SPE 19505, The Steam-Foam Process--Review of Steam-Foam Process Mechanisms*. Society of Petroleum Engineers.

Hirasaki, G. J. (1989, May 1). *The Steam-Foam Process*. Society of Petroleum Engineers. doi:10.2118/19505-PA

Hirasaki, G. J., & Lawson, J. B. (1985, April 1). *Mechanisms of Foam Flow in Porous Media: Apparent Viscosity in Smooth Capillaries*. Society of Petroleum Engineers. doi:10.2118/12129-PA

Hirasaki, G. J., & Pope, G. A. (1974, August 1). *Analysis of Factors Influencing Mobility and Adsorption in the Flow of Polymer Solution Through Porous Media*. Society of Petroleum Engineers. doi:10.2118/4026-PA

Hutchinson, D. A., Demiral, B. D., & Castanier, L. (1992, January 1). *Steam Foam Studies In The Presence Of Residual Oil. Society of Petroleum Engineers*. doi:10.2118/23709-MS

Jackson, J. A. (1984, September 1). *Nuclear Magnetic Resonance Well Logging*. Society of Petrophysicists and Well-Log Analysts

Jerosch-Herold, M., Thomann, H., & Thompson, A. H. (1991, January 1). *Nuclear Magnetic Resonance Relaxation in Porous Media*. Society of Petroleum Engineers. doi:10.2118/22861-MS

Kang, P. S., Lim, J. S., & Huh, C. (2016, January 1*). Screening Criteria and Considerations of Offshore Enhanced Oil Recovery*. Energies, *9*(1), 44. doi:10.3390/en9010044

Kharabaf, H., & Yortsos, Y. C. (1998, March 1). *A Pore-Network Model For Foam Formation And Propagation in Porous Media*. Society of Petroleum Engineers. doi:10.2118/36663-PA

Khatib, Z. I., Hirasaki, G. J., & Falls, A. H. (1988, August 1). *Effects of Capillary Pressure on Coalescence and Phase Mobilities in Foams Flowing Through Porous Media*. Society of Petroleum Engineers. doi:10.2118/15442-PA

Kleinberg, R. L., Horsfield, M. A. (1990, June 1). *Transverse relaxation processes in porous sedimentary rock*. Journal of Magnetic Resonance, Volume 88, 1, 9-19, ISSN 0022-2364, https://doi.org/10.1016/0022-2364(90)90104-H

Kleinberg, R. L., & Vinegar, H. J. (1996, November 1). *NMR Properties of Reservoir Fluids*. Society of Petrophysicists and Well-Log Analysts.

Knight, R. (2011, January 1). *Nuclear Magnetic Resonance: From Pore-Scale Physics to Field-Scale Hydrogeophysics*. Society of Exploration Geophysicists

Krumbein, W. C., & Monk, G. D. (1942, October 1). *Permeability as a Function of the Size Parameters of Unconsolidated Sand*. Society of Petroleum Engineers. doi:10.2118/943153-G

Lashgari, H., Lotfollahi, M., Delshad, M., Sepehrnoori, K., & De Rouffignac, E. P. (2014, June 10). *Steam-Surfactant-Foam Modeling in Heavy Oil Reservoirs*. Society of Petroleum Engineers. doi:10.2118/170178-MS

Lau, H. C. (2012, August 1). *Alkaline Steam Foam: Concepts and Experimental Results*. Society of Petroleum Engineers. doi:10.2118/144968-PA

Lau, H. C., & Borchardt, J. K. (1989, January 1). *Improved Steam Foam Formulations: Concepts and Laboratory ResuIts. Society of Petroleum Engineers*. doi:10.2118/18783-MS

Li, Q., & Rossen, W. R. (2005, January 1). *Injection Strategies for Foam Generation in Homogeneous and Layered Porous Media*. Society of Petroleum Engineers. doi:10.2118/96116-MS

Li, Y., & Wardlaw, N. C. (1986, February 1). *The influence of wettability and critical pore-throat size ratio on snap-off*. Journal of Colloid and Interface Science, 109, 2, 461-472, ISSN 0021-9797. https://doi.org/10.1016/0021-9797(86)90324-3

Maini, B. B., & Ma, V. (1986, November 1). *Laboratory Evaluation Of Foaming Agents For High-Temperature Applications - I. Measurements Of Foam Stability At Elevated Temperatures And Pressures*. Petroleum Society of Canada. doi:10.2118/86-06-05

Marschall, D., Gardner, J. S., Mardon, D., & Coates, G. R. (1995, January 1). *Method for correlating NMR relaxometry and mercury injection data*. Presented at the Society of Core Analysts International Symposium, San Francisco, California, USA, 12–14 September. SCA-9511

Masch, F. D., & Denny, K. J. (1966, December 1). *Grain Size Distribution and Its Effect on the Permeability of Unconsolidated Sands*. Water Resour. Res., 2(4), 665–677. doi: 10.1029/WR002i004p00665

Moradi-Araghi, A., Johnston, E. L., Zornes, D. R., & Harpole, K. J. (1997, January 1). *Laboratory Evaluation of Surfactants for CO2-Foam Applications at the South Cowden Unit*. Society of Petroleum Engineers. doi:10.2118/37218-MS

Mukherjee, B., Patil, P. D., Gao, M., Miao, W., Potisek, S., & Rozowski, P. (2018, April 14). *Laboratory Evaluation of Novel Surfactant for Foam Assisted Steam EOR Method to Improve Conformance Control for Field Applications*. Society of Petroleum Engineers. doi:10.2118/190263-MS

Needham, R. B. (1968, November 1). *Plugging of High Permeability Earth Strata*. U.S. Patent No. 3,412,793. Washington, DC: U.S. Patent and Trademark Office.

Nguyen, Q. P. (2004). *Dynamics of foam in porous media*. PhD dissertation, Delft University of Technology, Delft, The Netherlands.

Nguyen, T., Rommerskirchen, R., Fernandez, J., & Nguyen, Q. P. (2018, March 26). *Surfactants As Steam Foam Additives for Thermal EOR Processes*. Society of Petroleum Engineers. doi:10.2118/190473-MS

Osterloh, W. T., & Jante, M. J. (1992, January 1). *Effects of Gas and Liquid Velocity on Steady-State Foam Flow at High Temperature*. Society of Petroleum Engineers. doi:10.2118/24179-MS

Overbeek, J. T. G. (1960, January 1). *Black Soap Films*. The Journal of Physical Chemistry, 64. doi:10.1021/j100838a017

Peksa, A. E., Wolf, K. A., & Zitha, P. L. (2015). *Bentheimer sandstone revisited for experimental purposes*. Marine and Petroleum Geology, 67, 701-719. doi:10.1016/j.marpetgeo.2015.06.001

Rossen, W. R. (1988, January 1). *Theories of Foam Mobilization Pressure Gradient*. Society of Petroleum Engineers. doi:10.2118/17358-MS

Rossen, W. R., & Gauglitz, P. A. (1990, August 1). *Percolation Theory of Creation and Mobilization of Foam in Porous Media*. AiChe J.

Rossen, W. R. (1999, December 1). *Foam Generation at Layer Boundaries in Porous Media*. Society of Petroleum Engineers. doi:10.2118/59395-PA

Rossen, W. R. (2013, September 30). *Numerical Challenges in Foam Simulation: A Review*. Society of Petroleum Engineers. doi:10.2118/166232-MS

Sanders, A., Nguyen, M. N., Ren, G., Westemoreland, D., Nguyen, Q., Dong, S., & Rojas, C. (2017, November 13). *Development of Novel Foaming Agents for High Temperature Steam Applications*. Society of Petroleum Engineers. doi:10.2118/188682-MS

Schallcross, D. C., Castanier, L. M., & Brigham, W. E. (1990). *Characterization of steam foam surfactants through one-dimensional sandpack experiments*. Stanford University, CA (USA). Petroleum Research Institute.

Schlumberger. (2016). *Heavy Oil. Defining Series*. Retrieved from https://www.slb.com/resources/oilfield_review/~/media/Files/resources/oilfield_review/defining_series/Defining-Heavy-Oil.ashx.

Schramm, L. L. (1994). *Foams: Fundamentals and Applications in the Petroleum Industry* (Vol. 242). American Chemical Society. doi:10.1021/ba-1994-0242

Shikhov, I., d'Eurydice, M. N., Arns, J., & Arns, C. H. (2017, April 4). *An Experimental and Numerical Study of Relative Permeability Estimates Using Spatially Resolved T1-z NMR*. Transport in Porous Media. doi:10.1007/s11242-017-0855-7.

Sun, G., & Grace, J. R. (1992, May 1). *Effect of Particle Size Distribution in Different Fluidization Regimes*. AIChE J., 38: 716-722. doi:10.1002/aic.690380508

Tandon, S., & Heidari, Z. (2016, September 26). *Impact of Internal Magnetic Gradients on Nuclear Magnetic Resonance Measurements and NMR-Based Pore Network Characterization*. Society of Petroleum Engineers. doi:10.2118/181532-MS

Tanzil, D., Hirasaki, G. J., & Miller, C. A. (2000, January 1). Mobility of Foam in Heterogeneous Media: Flow Parallel and Perpendicular to Stratification. Society of Petroleum Engineers. doi:10.2118/63228-MS

Tanzil, D. (2001, March 1). Foam generation and propagation in heterogeneous porous media. Diss., Rice University. http://hdl.handle.net/1911/18034

U.S. Energy Information Administration. (2019, January 1). U.S. Imports by Country of Origin. (n.d). Retrieved from http://www.eia.gov/dnav/pet/pet_move_impcus_a2_nus_epc0_im0_mbblpd_a.htm

Washburn E. W. (1921). Note on a Method of Determining the Distribution of Pore Sizes in a Porous Material. Proceedings of the National Academy of Sciences of the United States of America, 7(4), 115–116.

Zeng, Y., Bahrim, R. Z. K., Bonnieu, S. V., Groenenboom, J., Shafian, S. R. M., Manap, A. A. A., Tewari, R. D., Biswal, S. L. (2018, March 20). The Dependence of Methane Foam Transport on Rock Permeabilities and Foam Simulation on Fluid Diversion in Heterogeneous Model Reservoir. Offshore Technology Conference. doi:10.4043/28229-MS